DOE/ER-0046/8
Vol. 2

Damage Analysis and Fundamental Studies

Proceedings of a Workshop on Advanced Techniques for Radiation Damage Analysis

February 1982

U.S. Department of Energy
Assistant Secretary for Energy Technology
Office of Fusion Energy
Washington, DC 20545

NOTICE

This report was prepared as an account of work sponsored by the United States Government. Neither the United States nor the U.S. Department of Energy (DOE), nor any of its employes, nor any of its contractors, subcontractors or their employes, makes any warranty, expressed or implied, or assumes any legal liability or responsibility for any third party's use or the results of such use of any information, apparatus, product or process disclosed in this report, or represents that its use by such third party would not infringe privately owned rights.

Printed in the United States of America
Available from
National Technical Information Service
U.S. Department of Commerce
5285 Port Royal Road
Springfield, VA 22161

NTIS price codes
Printed copy: A09
Microfiche copy: A01

DOE/ER-0046/8
UC-20,20c
Vol. 2

Damage Analysis and Fundamental Studies

Proceedings of a Workshop on
Advanced Techniques for Radiation Damage Analysis

February 1982

U.S. Department of Energy
Assistant Secretary for Energy Technology
Office of **Fusion** Energy
Washington, DC 20545

PREFACE

This two-volume report contains two special contributions. Appended to Volume 1 is a critical assessment of the role of charged particle research in the Damage Analysis and Fundamental Studies (OAFS) program, prepared by several OAFS program participants under the leadership of G. R. Odette. Volume 2 contains the proceedings of a workshop on advanced experimental techniques for radiation damage analysis arranged under the OAFS program by P. Wilkes, F. V. Nolfi and J. A. Spitznagel. The participation of the various contributors, most of whom were not working on Office of Fusion Energy programs, is gratefully acknowledged.

PROCEEDINGS OF THE
WORKSHOP ON AOVANCED TECHNIQUES
FOR RADIATION DAMAGE ANALYSIS

Oak Brook, Illinois

March 8 and 9, 1979

Sponsored by the Damage Analysis and Fundamental Studies Task Group,
Fusion Reactor Materials Program, Office of Fusion Energy,
Department of Energy

Foreword

The workshop was intended to assist the fusion materials comnunity in assessing the usefulness of a variety of sophisticated techniques currently available in analysis of radiation damage microstructures. The fusion materials program will require careful analysis of large numbers of irradiated samples by a relatively small group of qualified scientists and engineers. The problem is exacerbated by the absence of any high dose rate, 14-MeV neutron facility. This places great demands on predictions from other neutron sources and, in turn, requires a very complete understanding of the fundamental processes occurring in void swelling, radiation phase instability, radiation creep, fatigue, and fracture. Therefore, it is necessary to make appropriate use of every technique that can provide useful information on relevant microstructural features and, in addition, to explore the possibilities of using technically trained people to maximum efficiency by means of innovative data collection systems.

The primary purpose of the workshop was, therefore, to acquaint the community with current developments in the techniques of radiation damage microstructure. A secondary purpose was to begin detailed examination of the usefulness of these techniques in discussion sessions. The test for the success of the workshop is whether future work by the fusion materials community will be able to use the techniques described.

The workshop was made possible through technical contributions by leading investigators, most of whom are not working directly on Office of Fusion Energy programs. This participation is gratefully acknowledged.

Peter Wilkes
Frank Nolfi
John Spitznagel

CONTENTS

		Page
	Foreword	vi
	Figures	vii
	Tables	xii
I.	SUMMARY	1
II.	PROGRAM AGENDA	3
III.	WORKSHOP PARTICIPANTS	5
IV.	CONTRIBUTIONS	9
	A SUMMARY OF PROBLEMS ASSOCIATED WITH PRIMARY DAMAGE AND SECONDARY DEFECT AGGREGATION UNDER CTR IRRADIATION CONDITIONS M. R. Hayns, United Kingdom Atomic Energy Authority-Harwell	11
	A SUMMARY OF THE CURRENT UNDERSTANDING OF THE SECONDARY DAMAGE MICROSTRUCTURE H. Wiedersich, Argonne National Laboratory	33
	RADIATION DAMAGE ANALYSIS BY POSITRON ANNIHILATION SPECTROSCOPY R. W. Siegel, Argonne National Laboratory	57
	HIGH SPATIAL RESOLUTION CHEMICAL MICROANALYSIS IN DAMAGE STUDIES D. C. Joy, Bell Laboratories	81
	HIGH RESOLUTION TRANSMISSION ELECTRON MICROSCOPY AND MICRODIFFRACTION FOR RADIATION DAMAGE ANALYSIS R. Sinclair, Stanford University	93
	APPLICATIONS OF ION CHANNELING TO RADIATION DAMAGE STUDIES S. T. Picraux, Sandia Laboratories	99
	SMALL ANGLE AND DIFFUSE SCATTERING OF X-RAYS AND NEUTRONS R. W. Hendricks, Oak Ridge National Laboratory	105
	THE STUDY OF DEFECTS AND RADIATION DAMAGE IN SOLIDS BY FIELD-ION AND ATOM-PROBE MICROSCOPY D. M. Seidman, Cornell University	107

CONTENTS (Cont'd)

		Page
	QUANTITATIVE DATA EXTRACTION FROM TRANSMISSION ELECTRON MICROGRAPHS J. A. Sprague, Naval Research Laboratory	131
	HYPERFINE TECHNIQUES AND EXAFS: PROBES OF SPECIFIC ATOMIC ENVIRONMENTS F. Y. Fradin, Argonne National Laboratory	137
	SURFACE ANALYSIS TECHNIQUES M. G. Lagally, University of Wisconsin	151
V.	EDITED SUMMARY OF WORKSHOP DISCUSSION P. Wilkes, University of Wisconsin F. V. Nolfi, Argonne National Laboratory J. A. Spitznagel, Westinghouse Research & Development Center	165
VI.	COMMENTS	173

FIGURES

Page

A Summary of Problems Associated with Primary Damage and Secondary Defect Aggregation Under CTR Irradiation Conditions (UKAEA) 11

FIGURE 1. The Production of Subcascades in a 14 MeV Displacement Cascade in Gold. 13

FIGURE 2. Local Vacancy Concentrations Due to Pulsed Irradiations. 15

FIGURE 3. Local Interstitial Concentrations Due to Pulsed Irradiations. 15

FIGURE 4. Difference in Void Radius Computed With and Without Spacially Inhomogeneous Defect Flux. 16

FIGURE 5. Interstitial Loop Density in e^- Irradiated Silver and Gold. 18

FIGURE 6. Calculated Interstitial Loop Density as a Function of Temperature. 19

FIGURE 7. Critical Cavity Size as a Function of Temperature and Dose Rate. 22

FIGURE 8. Calculated Bubble Density in 316 Stainless Steel as a Function of Temperature for Various Gas Atom Trap-Binding Energies. 24

FIGURE 9. Electron Micrograph of Bimodel Void Populations in 'Pure' 316 Stainless Steel at 70 dpa. 26

FIGURE 10. Histograms of the Void Size Distributions Obtained From the Micrographs Shown in Figure 9. 27

FIGURE 11. The Calculated Evolution of the Void Size Distribution in CW 316 Steel Under Neutron Irradiation Conditions at 550°C. 28

FIGURE 12. Calculated Observable Void Concentrations for VEC Conditions Shown With the Observed Void Densities. 23

A Summary of the Current Understanding of the Secondary Damage Microstructure (ANL) 33

FIGURE 1. Dislocation Structure Development in a Ni-12.8 at. % Al Alloy During Ni-ion Bombardment at 550°C. 36

FIGURE 2. Void and Interstitial Loop Number Densities, Swelling $\Delta V/V$ and Network Dislocation Density as Function of Dose for Solution Annealed Type 316 Stainless Steel, Irradiated With 1.0 MeV Electrons at 500°C. 37

FIGURES (Cont'd)

		Page
FIGURE 3.	Micrographs of a Ti-14.4 at. % Al Alloy Nickel-Ion Bombarded to Approximately 15 dpa at the Temperatures Indicated.	38
FIGURE 4.	Ordered Voids in Nb-O Alloys After Ni-Ion Bombardment at 780°C and at 828°C to 50 dpa.	40
FIGURE 5.	Diffusion Coefficient as Function of Inverse Temperature Calculated from Rate Theory for a Nickel Based Substitutional Alloys.	41
FIGURE 6.	Average Diameter of γ' Precipitates Raised to the Third Power in Ni-12.8 at. % Al as Function of Dose During Ni-Ion Irradiation at the Temperatures Indicated.	43
FIGURE 7.	Coarsening Rate Constant K as Function of Inverse Temperature for a Ni-12.7 at % Si Alloy During Ni-Ion Bombardment of a Displacement of $\sim 2.7\ 10^{-3}$ dpa/s (+).	44
FIGURE 8.	Apparent Temperature of Ni_3Si Measured With an Infrared Pyrometer as Function of Bombardment Time With Ni-Ions.	46
FIGURE 9	Precipitation of Ni_3Si on Defect Sinks in Solid Solution Ni-Si Alloys During Irradiation.	48
FIGURE 10.	Formation of b.c.c. precipitates in a h.c.p. Commercial Purity Ti-6 wt.% A1-4 wt.% V Solution-Annealed Alloy During V-Ion Bomhardment.	49
FIGURE 11.	Development of the Precipitate Microstructure During Irradiation of a Ni-12.8 at. % Al Two-Phase Alloy.	50
FIGURE 12.	Dislocation-Precipitate Interaction as Illustrated by Dissolution of Particles Present Prior to Irradiation.	51
FIGURE 13.	Precipitate Diameter and Number Density as Function of Dose in a Ni-12.8 at. Al Alloy Irradiated at the Temperatures Indicated.	53
Radiation Damage Analysis by Positron Annihilation Spectroscopy (ANL)		57
FIGURE 1.	Positron Annihilation Spectroscopy.	58
FIGURE 2.	Positron Density x Ω_0 in W in the Bloch State of the Positron.	59
FIGURE 3.	Positron Density x Ω in W in the Vacancy-Trapped State of the Positron.	59

FIGURES (Cont'd) Page

FIGURE 4. Positron-Lifetime Spectra After Source-Background Subtractions in Electron-Irradiated High-Purity a-Fe at Various Stages of Isochronal Annealing. 61

FIGURE 5. Angular-Correlation Curves From Al at 100K, 600°C, and Containing Voids. 61

FIGURE 6. Doppler-Broadening Lineshape-Parameter F(T) for Cu Versus Temperature, T, and the Two-Stage Trapping Model Fit to the Data. 68

FIGURE 7. Arrhenius Plot of the Data and Fit for Cu Shown in Figure 6. 68

FIGURE 8A. Doppler-Broadening Study of Electron-Irradiation Cu. 71

FIGURE 8B. The Ratio of Lineshape-Parameter Differences for Electron-Irradiated Cu Versus Annealing Temperature is Compared With That for Quenched Au and Calibrated Values for Cu for Vacancies, Dislocation Loops, and the Liquid. 72

FIGURE 8C. The Lineshape-Parameters I_V and I_C are Indicated on Doppler-Braodened Annihilation Lines. 72

FIGURE 9. The Lifetime τ_2 and Intensity I_2 of Trapped Positrons in Electron-Irradiated High Purity a-Fe Versus Isochronal-Annealing Temperature. 74

FIGURE 10, Isochronal-Annealing Behavior of the Defect-Trapped Positron-Lifetime τ_2 in Neutron-Irradiated and Electron-Irradiated Mo. 75

FIGURE 11A. Calculated Positron Lifetimes in Microvoids in Al and Mo as a Function of Void-Radius R. 77

FIGURE IIB. A Combination of Calculation Results From Reference 29 for Mo Shown in Figure 11A and the Experimental Positron Lifetimes From Reference 28 Shown in Figure 10 Indicating the Estimated Number of Vacancies per Average-Size Microvoid as a Function of Annealing Temperature. 77

High Spatial Resolution Chemical Microanalysis in Damage Studies (Bell Labs) 81

FIGURE 1. The Schematic Arrangement of the Electron Beam, the Specimen, and the Spectrometers in an Analysis Electron Microscope. 82

FIGURE 2. (a) The Factors Affecting the Sensitivity of X-ray Analysis, and (b) The Factors Affecting Electron Energy Loss Analysis. 84

FIGURES (Cont'd)

Page

FIGURE 3. The Variation in Minimum Detectable Mass (MDM) as a Function of Atomic Number in EDXS. 86

FIGURE 4. Electron Energy Loss Spectrum Recorded at 100 kV From a Thin Carbon Film. 89

FIGURE 5. A Comparison of the Minimum Detectable Mass Sensitivities, as a Function of Z, for EELS and EDXS at 100 kV. 91

FIGURE 6. A Comparison of Nitrogen K-Edges From Silicon Foils 100 and 500 Å Thick Showing the Effects of Multiple Scattering on the Visibility of the Edge. 91

Application of Ion Channeling to Radiation Damage Studies (Sandia) 99

FIGURE 1. The 2 MeV He Ion Backscattering Spectra for <110> axial and {111} Planar Channeling in Aℓ Before and After 7 x 10^{15} Ni/cm^2 Implantation. 102

FIGURE 2. Disorder and Ni Depth Profiles Obtained From the Spectra of Figure 1. 102

The Study of Defects and Radiation Damage in Solids by Field-Ion and Atom-Probe Microscopy (Cornel1 U) 107

FIGURE 1. The In-Situ Irradiation of a W FIM Specimen With 300 eV $^4He^+$ Ions at a T_i Where the Implanted ^4He Atoms are Inmobile. 114

FIGURE 2. A Schematic Diagram Illustrating the Method Employed to Determine an Absolute Depth Scale. 116

FIGURE 3. The ^3He Integral Profiles for the Implantation Energies of 100, 500 and 1500 eV. 117

FIGURE 4. A Composite ^3He Range Profile for all 300 eV Implantations at 60K. 117

FIGURE 5. The ^4He Integral Profiles for the Implantation Energies of 150, 475, 500 and 1000 eV. 119

FIGURE 6. A Composite ^4He Range Profile for all the 1000 eV Implantations at 6DK. 119

FIGURE 7. Mean Range ($\bar{x}$) in Angstroms Versus Incident Helium Energy (ev) for all the ^4He Implantations in Tungsten at 60K. 121

FIGURES (Cont'd)

Page

FIGURE 8. Standard Diviation or Straggling in Angstroms (Ax) Versus Incident Helium Energy (eV) for all the ^3He and ^4He Implantations in Tungsten at 60K. 121

FIGURE 9. The Relative Variance $[(\Delta x)^2/(\bar{x})^2]$ Versus the Incident Helium Energy (eV) for all the ^3He and ^4He Implantations in Tungsten at 60K. 123

FIGURE 10. The Diffusion Coefficient of ^3He Versus (1/T) in the Temperature Range 90 to 110K. 125

Hyperfine Techniques and Exafs: Probes of Specific Atomic Environments (ANL) 137

FIGURE 1. Spin Lattice Relaxation Time T_1 for $^{27}A\ell$ in the Rotating Frame Vs. the Reciprocal Temperbture. 139

FIGURE 2. Results (Figure 1) for the Diffusion Coefficient of $A\ell$, Together With Other Determinations, Plotted Against Reciprocal Temperature. 139

FIGURE 3. Transverse Magnetization Decay for ^3He Contained in Three-Year-Old $Ti^3H_{1,8}$ After Weaver. 140

FIGURE 4. Longitudinal Magnetization Recovery for ^3He Contained in Three-Year-Old $Ti^3H_{1,8}$ After Weaver. 140

FIGURE 5. Free-Induction Decay for ^3He Implanted into Pd. 140

FIGURE 6. Experimental Fourier Transform of $^{27}A\ell$ PNMR Free Induction Decay of Annealed Pu $A\ell_2$ at 12 MHz and 77°K. 142

FIGURE 7. Experimental Fourier Transform of $^{27}A\ell$ PNMR Free Induction Decay of Damage $PuA\ell_2$. 143

FIGURE 8. Showing Two Decay Curves F(t) After the Spin Locking Sequence With Zero and Finite Plastic Deformation Rates. 143

FIGURE 9. Comparison Between Jeener (R_D) and Spin Locking ($R_D(\rho)$) Experiment. 143

FIGURE 10. Characteristic Mossbauer Spectra of $^{57}Co(^{57}Fe)$ in Aluminum Before and After Fast Neutron Irradiation at 4·6K and After Subsequent Isochronal Annealing. 144

FIGURES (Cont'd)

Page

FIGURE 11. Logarithm of Debye-Waller Factor of $^{57}Co(^{57}Fe)$ (<1 ppm) in Aluminum. 146

FIGURE 12. A. Absorption Edge of Ge.
B. EXAFS After Background Subtraction.
C. Atomic Absorption Background After Lytle et al. 146

FIGURE 13. Fe K-Edge EXAFS, Amplitude of Fourier Transform, for a Number of Doped Na-Silicate Glasses. 150

Surface Analysis Techniques (U. of Wisconsin) 151

FIGURE 1. Relation Between Surface Structure and Surface Composition. 152

FIGURE 2. Auger Spectrum of Stainless Steel. 157

FIGURE 3. ESCA Spectrum of 70-30 Brass, Also Showing Several Auger Peaks. 159

FIGURE 4. Positive and Negative SIMS Spectra of Stainless Steel. 160

FIGURE 5. ISS Spectrum of Ne and He Incident on Mo-Contaminated Au/Ni Alloy, Showing the Greater Mass Resolution Obtainable With More Massive Ions. 162

TABLES

Page

Radiation Damage Analysis by Positron Annihilation Spectroscopy (ANL)

TABLE 1. Some Recently Measured Values of the Vacancy Formation Enthalph, H_V^F, for Several Metals by PAS. 69

WORKSHOP ON ADVANCED TECHNIQUES FOR RADIATION DAMAGE ANALYSIS

I. SUMMARY

The aim of the workshop is to examine a wide range of state-of-the-art, solid-state techniques and determine their usefulness in high-temperature radiation damage studies. The first day of the program included invited lectures on a variety of physical techniques with overviews of the current understanding of damage microstructures. The second day included a detailed examination of the techniques by a selected panel (with some audience participation) to determine the particular usefulness of each technique in studying high-temperature damage microstructures.

11. PROGRAM AGENDA

Thursday, March 8			
8:00 to 8:30 am	REGISTRATION		
8:00 to 10:25 am	FIRST SESSION	TC Reuther, Chairman	DOE
	CHAIRMAN'S REMARKS		
	CURRENT UNDERSTANDING OF THE PRIMARY DAMAGE MICROSTRUCTURE	MR Hayns	UKAEA
	CURRENT UNDERSTANDING OF THE SECONDARY DAMAGE MICROSTRUCTURE	H. Weidersich	ANL
	POSITRON ANNIHILATION	RW Siegel	ANL
10:25 to 10:45 am	COFFEE BREAK		
10:45 to 12:30 pm	SECOND SESSION		
	ENERGY DISPERSIVE X-RAY ANALYSIS AND ENERGY LOSS SPECTROSCOPY	DC Joy	Bell Labs
	ULTRA-HIGH RESOLUTION TEM AND MICRODIFFRACTION	R. Sinclair	Stanford
	CHANNELLING TECHNIQUES	ST Picraux	Sandia
12:30 to 1:30 pm	LUNCH		
1:30 to 3:10 pm	THIRD SESSION		
	DIFFUSE SCATTERING OF NEUTRONS AND X-RAYS	RW Hendricks	ORNL
	FIELD ION MICROSCOPY	DN Seidman	Cornel1 U
	DATA HANDLING FOR TRANSMISSION ELECTRON MICROSCOPY	JA Sprague	ONR
3:10 to 3:30 pm	COFFEE BREAK		
3:30 to 4:45 pm	FOURTH SESSION		
	HYPERFINE INTERACTIONS	FY Fradin	ANL
	SURFACE ANALYSIS TECHNIQUES	MG Lagally	U of W
7:00 pm	WORKSHOP BANQUET		

Friday, March 9

9:00 to 10:30 am	PANEL DISCUSSION	P. Wilkes, Moderator	U of W

A panel examination of the techniques described on the first day and their applications to damage microstructure. A group of seven panel members (listed below) will question the speakers from the first day on the advantages, limitations, and practicality of each technique for observation of microstructural effects resulting from irradiation with particular reference to fusion reactor conditions. There will be limited time for audience questions and comments.

PANEL MEMBERS		Areas of Concentration
DG Doran	HEDL	Cascade Structure & Lonsequences Including Defect Survival
GR Odette	UCSB	Concentrations & Distributions of Point Defects
WJ Choyke	WR&D	Concentrations & Distributions of He & H
PR Okamoto	ANL	Solute Segregation
DI Potter	ANL	Precipitation
JO Stiegler	ORNL	Small Voids
K. Westmacott	U of C Berkeley	Concentrations & Distributions of Small Loops

10:30 to 10:45 am	COFFEE BREAK		
10:45 to 12:00 pm	PANEL DISCUSSION (Cont'd)	JA Spitznagel, Moderator	WR&D
12:30 to 1:00 pm	OFFICIAL END	TC Reuther	DOE
	CLOSING COMMENTS	TC Reuther	DOE

1:30 to 3:30 pm After the conference ends, the afternoon members of DOE/OFE Materials Branch, the DAFS Task Group, and the panel of questioners will meet for about 2 hours to summarize the information required for publication of the Workshop proceedings and for a report to the DAFS Task Group.

III. WORKSHOP PARTICIPANTS

James Bentley
Oak Ridge National Laboratory
P.O. Box X
Oak Ridge, TN 37830

Howard Brager
Hanford Engineering Development Laboratory
P.O. Box 1970, W/A-57
Richland, WA 99352

John L. Brimhall
Battelle Memorial Institute
Pacific Northwest Laboratory
P.O. Box 999
Richland, WA 99352

Albert L. Chang
Westinghouse-ARD
Madison, PA 15663

Wolfgang J. Choyke
Westinghouse R&D Center
1310 Beulah Road
Pittsburgh, PA 15235

Donald G. Doran
Hanford Engineering Development Laboratory
P.O. Box 1970, W/A-57
Richland, WA 99352

David Faulkner
Atomic Energy of Canada LTD
Whiteshell Nuclear Research Establishment
Pinawa, Manitoba Roe Ilo

Frank Y. Fradin
Argonne National Laboratory
Materials Science Division
9700 South Cass Avenue
Argonne, IL 60439

Lawrence R. Greenwood
Argonne National Laboratory
Chemical Engineering Division
9700 South Cass Avenue
Argonne, IL 60439

Michael W. Guinan
Lawrence Livermore Laboratory
P.O. Box 808, L-233
Livermore, CA 94550

Otto K. Harling
Massachusetts Institute of Technology
Nuclear Reactor Laboratory
138 Albany Street, Room 204
Cambridge, MA 02139

Michael R. Hayns
Oak Ridge National Laboratory
P.O. Box X
Oak Ridge, TN 37830

Robert W. Hendricks
Oak Ridge National Laboratory
P.O. Box X
Oak Ridge, TN 37830

David C. Joy
Bell Laboratories
Materials Research Division
600 Mountain Avenue
Murray Hill, NJ 07974

Max G. Lagally
University of Wisconsin
Dept of Metallurgical Engineering
1509 University Avenue
Madison, WI 53706

Kang-Yih Liou
Argonne National Laboratory
Materials Science Division
9700 South Cass Avenue
Argonne, IL 60439

Philip J. Maziasz
Oak Ridge National Laboratory
P.O. Box X
Building 5500, X-10
Oak Ridge, TN 37830

Karl L. Merkle
Argonne National Laboratory
Materials Science Division
9700 South Cass Avenue
Argonne, IL 60439

John Moteff
University of Cincinnati
Materials Science &
Met. Engineering Dept
Cincinnati, OH 45221

Frank V. Nolfi, Jr.
Argonne National Laboratory
Materials Science Division
9700 South Cass Avenue
Argonne, IL 60439

Richard E. Nygren
P.O. Box 1970, W/A-58
Richland, WA 99352

G. Robert Odette
University of California
Dept of Chemical & Nuclear Eng
Santa Barbara, CA 93106

Paul R. Okamoto
Argonne National Laboratory
Materials Science Division
9700 South Cass Avenue
Argonne, IL 60439

James E. O'Neal
McOonnell-Douglas Astronautics Co.
Dept 224, Bldg 33/45
P.O. Box 516
St. Louis, MO 63136

Nicolas H. Packan
Oak Ridge National Laboratory
P.O. Box X
Oak Ridge, TN 37830

Samual T. Picraux
Sandia Laboratories
P.O. Box 5800
Division 511
Albuquerque, NM 87185

Donald I. Potter
Argonne National Laboratory
Materials Science Division
9700 South Cass Avenue
Argonne, IL 60439

Roger W. Powell
Hanford Engineering Development
Laboratory
P.O. Box 1970, W/A-64
Richland, WA 99352

Lynn Rehn
Argonne National Laboratory
Materials Science Division
9700 South Cass Avenue
Argonne, IL 60439

Ted C. Reuther
DOE/Office of Fusion Energy
Materials & Radiation Effects Branch
ER-70
Washington, OC 20545

Margaret L. Sattler
University of Virginia
Dept of Materials Science
Thornton Hal1
Charlottesville, VA 22901

Richard W. Schmunk
EG&G Idaho, Inc.
P.O. Box 1625
Idaho Falls, ID 83415

David M. Seidman
Cornel1 University
Dept of Materials Science & Eng
Bard Hall
Ithaca, NY 14853

Richard W. Siegel
Argonne National Laboratory
Materials Science Division
9700 South Cass Avenue
Argonne, IL 60439

Robert Sinclair
Stanford University
Oept of Materials Science & Eng
Stanford, CA 94305

John A. Spitznagel
Westinghouse R&O Center
1310 Beulah Road
Pittsburgh, PA 15235

Stephen Spooner
Georgia Institute of Technology
School of Chemical Engineering
Atlanta, GA 30332

James A. Sprague
Office of Naval Research
Naval Research Laboratory
Code 6395
Washington, OC 20375

JO Stiegler
Oak Ridge National Laboratory
P.O. Box X
Oak Ridge, TN 37830

Eddy Tjhia
1013 Milton St, #301
Madison, WI 53715

Louise Weaver
University of California
School of Engineering & Applied Science
6532 Boelter Hall
Los Angeles, CA 90024

K. Westmacott
University of California
at Berkeley
Berkeley, CA 94720

Hartmut Wiedersich
Argonne National Laboratory
Materials Science Division
9700 South Cass Avenue
Argonne, IL 60439

F. W. Wiffen
Oak Ridge National Laboratory
P.O. Box X
Oak Ridge, TN 37830

Peter Wilkes
University of Wisconsin
Oept of Metallurgical Eng
1509 University Avenue
Madison, WI 53706

William O. Wilson
Sandia Laboratories
Theoretical Division 8341
Livermore, CA 94550

Susan Wood
Westinghouse R&D Center
1310 Beulah Road
Pittsburgh, PA 15235

IV. CONTRIBUTIONS

A SUMMARY OF PROBLEMS ASSOCIATED WITH PRIMARY DAMAGE AND SECONDARY DEFECT AGGREGATION UNDER CTR IRRADIATION CONDITIONS*

M. R. Hayns†

I. INTRODUCTION

The characterization of the irradiation damage in steels exposed to neutron irradiation in the first wall of CTRs is an immensely complex and daunting problem. In addition to the known, but not completely solved problems associated with lower energy neutron damage in FBRs, no major experimental facility exists, or will exist in the near term, for the investigation of the effects of the harder neutron spectrum and its associated helium generation. Consequently, an experimental program of irradiation in fission reactors and simulation environments (heavy ions or 7 MeV electrons) is the only means of obtaining pertinent data. Thus, if these data are to be at all useful, we must have a sufficiently detailed physical understanding of the processes to allow quantitative extrapolation to the CTR environment. It is therefore necessary to isolate those mechanisms which require a detailed knowledge of materials parameters and to establish procedures with the available equipment which can provide this information. The purpose of this workshop is to discuss the available experimental techniques and to establish their usefulness in this area. This brief review, and the one following it, attempt to outline some of the mechanisms which play an important role in the damage process and hence isolate these quantities which require detailed experimental investigations. Here we are concerned with the primary stages of the damage process and we cover two areas in particular. The first is the nature of the displacement damage under 14 MeV neutrons, compared with either fission reactor or simulation conditions. The second is the broad area of the nucleation and stability of secondary defects (aggregates of point defects).

II. PRIMARY DAMAGE AND THE IMPORTANCE OF DISPLACEMENT CASCADES

The problem of relating the lattice atom displacements due to impingeing energetic particles has plagued the study of irradiation damage. Here we

*Work performed at UKAEA Harwell, England
†Now on assignment at Oak Ridge National Laboratory, Oak Ridge, Tennessee 37030.

concentrate upon those aspects which specifically relate to CTR irradiation environments and the correlation with lower energy neutrons, heavy ions or electrons. Two questions are highlighted, the ramifications of the harder neutron spectrum and the pulsed nature of the irradiation.

In the fission reactor the principal damage component arises from neutrons with ~1 MeV energy. Collisions between these particles and lattice atoms dislodge the lattice atoms with sufficient energy to dislodge further lattice atoms. This process continues until the displaced atoms do not have sufficient energy to dislodge further atoms. The area of crystal undergoing such a process is termed a displacement cascade. In this region both interstitials and vacancies are produced and, whilst considerable numbers may be annihilated by recombination, a vacancy-rich core can remain as the interstitials rapidly diffuse away. The vacancy supersaturation in the core is such that vacancy loops can form. Thus, the number of 'free' point defects created by a single collision event depends upon the energetics of the displaced atoms, the diffusivity of the defects and the number *of* vacancies trapped temporarily in vacancy loops. For fussion realted conditions and for heavy ions (typically 4-40 MeV nickel ions) the production of vacancy loops is well established,"? and some idea of their size and shrinkage kinetics has been established.[3] For electron irradiation no displacements occur because the energy available is only sufficient for Frenkel pair production. In this case, the threshold energy for displacements and the effects of correlated recombination are the principle problems. Thus, in order to correlate the three types of irradiation, the displacement events must be understood in some detail. Under 14 MeV neutron irradiation the displacement events are expected to be significantly larger, with the possibility of subcascade formation. This would lead to more than one vacancy loop per collision event; such a situation is shown in Fig. 1, taken from Ref. (1). The principal quantities to be characterized are the number of defects surviving the cascades and the size, type, and concentration of the secondary defects. A range of measuring techniques could be used; up to now TEM and electrical resistivity have dominated but, as detailed in a recent review,[4] diffuse x-ray scattering, mechanical property changes, superconductivity, internal friction, and neutron sputtering have all been used to some extent. Computer simulation of displacement cascades also provides a

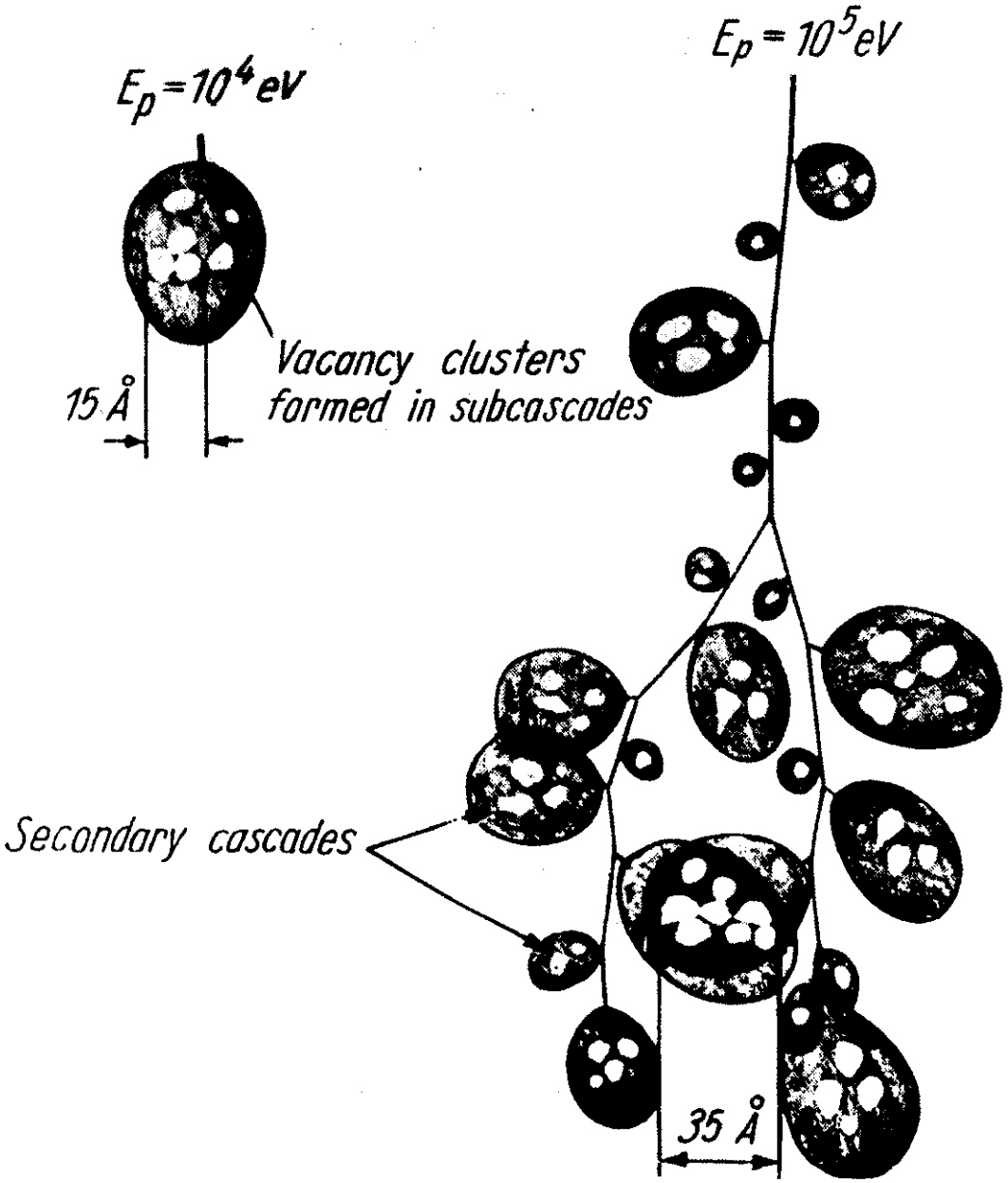

Figure 1. The production of subcascades in a 14 MeV displacement cascade in gold (from Ref. 1).

significant source of information.[5] Clearly such processes are most important for projected CTR materials applications and, without generally available sources of 14 MeV neutrons, their influence can only be understood by extrapolating physical models based upon information gleaned from lower energy neutron or heavy ion experiments. This places a great burden upon both the basic data and the theoretical models for some years to come.

Another possibly important distinction between CTR environments and those typically existing in FBRs and simulation experiments is that the latter produce a very uniform damage as a function of time (unless specifically altered) whilst all of the CTR designs, whether they are tokamaks or laser fusion devices, operate on pulsed basis. Plasma burns in experimental reactors are expected to occur with cycle times in the region of a few per second to a few seconds per pulse. As the damage will be imposed as large displacement cascades, as discussed above, it is important to understand how cycling such damage can influence the irradiation microstructure. We are not aware of any experimental data, but a theoretical study has recently been reported.[6] The significant new feature studied is the inhomogeneous nature of the damage structure both spatially and temporally. The argument can be sumnarized as follows. At a particular point in space cascades will occur at random distances and times around it. Large local fluctuations in point defect concentrations occur as the virtually instantaneous 'wind' of interstitials from new cascades cross the reference point. The local vacancy concentration varies much more slowly, reflecting the much lower mobility of these defects. Figures 2 and 3 are typical of the computed local point defect concentrations arising from random cascade production for vacancies and interstitials, respectively. Even though the local defect concentrations vary by almost an order of magnitude, comparisons with the spatially and temporally averaged rate theory continuum model traditionally used shows that for most instances of *continuous* irradiation the averaging processes lead to an adequate representation of void growth except at elevated temperature, and this is illustrated in Fig. 4 where the fractional changes in void radius with and without spatial averaging are shown. However, cyclic operation, with a cycle time $\lesssim$ the relaxation time implied by Fig. 2 could lead to an accute sensitivity to this effect and have a significant, though as yet undetermined, effect on secondary defect nucleation.

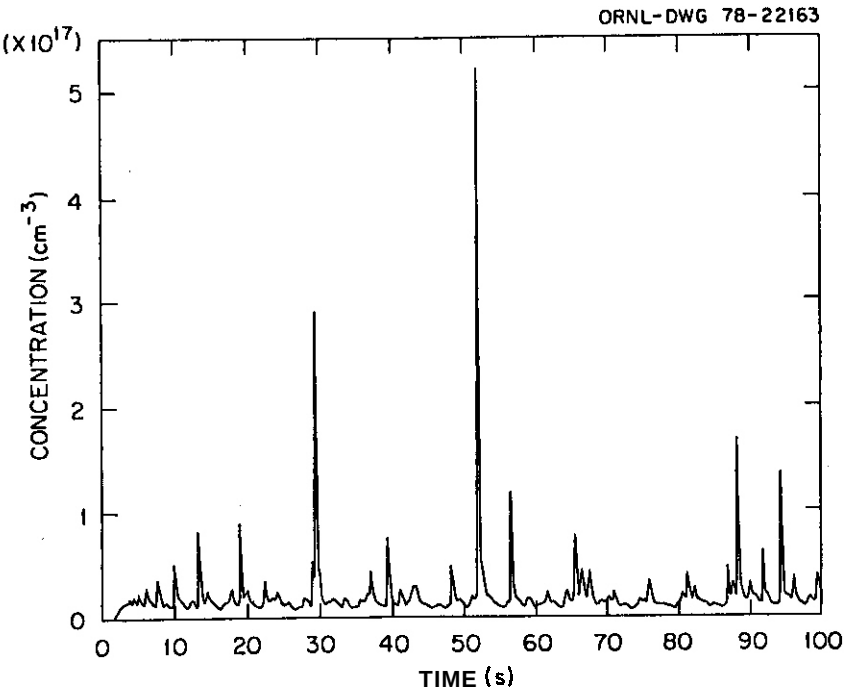

Figure 2. Local vacancy concentrations due to pulsed irradiations (Ref. 6).

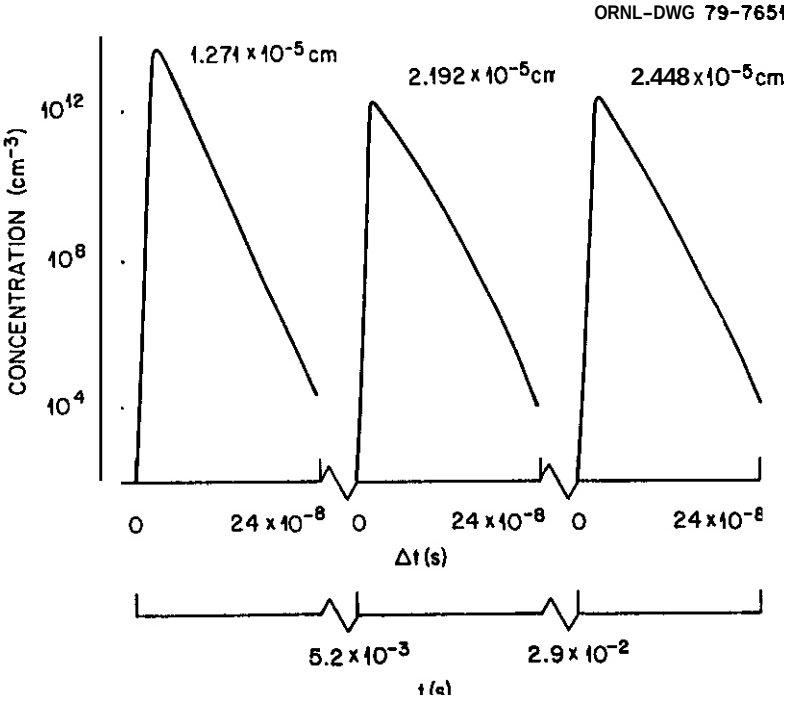

Figure 3. Local interstitial concentrations due to pulsed irradiations (Ref. 6)

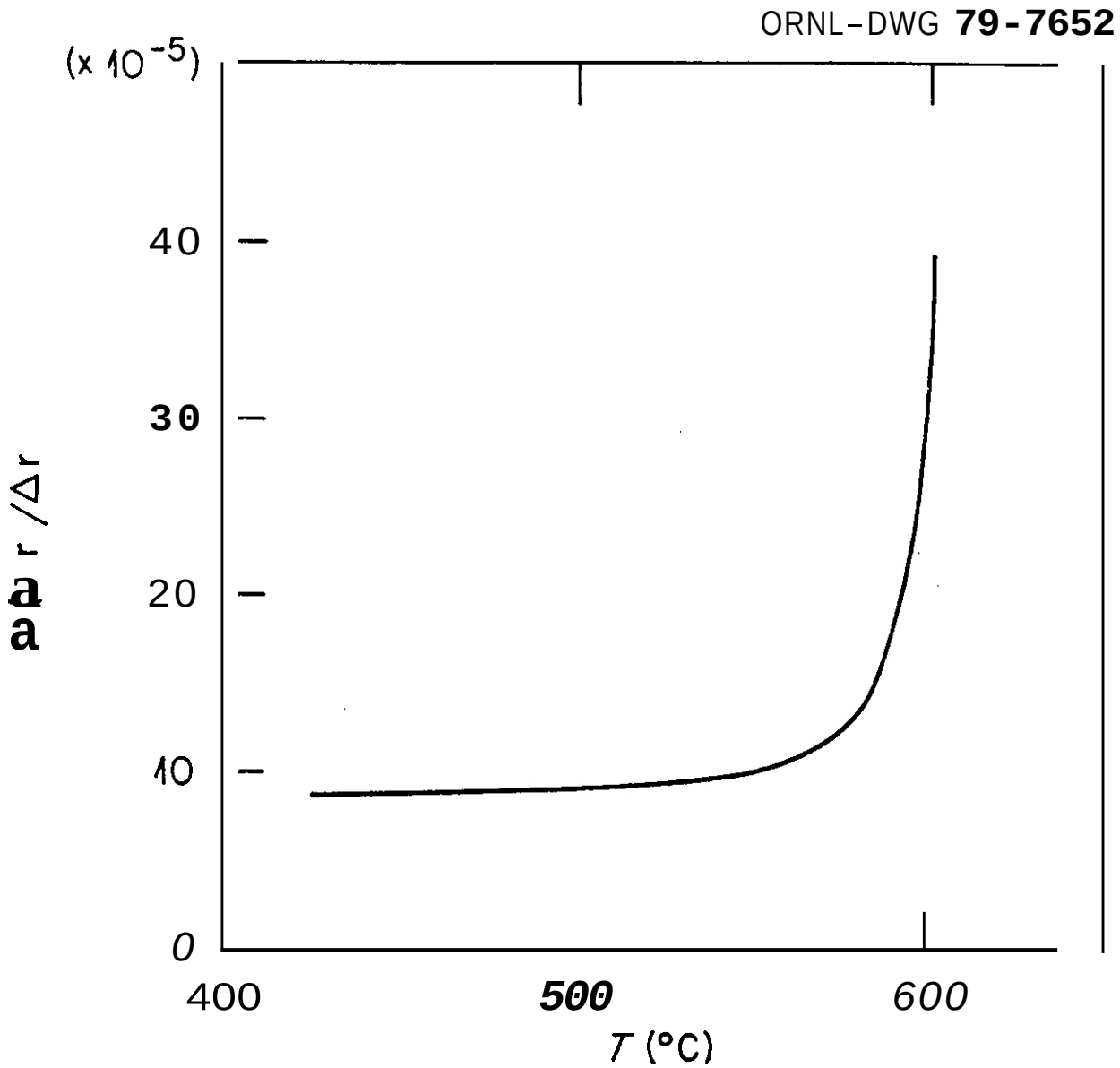

Figure 4. Difference in void radius computed with and without spacially inhomogeneous defect flux (from Ref. 6).

III. THE NUCLEATION OF SECONDARY DEFECTS

In order that irradiation produced defects should influence the irradiation response of material* they must first aggregate and such aggregates are called secondary defects. Further, the existance of separate secondary defects for interstitials and vacancies is necessary and such a separation can only occur under steady-state conditions when sinks for both species exist and in addition that interstitials have a bias for one sink type.[7] The initial aggregation is therefore a prerequisite for irradiation induced deformation and is a difficult area for experimental observation since, in general, all of the necessary information concerning the properties of small clusters has to be inferred from observations of the macroscopic defects after some growth has been achieved. Here we concentrate upon the nucleation of point defect aggregates, the precipitation of solute and impurity atoms will be treated in the following presentation. We shall treat the nucleation of two types of secondary defects, interstitial dislocation loops and cavities. A great deal of information is available on the nucleation of interstitial loops under electron irradiation in pure metals and alloys. In recent reviews Kiritani[8] and Yoshida[9] cover a wide range of observations. Several features of loop nucleation have now been clarified; even for ostensibly 'pure' metals the nucleation density is very sensitive to impurity atom concentrations, with levels in the *ppm* range being important; the rate controlling diffusion process depends upon the mobility of vacancies, at higher temperatures the vacancy migration energy controls the rate of growth of loops and the local increase in vacancy concentration adjacent to interstitial sinks can lead to the formation of vacancy clusters by thermal and/or irradiation induced diffusion of vacancies. The observed[8] nucleation density as a function of inverse temperature for gold and molybdenum are shown in Fig. 5. The separation into four significantly different temperature regimes is more clearly shown in Fig. 6 where the loop densities were calculated.[8] The highest temperature regime is not seen in Fig. 5 because of the very low densities and also these calculations did not include vacancy mobility. Region II is interpreted as nucleation dominated by (interstitial) impurity

*With the exception of irradiation enhanced diffusion which does not introduce new mechanisms of deformation.

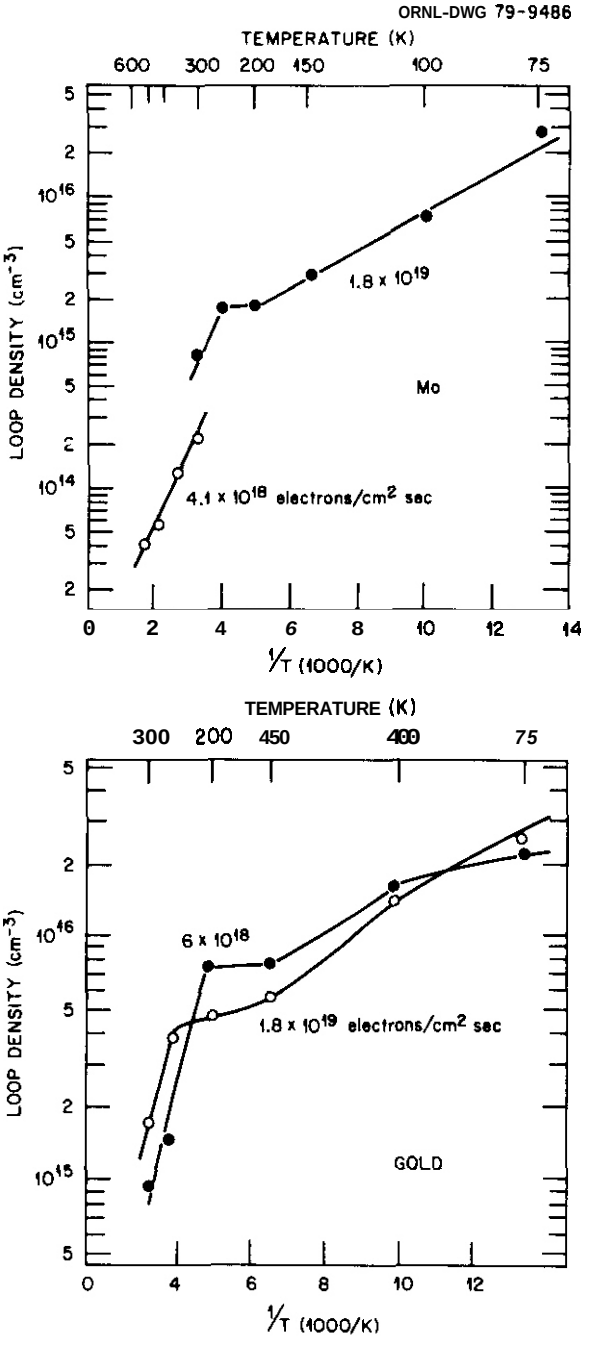

Figure 5. Interstitial loop density in e^- irradiated silver and gold (from Ref. 8).

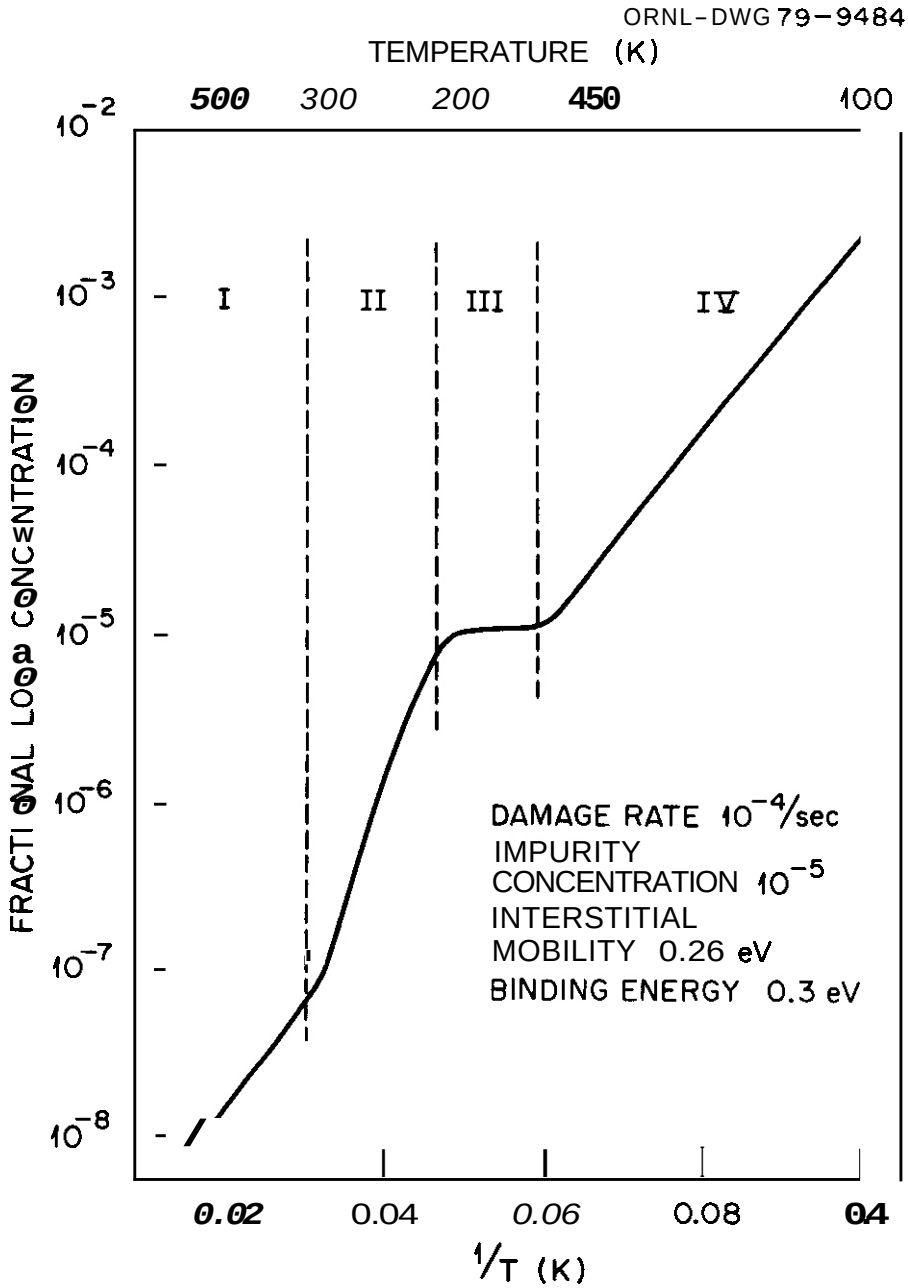

Calculated Variation in Interstitial Loop Density with Irradiation Temperature.

Figure 6. Calculated interstitial loop density as a function of temperature (from Ref. 8).

trapping; the apparent activation energies are 0.19 eV for Au and 0.18 eV for Mo, activation energies for other metals are in reference (8). These quantities are a combination of the free interstitial mobility and the free interstitial-impurity binding energy. The plateau region is heterogeneous nucleation on impurity atoms (here assumed to be present at ~10 ppm), whilst region IV is *either* nucleation under free interstitial diffusion or in conjunction with an impurity of lower binding energy than that associated with region II. These results are included to demonstrate the level of complication found for simple electron irradiation under 'ideal' conditions for very pure materials. Our concern is for technologically important materials under heavy ion or neutron irradiation and several new features have to be considered. The important role of impurities as heterogeneous nucleation sites has been established for pure metals, in technological alloys it can be expected to be dominant. Consequently careful measurements are required to separate self-diffusion processes and point defect trapping in interpreting the loop nucleation density. The very important part played by the segregation of impurities to the nucleating clusters is treated in the next presentation.[7] Another feature which is especially pertinent under CTR conditions is the influence of helium gas on the nucleation process. We shall discuss this further below with reference to cavity nucleation, but there is clear evidence that the presence of helium greatly influences the observed loop number density.[10,11] When the damage is caused by 14 MeV neutrons, with the consequent copious helium generation the loop nucleation is likely to be influenced to an extent which at present is not well understood. Further questions relating to the damage-rate dependence,[12] the presence of free surfaces (in electron and heavy ion simulation experiments),[13] and the presence of large diffusion gradients for defects (in heavy ion experiments)[14] must also be considered.

Even though there is general agreement that interstitial loop nucleation is completed very early in an irradiation, the final nucleation density and hence the dislocation density is sensitive to many influences which are not well characterized, particularly for technological steels and CTR irradiation conditions.

IV. THE NUCLEATION AND STABILITY OF CAVITIES*

The nucleation of voids is a more complicated process than that for interstitial loops discussed above because it arises from the mutual aggregation of more than one diffusing species. In the simplest case one must account for the flux of two species, interstitials, and vacancies, whilst in general the simultaneous arrival of helium or intrinsic gases is also necessary for the creation of stable embryo's. Cavities are special in that a three dimensional collection of vacancies is not a stable unit. Hence the appearance of two dimensional vacancy loops from cascades and from quenching (although in pure metals vacancy type stacking fault tetrahedra are observed).' The net vacancy flux to an embryo must be large enough to overcome the thermodynamic driving force for shrinkage by vacancy thermal emission for stable growth. This is simply conceptualized as a critical size or void nucleation barrier, below which a cavity is unstable and will shrink, and is strongly dependent upon damage rate, local microstructure and temperature. At elevated temperatures this size can be significant, Fig. 7 gives an example of the computed critical size for 316 stainless steel as a function of temperature for different dose rates.[15] There are three ways in which a cavity can appear in the system with sufficient size to grow as a void. First by statistical fluctuations, that is the out of equilibrium appearance of clusters of vacancies by thermodynamic accretion, secondly from high vacancy supersaturations in damage cascades. and thirdly, by the growth of gas bubbles up to the required size. At higher temperatures (the peak swelling temperature and above) it is clear that the latter is the only viable process. We therefore prefere to separate void nucleation in two stages. The first concerns the aggregation of gas atoms to form small gas bubbles, the void embryos, the second the growth/or simple existance of bubbles up to the critical size. The first stage has been treated using classical thermodynamical arguments[16] and by sophisticated numerical treatments which involve all three diffusing species.[17] A simpler approach in which only the motion of the helium was taken into account has also been given.[15,18] All of these methods are complicated and

** The cavity is used to cover both gas bubbles and voids; only when it is clear which type is dominant will the terms 'gas bubble' or 'void' be used.

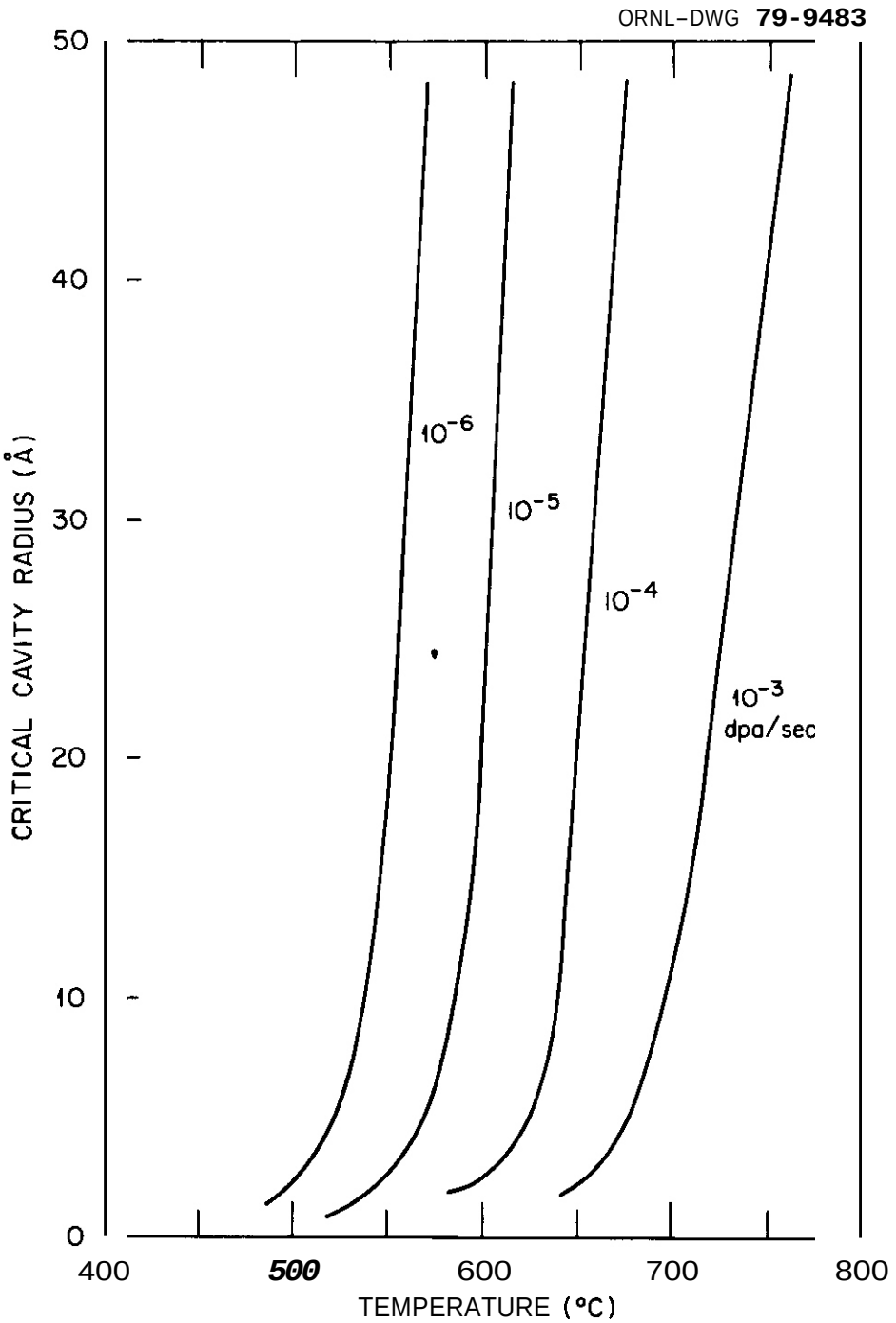

Calculated Critical Radii as a Function of Temperature for Various Dose Rates. $\rho_D = 2.6 \times 10^{10} cm/cm^3$

Figure 7. Critical cavity size as a function of temperature and dose rate (from Ref. 15).

depend upon poorly known quantities. For example, even the simplest picture of gas bubble nucleation requires a knowledge of an equation of state for statistically small ensembles of gas atoms and vacancies. Further, the role of impurity trapping, leading to heterogeneous nucleation *is* thought to be just as important as discussed previously for interstitial loops.[18] Typical calculated bubble densities as a function of inverse temperature for different assumed gas atom trap energies are shown in Fig. 8.[18] The high apparent Arrhenius energy can be explained (for interstitial helium motion) by means of a thermally activated non-saturable heterogeneous trap for gas atoms. In the calculations leading to Fig. 8 no assumptions were made as to the nature of the trap site other than the binding energy. Thus, the trap could be an interstitial loop, perhaps leading to the commonly observed feature of loops and voids apparently produced together, single solute atoms, precipitates, dislocation nodes and other lattice defects. We have insufficient evidence to clearly define the nature of the trapping site and all of the above possibilities have been observed. The direct observation of void embryos is not possible and therefore techniques other than TEM need to be brought to bear.

The second part of the void nucleation process, the critical size, is rather more amenable to experimental confirmation since, from Fig. 7, we see that for an appropriate choice of damage rate and temperature the critical size predicted theoretically is well within observational range in the TEM. and indeed a considerable body of evidence now exists which yields to this interpretation. Mazey and Nelson" have presented most convincing evidence from heavy ion irradiatins. but here we utilize a spectacular example from the work of Packan and Farrell. The material investigated was a 'pure' 316 type austenitic steel (17% Ni, 16.7% Cr, 2.5% Mo), irradiated under 4 MeV Ni ions after being preinjected with 1400 ppm helium. Preinjection has long been used to simulate the helium production during neutron irradiation, and to give consistant values of the void density. Notice that this is significantly different from the continuous production of gas under neutrons. The consequences have been discussed in some detail recently.[15,21] Upon preinjection we visualize the gas nucleating a large number of small bubbles, the following ion irradiation will allow only those

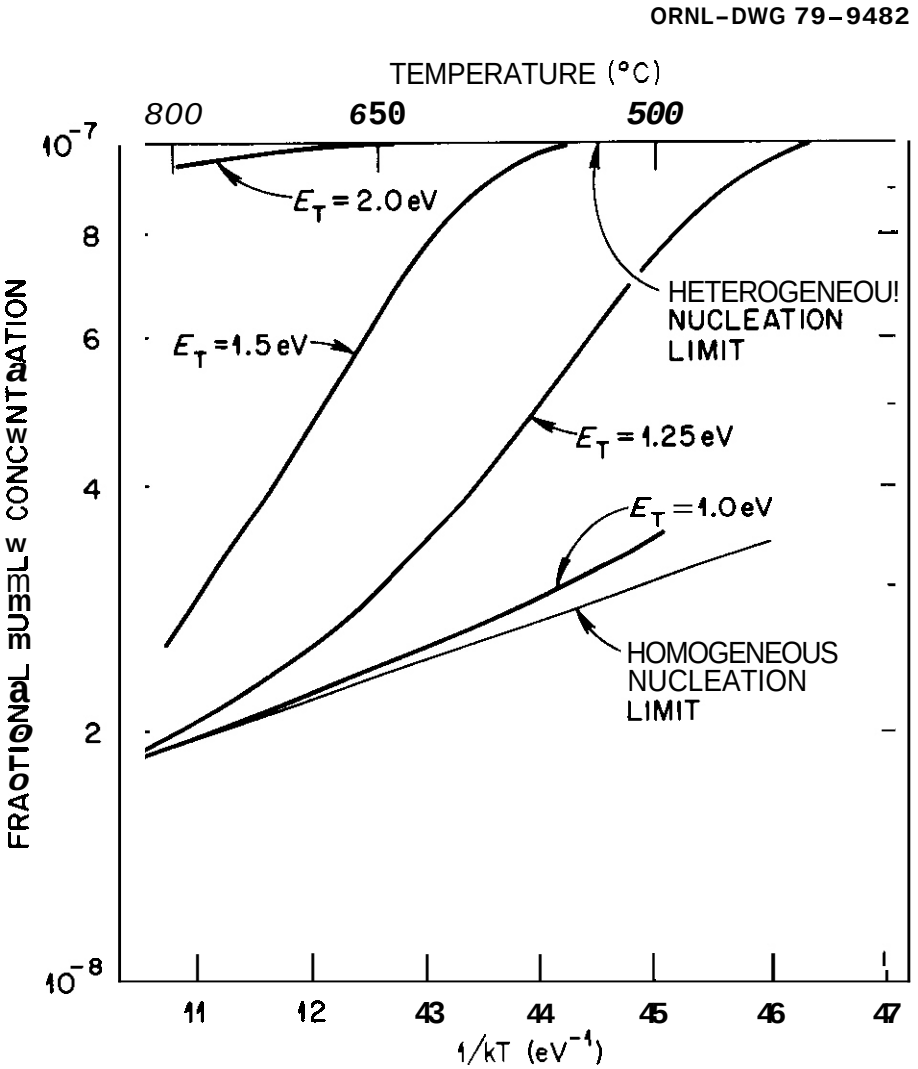

Calculated Bubble Concentration as a Function of 1/kT for Various Gas Atom-Trap Binding Energies.

Figure 8. Calculated bubble density in 316 stainless steel as a function of temperature for various gas atom trap-binding energies (from Ref. 18).

bubbles with a radius in excess of the critical size to grow. Thus, with the large amounts of injected gas in these experiments we would predict a bimodal cavity population consisting of growing voids and a stable background population of gas bubbles. Figure 9 shows this very clearly for two different experimental conditions, case (d) was for preinjection at room temperature, and case (c) at the temperature of the irradiation (625°C). The first case is clearly bimodal with a large (dominant) population of small cavities, the second case has a background population of less numbers, but larger size. The histograms for these two cases are shown in Fig. 10 and clearly highlight this effect. The differences between these two experiments are easily reconciled in the temperature at which the gas bubbles nucleated, the high temperature resulting in a smaller number of larger bubbles — hence in turn leading to a more evenly distributed bimodal population. Calculations using a distribution of cavity sizes shows the expected evolution of a bimodal population and the results are summarized in Fig. 11, essentially validating the physical model. This physical process has proved to be rather useful in a much wider area. For example, it was first introduced[15] as a clear concept to explain the observed sudden drop in 'void' numbers at high temperature, which seems to be an unusual feature of all irradiation conditions. For preinjected material this is explained in terms of the exponential rise in critical size with temperature (see Fig. 7) rapidly exhausting the cavities large enough to grow which resulted from the preinjection. Figure 12 demonstrates the results for particular calculations in 316 steel under nickel ion irradiation.[15] The effect is also useful in interpreting the appearance of an incubation dose and second swelling peak in neutron irradiated 316 steel[22] and in interpreting the possible effects of temperature changes on void swelling.[23] Useful though these simple arguments have been the complications arising from dose dependent effects, such as the evolving further detailed measurements like those mentioned above[19,20] to fully utilize the physical model and therefore allow its allow its extrapolation to CTR conditions.

In Figs. 10 and 11 we introduced the void size distribution as an observable feature of irradiation damage. The examples cited show that such measurements are a source of more detailed information. In fact, a great deal more informa-

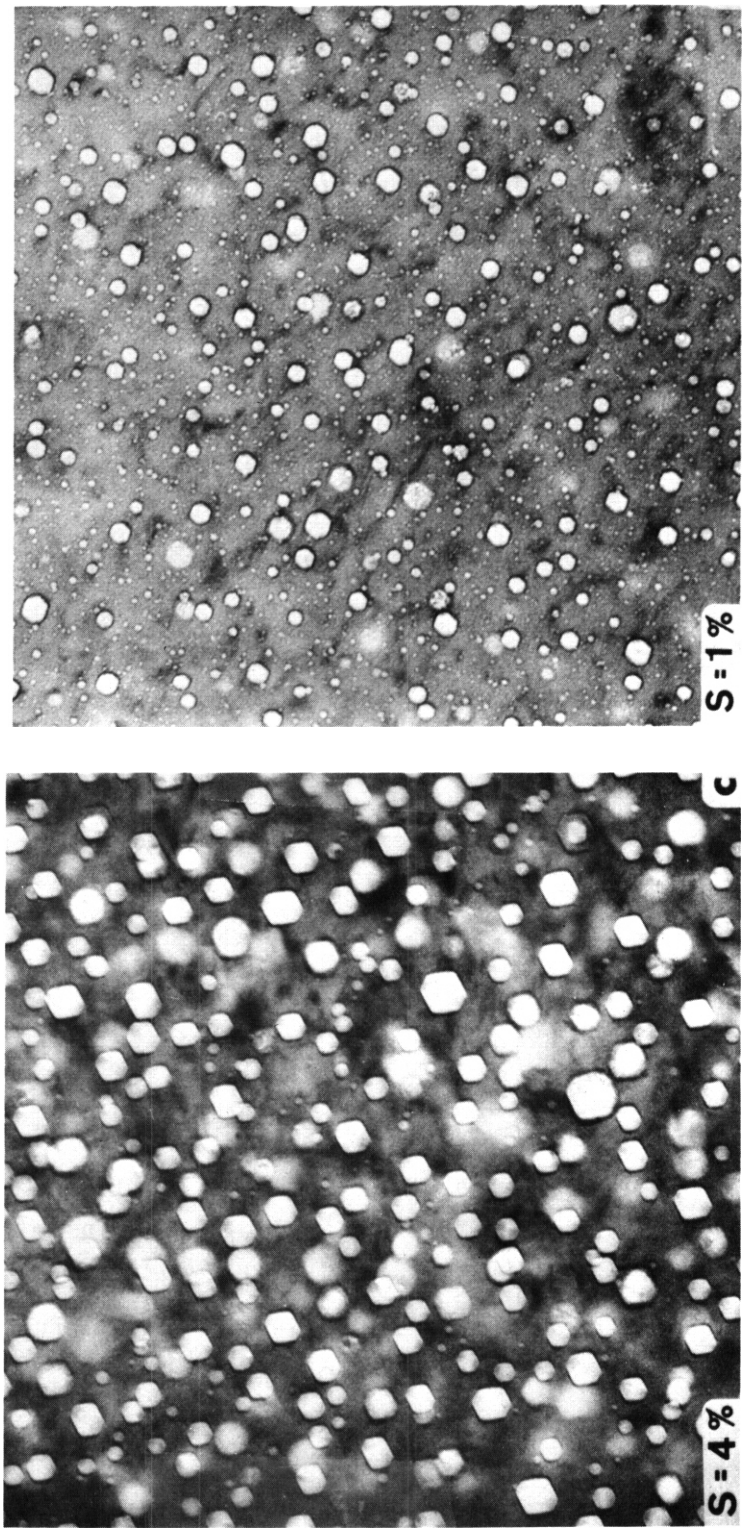

Figure 9. Electron micrograph of bimodel void populations in 'pure' 316 stainless steel at 70 dpa. Case (c) is for hot injected helium, case (d) for cold injected helium, both to 1400 ppm (from Ref. 20).

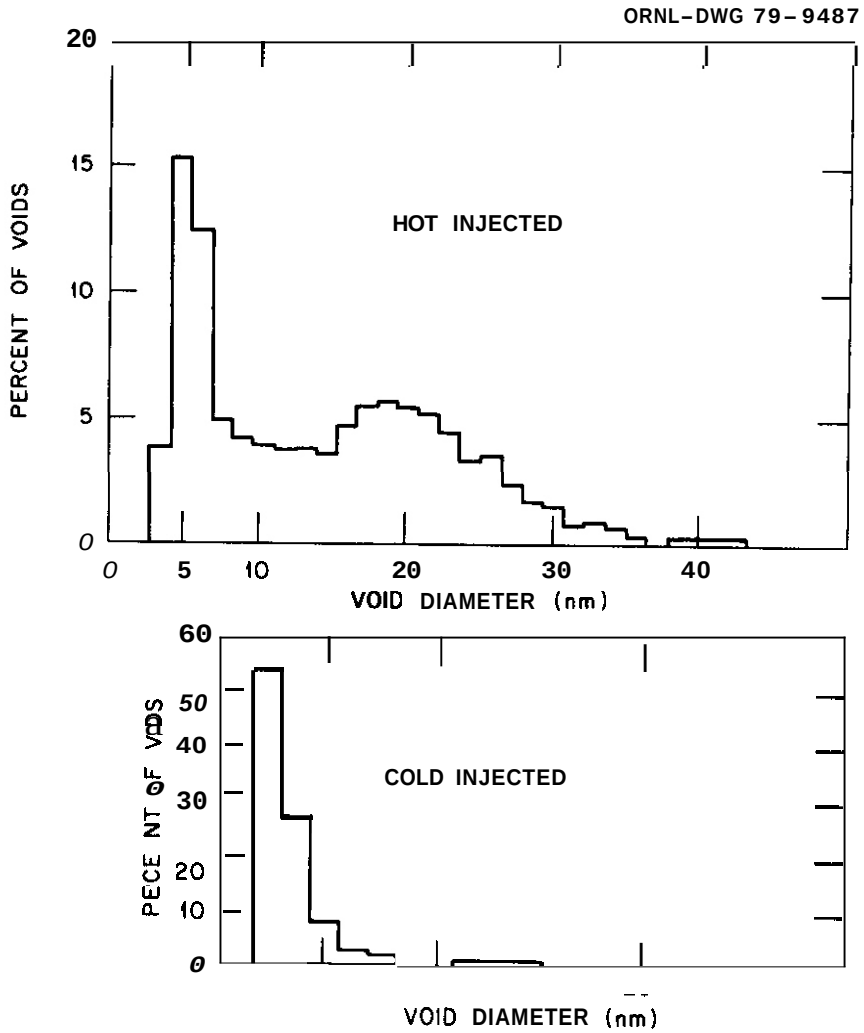

Void Size Distribution at 70 dpo and 625 °C with 1400 ppm Helium

Figure 10. Histograms of the void size distributions obtained from the micrographs shown in Fig. 9.

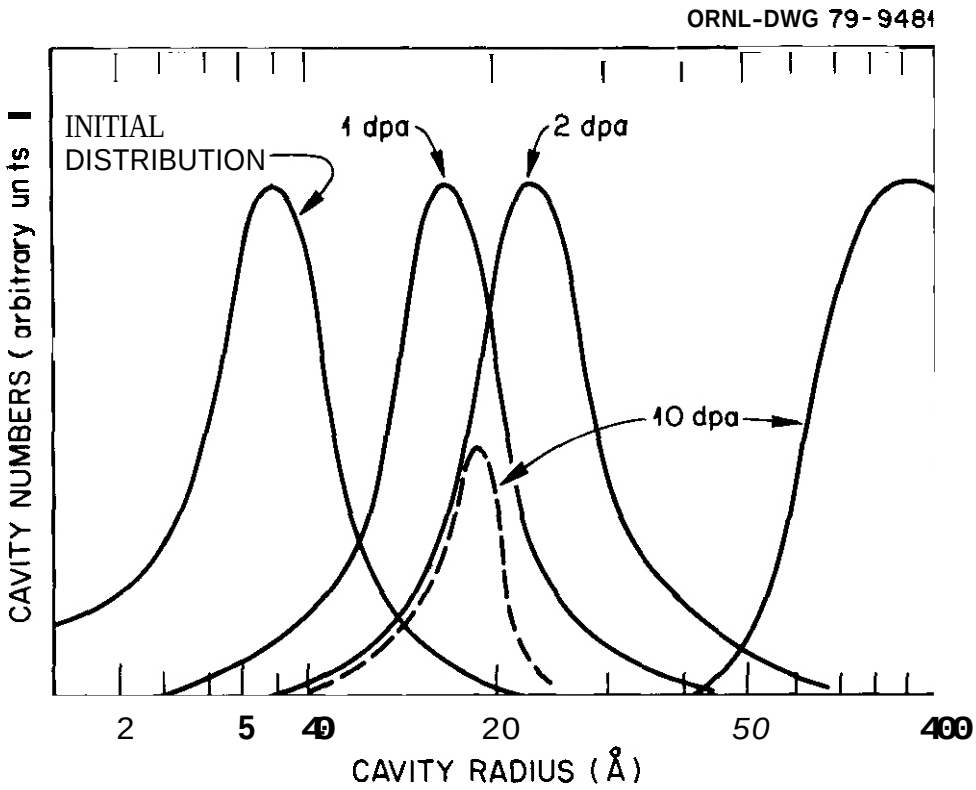

Calculated Cavity Size Distribution after 0,1,2 and 10 dpa at 550°C. CW. 316 Steel Under Neutron Irradiation Conditions. The Dotted Curve Represents Shrinking Cavities at 10 dpa.

Figure 11. The calculated evolution of the void size distribution in CW 316 steel under neutron irradiation conditions at 550°C. The dotted curve represents cavities which are shrinking at 10 dpa (from Ref. 23).

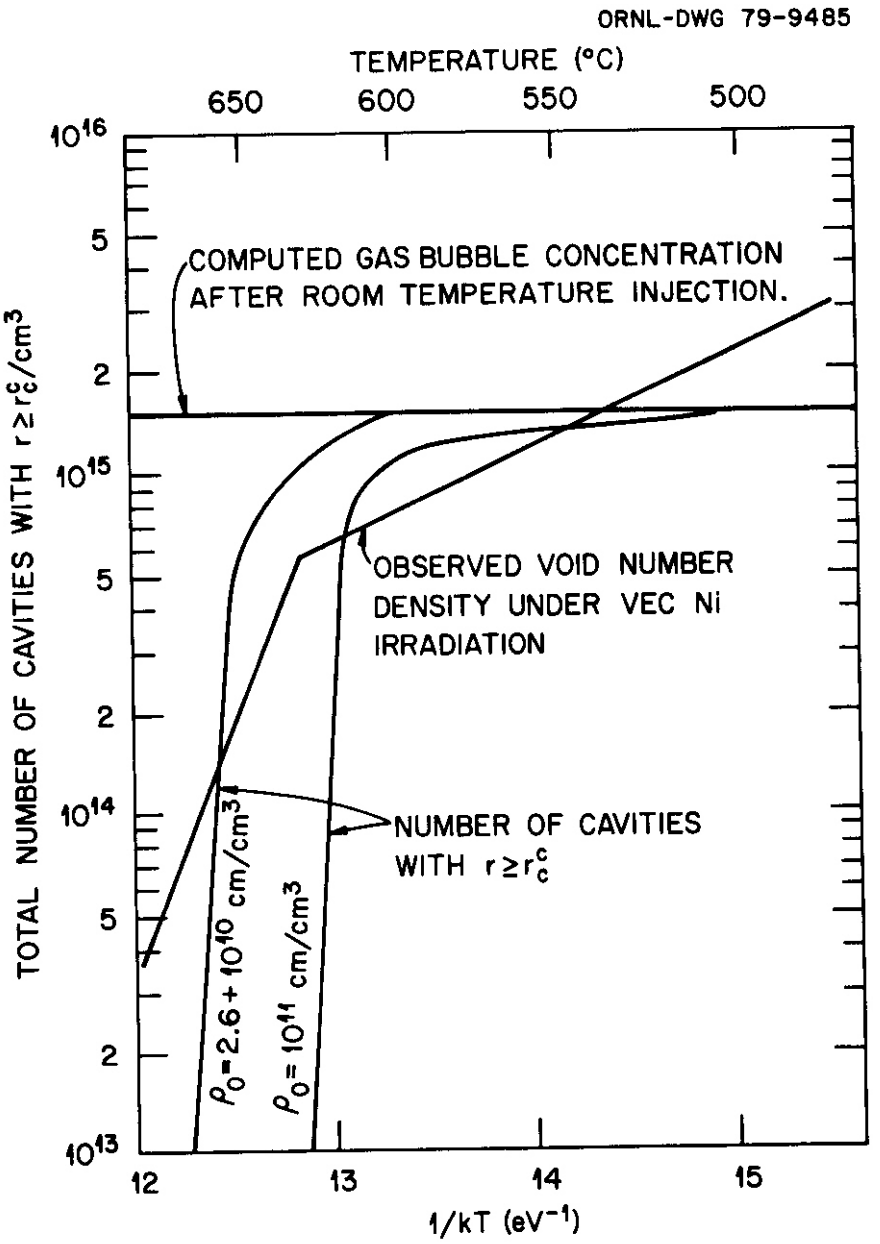

Comparison of Calculated and Observed Void Number Densities in S.T. 316 Steel as a Function of Temperature

Figure 12. Calculated observable void concentrations for VEC conditions shown, with the observed void densities (from Ref. 15).

tion can be derived if such size distributions can be accurately measured. However these principally concern questions of growth kinetics and are outside the range of the present discussion. Details are available in the literature.[24,25]

We have emphasized the role of helium in the nucleation kinetics of voids and shown how physical models based upon it can give a very successful interpretation of the available experimental results. In particular we would reemphasize the vital distinction between preinjected (or intrinsic) gas in simulation experiments and the continuous gas production under neutron irradiation conditions. Experimental observations under dual ion-gas injection irradiation conditions are vital to simulate CTR, and even FBR, environments and there is already a significant-body of evidence which emphasizes this.[21,26] We therefore highlight the whole area of inert gases in metals as a crucial one for understanding the response of materials to CTR irradiation environments.

V. SUMMARY

In this very brief note we have tried to highlight some of the important new quantities which need experimental verification and characterization of further our understanding of the irradiation damage processes in materials in CTR environments. We have particularly emphasized the need to thoroughly understand the available simulation experiment conditions so that a proper correlation with the, as yet unobtainable, CTR conditions can be made. We have only focused upon the primary stages of the damage process and the nucleation of secondary defects. This should in no way be taken as implying that our understanding of the more basic quantities, such as diffusion in complex alloys, surface energies, stacking fault-energies, dislocation bias values, trap nature and binding energies, and phase stability (not segregation) is anywhere near adequate and further work is needed here as well as in the rather more exotic fields discussed in the body of the paper.

REFERENCES

1. K. L. Merkle, Radiation Damage in Metals, N. L. Peterson and S. D. Herkness, eds., ASM Metals Park, Ohio (1976) p. 58.

2. B. L. Eyre and D. M. Maher, Phil. Mag. 24, 767 (1971).

3. R. Bullough, B. L. Eyre, and K. Krishan, Proc. Roy. Soc. Lond. A346, 81 (1975).

4. A. Goland, Proceedings of the ANS Topical Meeting on Fusion Reactor Materials, Miami Beach, Florida, January 29-31, 1979, paper J-2; to be published in Journal of Nuclear Materials.

5. See, for example, H. L. Heinish and J. O. Schiffgens, Proceedings of the ANS Topical Meeting on Fusion Reactor Materials, Miami Beach, Florida, January 29-31, 1979, paper H-11; to be published in Journal of Nuclear Materials.

6. L. K. Mansur, W. A. Coghlan, and A. D. Brailsford, Proceedings of ANS Topical Meeting on Fusion Reactor Materials, Miami Beach, Florida, January 29-31, 1979, paper L-9; to be published in Journal of Nuclear Materials.

7. H. Wiedersich, this workshop.

8. M. Kiritani, Progress in the Study of Point Defects, University of Tokyo Press, Doyama and Yoshida, eds., Tokyo (1977) p. 247.

9. S. Yoshida, Progress in the Study of Point Defects, University of Tokyo Press, Doyama and Yoshida, eds., Tokyo (1977) p. 195.

10. D. S. Gelles and F. A. Garner, Proceedings of the ANS Topical Meeting on Fusion Reactor Materials, Miami Beach, Florida, January 29-31, 1979, paper L-13; to be published in Journal of Nuclear Materials.

11. O. J. Mazey, private communication, to be published.

12. M. R. Hayns, J. Nucl. Mater. 56, 267 (1975).

13. M. R. Hayns and R. C. Perrin, AERE Harwell Research Report AERE R 7934 (1975), p. 188, (Proceedings of the Consultants Symposium on Irradiation Produced Voids, September 9-11, 1974, ed. R. S. Nelson; and M. R. Hayns U. S. ERDA CONF-751006-P1 (1975) p. 764.

14. L. K. Mansur, Nucl. Technol. 40, 1 and 5 (1978).

15. M. R. Hayns, AERE Harwell Research Report AERE R 8806 (1977).

16. K. C. Russell and D. H. Hall, J. Nucl. Mater. 18, 545 (1973).

17. H. Wiedersich and J. L. Katz, Proceedings of the Workshop on Correlation of Neutron and Charged Particle Damage, U. S. ERDA CONF-760673, 21 (1976). See also, B. 0. Hall, Proceedings of the ANS Topical Meeting on Fusion Reactor Materials, Miami Beach, Florida, January 29-31, 1979, paper H-15; to be published in Journal of Nuclear Materials.

18. M. R. Hayns and M. H. Wood, Proc. Roy. Soc. Lond. to be published.

19. D. J. Mazey and R. S. Nelson, Proceedings of the ANS Topical Meeting on Fusion Reactor Materials, Miami Beach, Florida, January 29-31, 1979, paper C-20; to be published in Journal of Nuclear Materials.

20. N. H. Packan and K. Farrell, Proceedings of the ANS Topical Meeting on Fusion Reactor Materials, Miami Beach, Florida, January 29-31, 1979, paper L-11; to be published in Journal of Nuclear Materials.

21. R. Bullough, M. R. Hayns, and M. H. Wood, Proceedings of the ANS Topical Meeting on Fusion Reactor Materials, Miami Beach, Florida, January 29-31, 1979, paper H-2; to be published in Journal of Nuclear Materials.

22. M. R. Hayns, J. Gallagher, and R. Bullough, to be published in Journal of Nuclear Materials.

23. M. R. Hayns, AERE Harwell Research Report TP 758, to be published in Journal of Nuclear Materials.

24. M. H. Wood and M. R. Hayns, AERE Harwell Research Report AERE R 9178 (1978).

25. L. K. Mansur, P. R. Okamoto, A. Taylor, and Che-Yu Li, Nucl. Met. 18, 509 (1973).

26. See, for example, K. Farrell and N. H. Packan, Proceedings of the ANS Topical Meeting on Fusion Reactor Materials, Miami Beach, Florida, January 29-31, 1979, paper L-12; to be published in Journal of Nuclear Materials.

A SUMMARY OF THE CURRENT UNDERSTANDING OF THE SECONDARY DAMAGE MICROSTRUCTURE

H. Wiedersich
Materials Science Division
Argonne National Laboratory
Argonne, Illinois 60439

I. INTRODUCTION

During elevated temperature irradiations with energetic neutrons, ions or electrons, the microstructure of alloys undergoes significant changes accompanied by corresponding changes in physical properties. Detailed information on various aspects of radiation-induced microstructural effects and property changes can be found in several recent proceedings. [1-3] The preceeding paper by M. R. Haynes summarizes the defect production and the nucleation of small defect aggregates during irradiation. Here, we will discuss the development of the microstructure on a somewhat grosser scale.

After a short characterization of the dynamic state of a crystalline material during irradiation we will address (a) the void swelling phenomenon; (b) radiation-enhanced, diffusion-induced processes such as radiation-induced coarsening; and (c) radiation-induced processes such as radiation-induced second phases and the spatial redistribution of phases in multiphase alloys.

II. THE DYNAMIC STATE DURING IRRADIATION

For a conceptual understanding of the microstructural developments during irradiation a treatment by chemical rate theory is most useful. [4-6] This theory assumes that defects are produced randomly throughout the material. Defects are classified as "imnobile", e.g., collapsed vacancy loops or void embryos in the core of displacement cascades, and "mobile", e.g., interstitials, vacancies, small clusters of these point defects, point defect-solute complexes, helium and other transmutation products. The interstitial- and vacancy-type mobile defects diffuse,

except at low temperatures, and cease to exist by mutual recombination throughout the material or by annihilation at stationary sinks such as dislocations, voids, surfaces and grain boundaries. Defect annihilation at sinks induces defect fluxes from the interiors of grains to the spatially discrete sinks. These fluxes are the predominant cause of microstructural development during irradiation. In the rate theory description, the defect losses by fluxes to descrete sinks are taken into account by loss rate constants called "sink annihilation probabilities" [4] or "sink strength" [5,6] and average defect concentrations are calculated.

For an appreciation of the types and scale of microstructural changes that can be expected in different temperature regimes, it is useful to consider the quasi-steady-state, average concentrations of mobile defects that are achieved during irradiation at const-ant displacement rate after an initial transient. At high temperatures, all point defects diffuse fast and, hence, their concentration does not rise significantly above the thermal equilibrium value; the rise is therefore insufficient for nucleation of interstitial loops or voids; moreover, thermal annealing eliminates incipient microstructural changes.

At low temperatures, at least one of the two principal types of defects, in metals usually the vacancy type, is essentially imnobile. Its concentration builds to a level limited by diffusive or spontaneous recombination, thereby eliminating any significant long range diffusion processes. The microstructural changes in this temperature range are thus limited to a high density of point defects and small defect clusters, up to sizes on the order of those produced directly by cascades.

Between these two temperature regimes both vacancies and interstitials annihilate, at least in part, at pre-existing or radiation-induced sinks, because even the slower defect diffuses fast enough to limit recombination as a defect loss mechanism. In this intermediate temperature regime, typically 0.3 to 0.6 of the absolute melting temperature, major changes of the microstructure on a scale above the resolution limit of conventional transmission electron microscopy (TEM) are induced or accelerated by irradiation. Generally, the high supersaturation of point defects at the lower end of this temperature regime causes profuse nucleation of interstitial loops and vacancy aggregates and, hence, leads to a high density of microstructural features. With increasing temperature, defect supersaturations

decrease. Consequently, fewer defect aggregates nucleate and coarser microstructures result. In the following sections we will touch on several distinct types of microstructural changes that occur during irradiation.

111. VOID SWELLING

In contrast to other microstructural changes during irradiation, to be discussed later, void swelling can occur only when a partial separation of interstitial- and vacancy-type defects is produced by preferential annihilation of interstitials and/or vacancies at specific types of sinks. The stronger elastic interaction of interstitials with dislocations than that of vacancies with dislocations is recognized as the major cause of this bias. The development of the dislocation structure in an annealed material usually starts with faulted loops. These loops grow, unfault, and eventually interact with other loops and existing dislocations to form dislocation networks as illustrated in Fig. 1. [7] The development of the major microstructural features in an annealed austenitic steel during electron irradiation is shown in a quantitative fashion in Fig. 2. [8] The number density of loops decreases as they interact and form dislocation networks, which in turn leads to an increase in the total dislocation density ρ_d. Saturation of ρ_d is approached with increasing dose. Generally, nucleation of loops as well as of voids ceases after low doses as can be deduced from peaks in the number densities, see Fig. 2. Observed decreases in void number densities with dose are likely caused by a process similar to Ostwald ripening or, sometimes, by void coalescence. The growth of surviving voids more than compensates for the decrease in number density as evidenced by a monotomic increase of the fractional void volume, $\Delta V/V_o$.

Typical void microstructures at a fixed dose are illustrated as a function of irradiation temperature in Fig. 3. [9] Consistent with the expectations outlined in the previous section, the void number density decreases with increasing temperature and the volume attains a maximum at intermediate temperatures where few defects are lost by recombination and thermal annealing is sufficiently slow to permit the nucleation of defect clusters at moderate number densities.

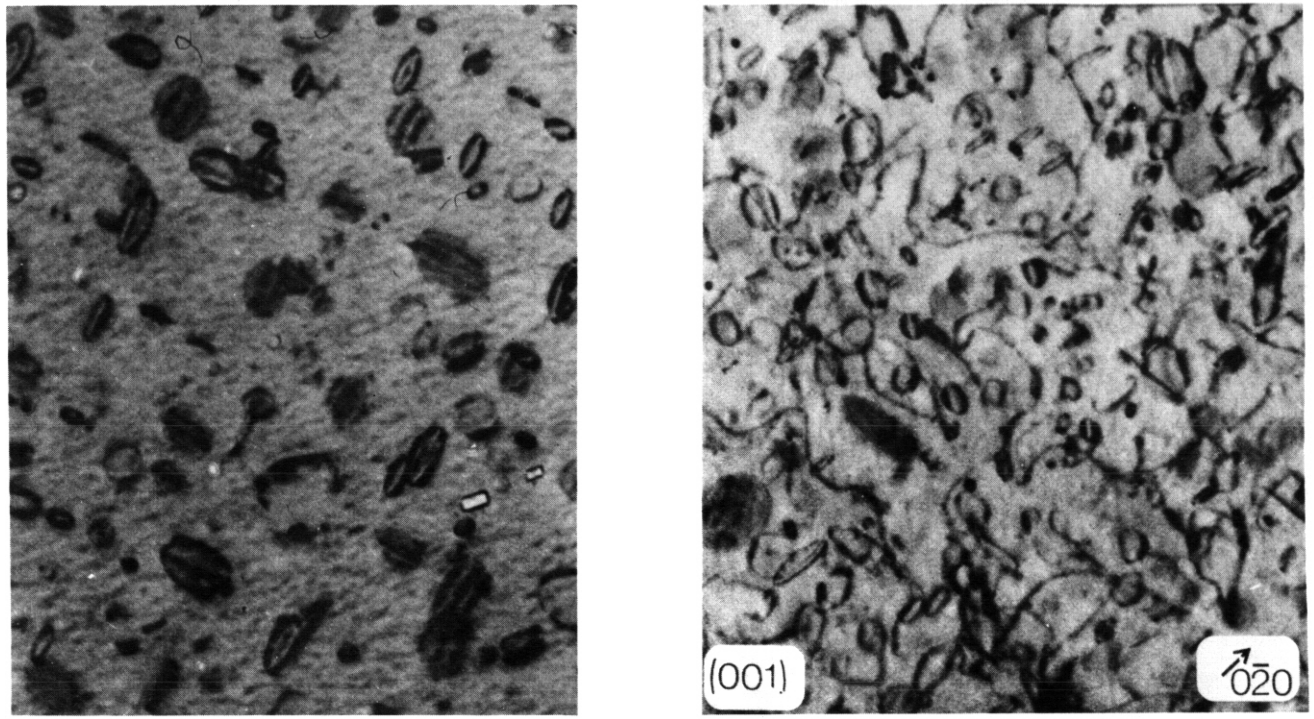

a b

Fig. 1. Dislocation structure development in a Ni-12.8 at. % Al alloy during Ni-ion bombardment at 530°C. (a) Interstitial loops at 1.8 dpa. (b) Loops and network dislocations at 5.5 dpa [7]

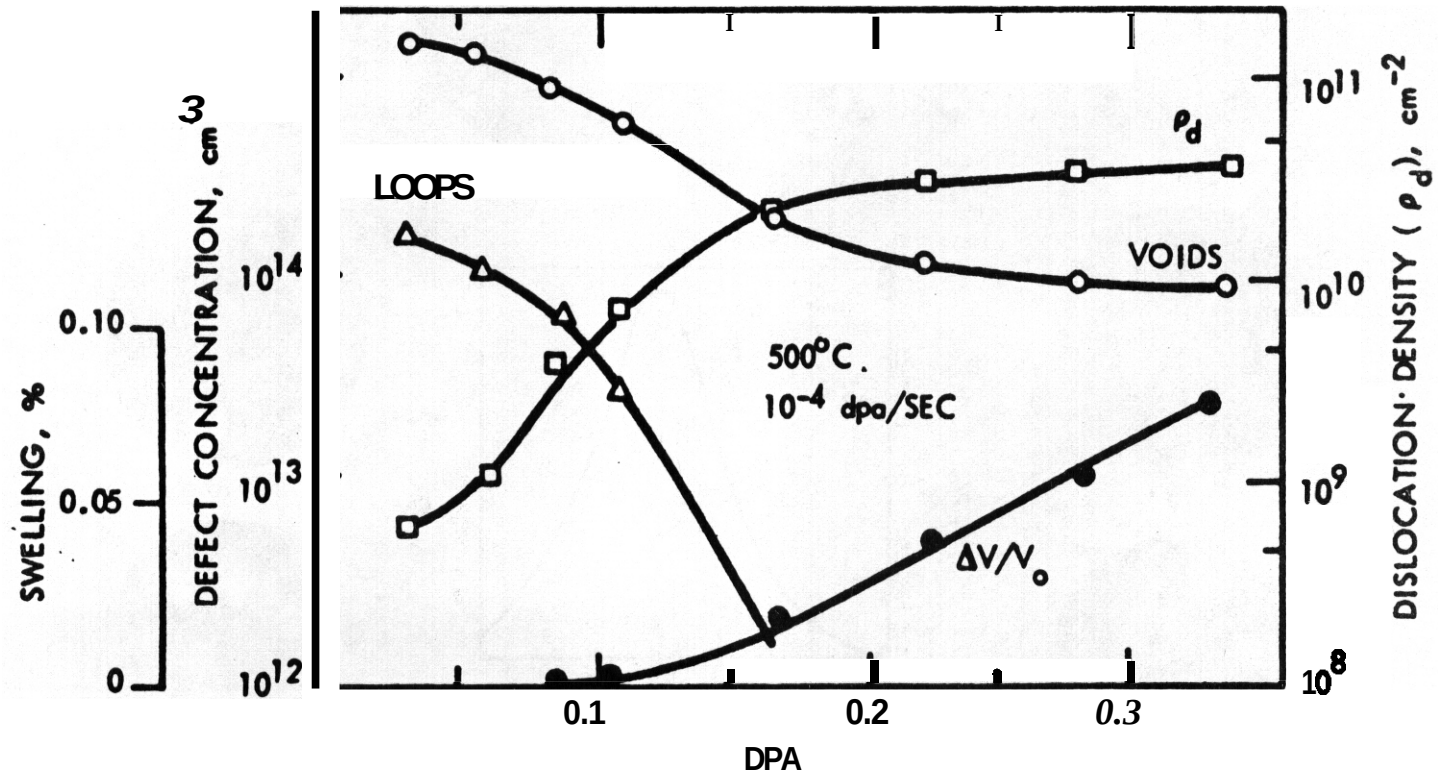

Fig. 2 Void and interstitial loop number densities, swelling $\Delta V/V$ and network dislocation density as function of dose for solution annealed type 316 stainless steel, irradiated with 1.0 MeV electrons at 500°C. [8]

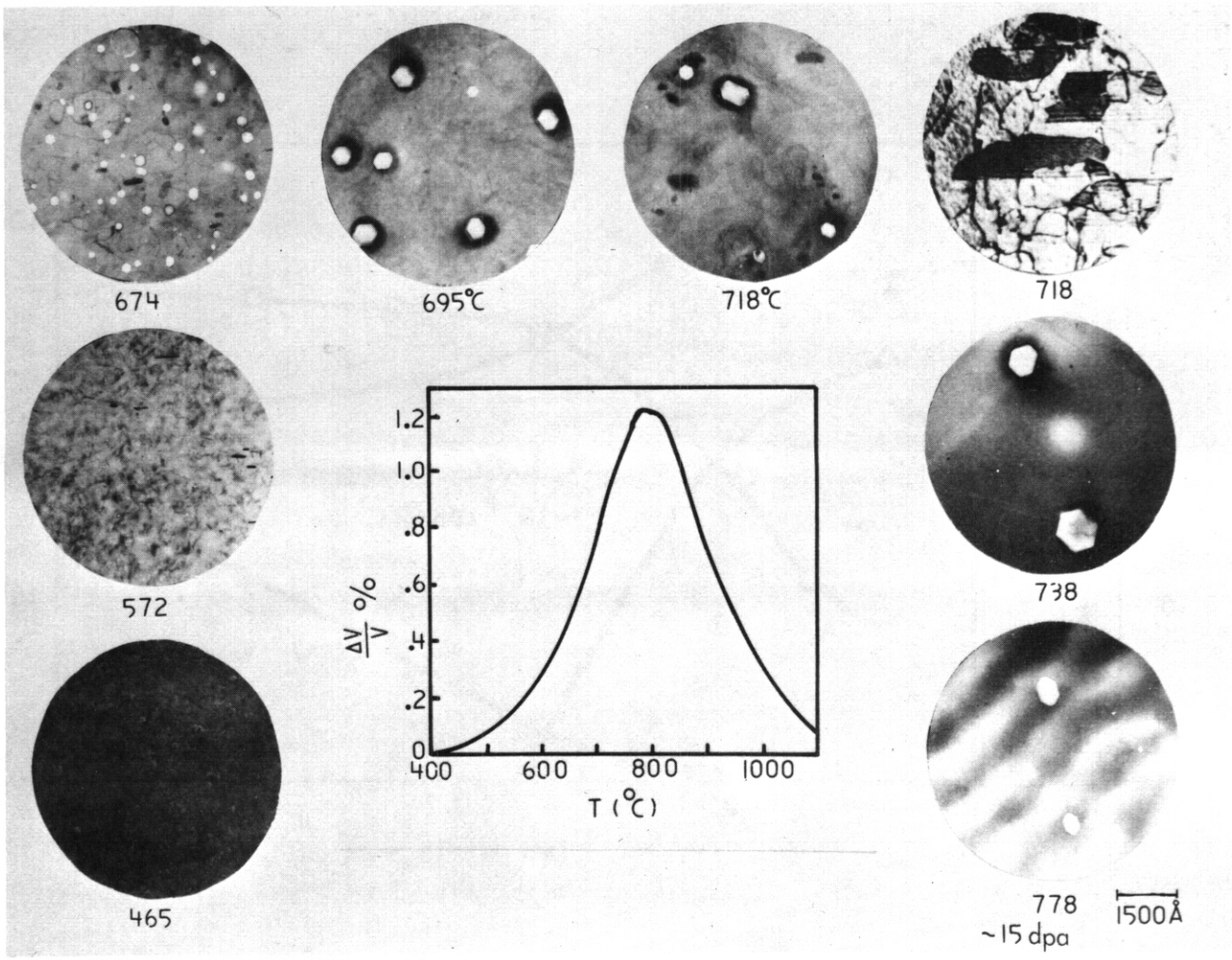

Fig. 3. Micrographs of a Ti-14.4 at. % Al alloy nickel-ion bombarded to a approximately 15 dpa at the temperatures indicated. The curve shows the calculated swelling as function of temperature. Courtesy of D. I. Potter.

Usually, voids and dislocation loops are distributed fairly randomly throughout the material with some exceptions. In a number of cases, many of the initial voids are observed in close proximity to existing dislocations. Void and loop denuded zones occur near surface and grain boundary sinks. In some materials interstitial loops are aligned in strings or rafts. The most striking non-random defect cluster distributions are ordered void arrays in which the voids form a superlattice, usually with the same type of unit cell and orientation as the host metal lattice. Examples of ordered void arrays, shown in Fig. 4, are taken from the work of Loomis et al. [10] The figure shows that the perfection and temperature range of ordered void arrays in Nb depend on the oxygen content.

IV. RADIATION-ENHANCED MICROSTRUCTURAL PROCESSES

Diffusion of substitutional elements in crystalline solids generally involves point defects. It has long been recognized that the radiation-produced excess point defects accelerate diffusion processes. Figure 5 illustrates the calculated enhancement of the diffusion coefficient for a species diffusion by a vacancy mechanism. In the intermediate and low temperature range, diffusion is greatly enhanced by irradiation. Values of the diffusion coefficient which can lead to significant microstructural changes in reasonable times are maintained to significantly lower temperatures during irradiation than without irradiation. Note that interstitials contribute to the enhancement of diffusion. However, increased recombination at low temperature limits long range diffusion and, hence, significant redistribution of alloy components on a microstructural scale.

The calculations for Fig. 5 are based on reaction rate theory which yields spatially averaged defect concentrations and diffusion coefficients. [4] Complications arise near defect sinks where defect concentrations and diffusion coefficients become strongly space dependent. Furthermore, defect flux induced segregation, to be discussed in the next section, may overshadow any effects of diffusion enhancement in the vicinity of defect sinks. As an example of a radiation-enhanced, diffusion-controlled

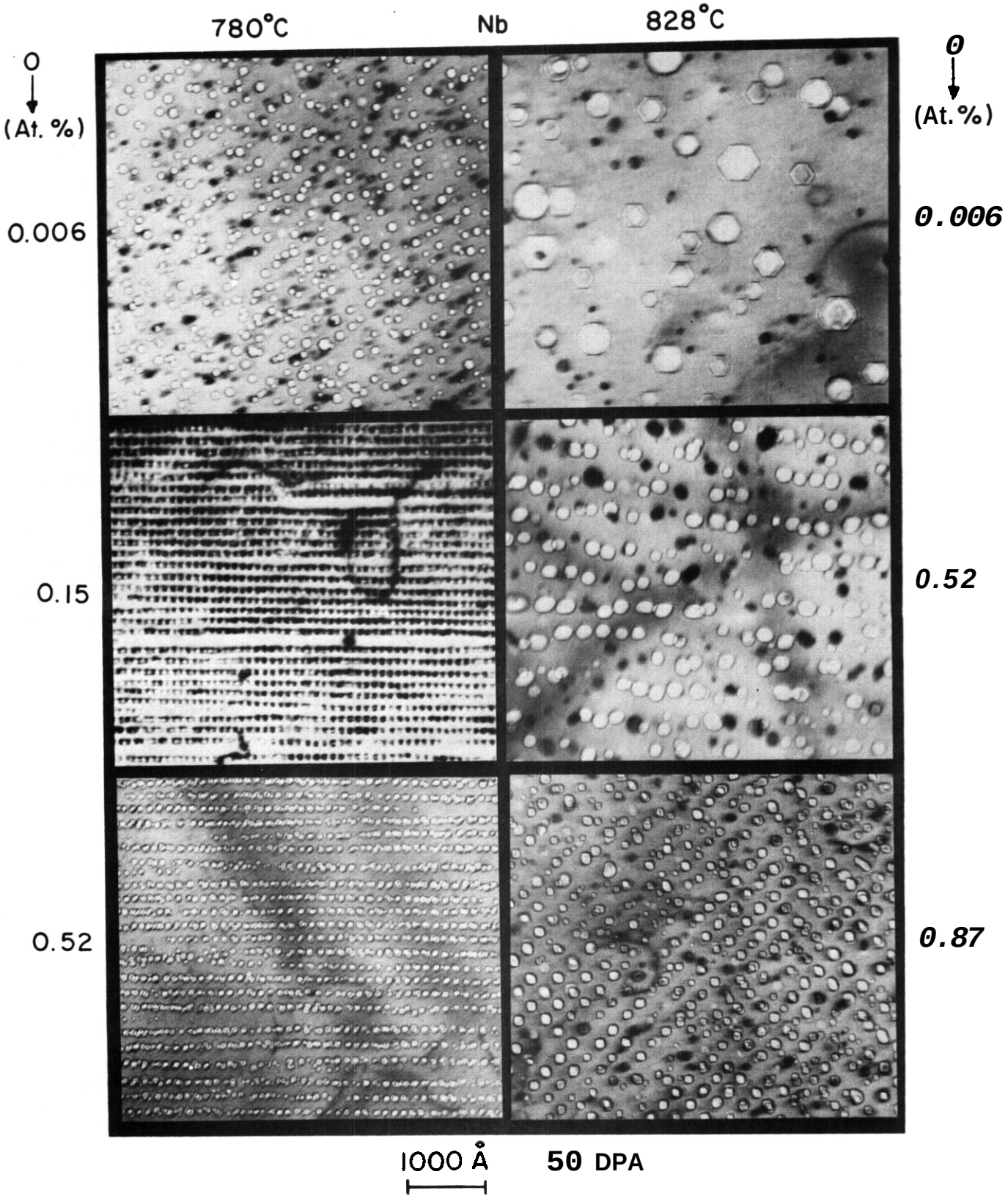

Fig. 4. Ordered Voids in Nb–O alloys after Ni-ion bombardment at 780°C and at 828°C to 50 dpa. Note that a higher oxygen concentration is required at the high temperature in order to form a well-ordered void lattice. [10]

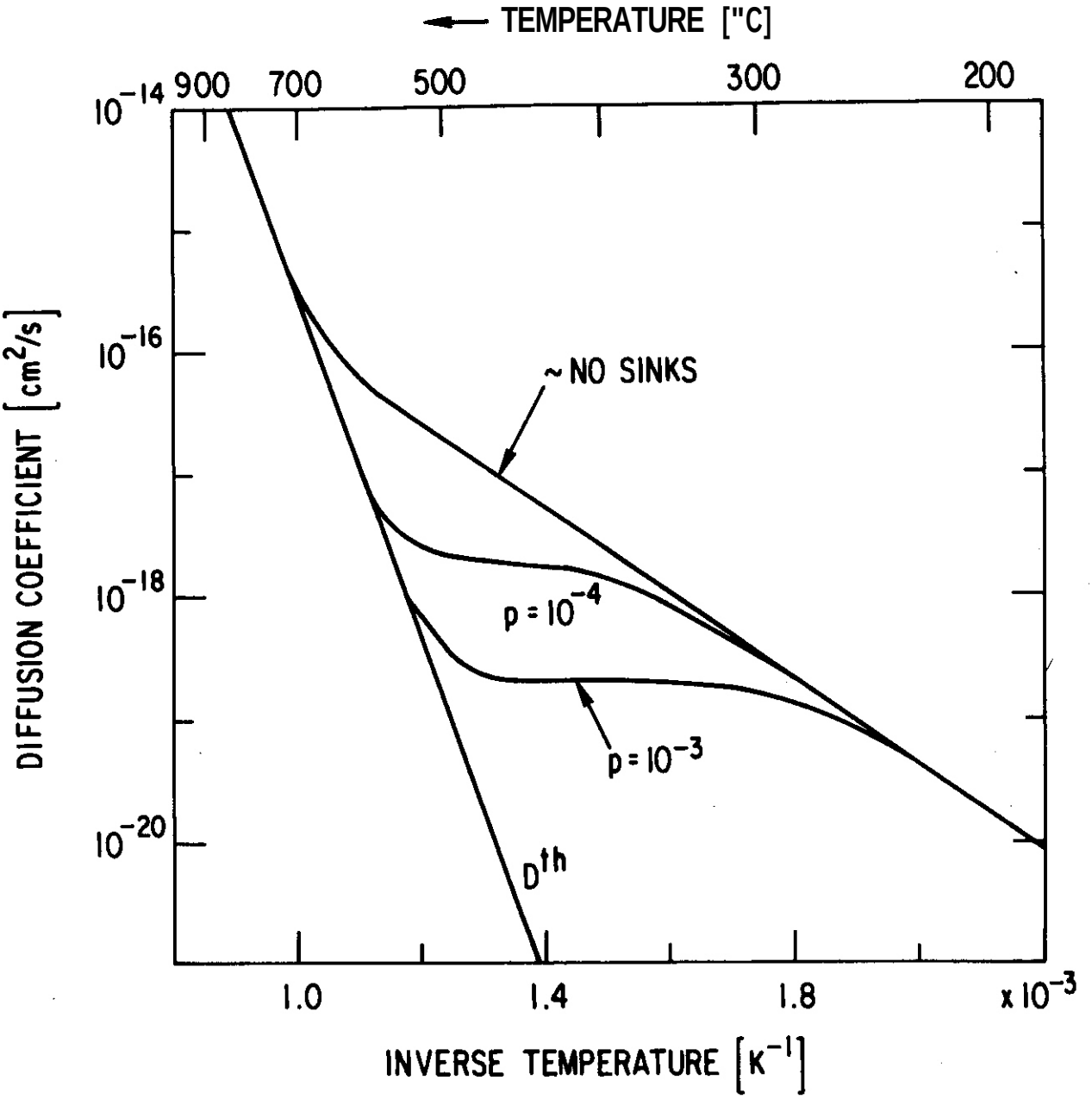

Fig. 5. Diffusion coefficient as function of inverse temperature calculated from rate theory for a nickel based substitutional alloy. Displacement rate used was 10^{-6} dpa/s. The sink density is characterized by the sink annihilation probability p. p^{-1} is the average number of jumps of a defect between creation and annihilation at a sink. The thermal diffusion coefficient D^{th} is shown for comparison.

microstructural process, we will discuss precipitate coarsening in γ/γ' alloys. The γ'-precipitates are ordered A_3B intermetallics ($L1_2$) that form coherently with the fcc disordered matrix and often exhibit little if any lattice parameter misfit. Therefore, coarsening can be studied without the undue interference from defect sinks that was alluded to before.

Coarsening or Ostwald ripening occurs by growth of large particles at the expense of smaller ones. The driving force is the reduction of interfacial energy. According to the Lifschitz-Slyozov-Wagner theory the average particle diameter $\bar{a}^3 - \bar{a}_0^3 = kt$. The rate constant k is proportional to the diffusion coefficient. Figure 6, taken from the work of Potter and McCormick, illustrates that coarsening of a Ni-12.8 at. % Al alloy during irradiation at various temperatures follows this relation well and, hence, can be considered as Ostwald ripening. [11] However, the rate constant k (which is proportional to the ordinate value at any fixed dose, e.g. 1 dpa, is greatly enhanced relative to that for thermal aging. In Fig. 7 coarsening rate constants for a Ni-12.7 at. % Si during irradiation are compared with those calculated on the basis of rate theory assuming that Si atoms act as immobile or mobile traps for interstitials, or do not trap interstitials. [12] The results indicate that precipitate coarsening under irradiation can be described as a radiation-enhanced diffusion process in the Ni-A1 and the Ni-Si systems. Some complications that arise from radiation-induced segregation will be discussed later.

V. RADIATION-INDUCED PHASE CHANGES

Three principally different types of radiation-induced phase changes can be distinguished. The changes may be caused by (a) the presence of excess difects, (b) displacement disordering and (c) radiation-induced local compositional changes.

The presence of excess interstitials and vacancies increases the free energy of a phase. Maydet and Russel suggested that as a consequence, shifts in phase boundaries should occur. [13] The energy contribution from excess defects are usually small compared to typical energy differences between neighboring phases. Moreover, only the difference in the energy

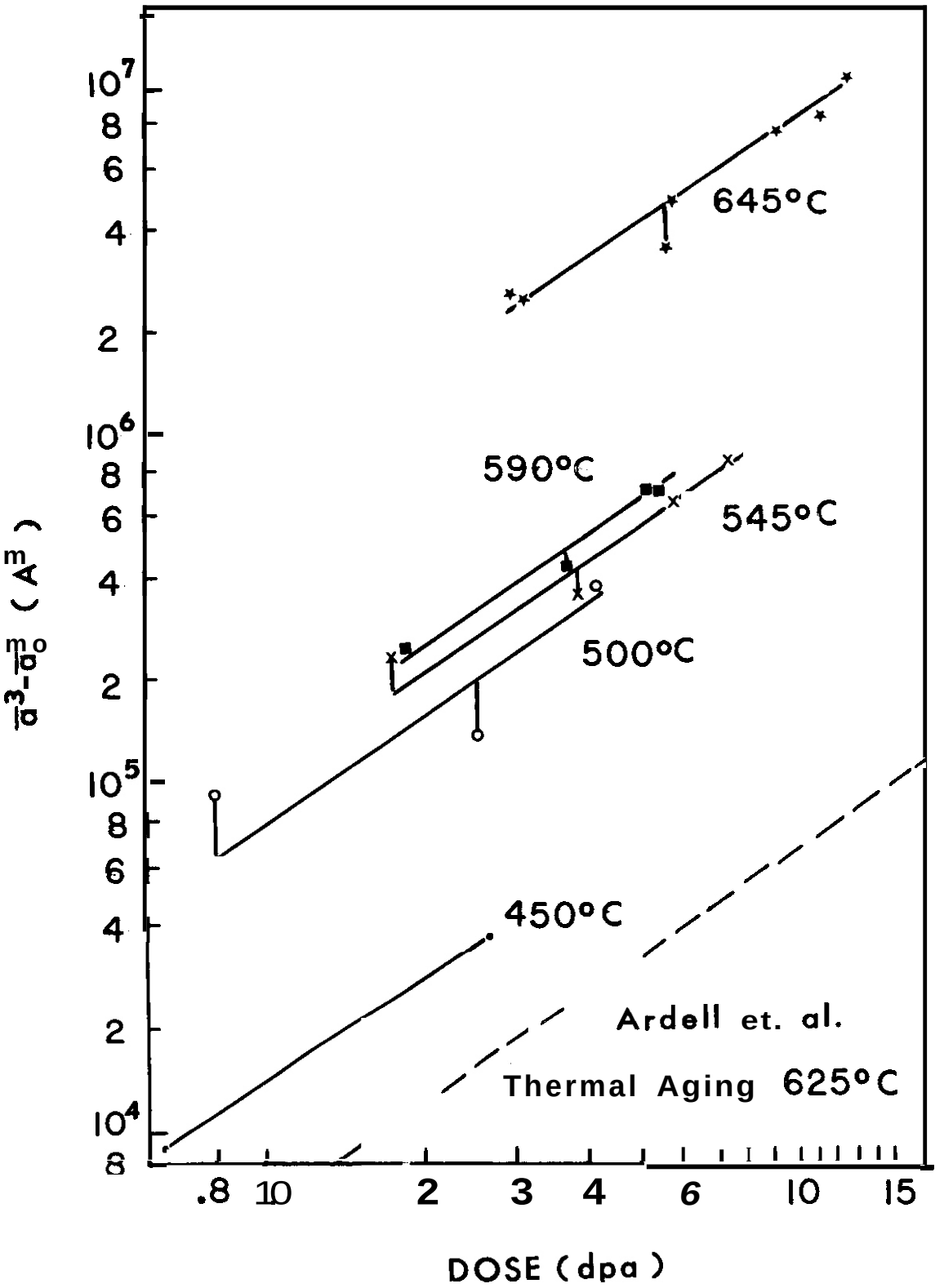

Fig. 6. Average diameter of γ' precipitates raised to the third power in Ni-12.8 at. % Al as function of dose during Ni-ion irradiation at the temperatures indicated. The dose rate was ∿2.7 x 10^{-3} dpa/s or ∿10 dpa/h. For comparison thermal aging data for 625°C is shown as dashed line using a time scale in which 1 h corresponds to ∿10 dpa. [11]

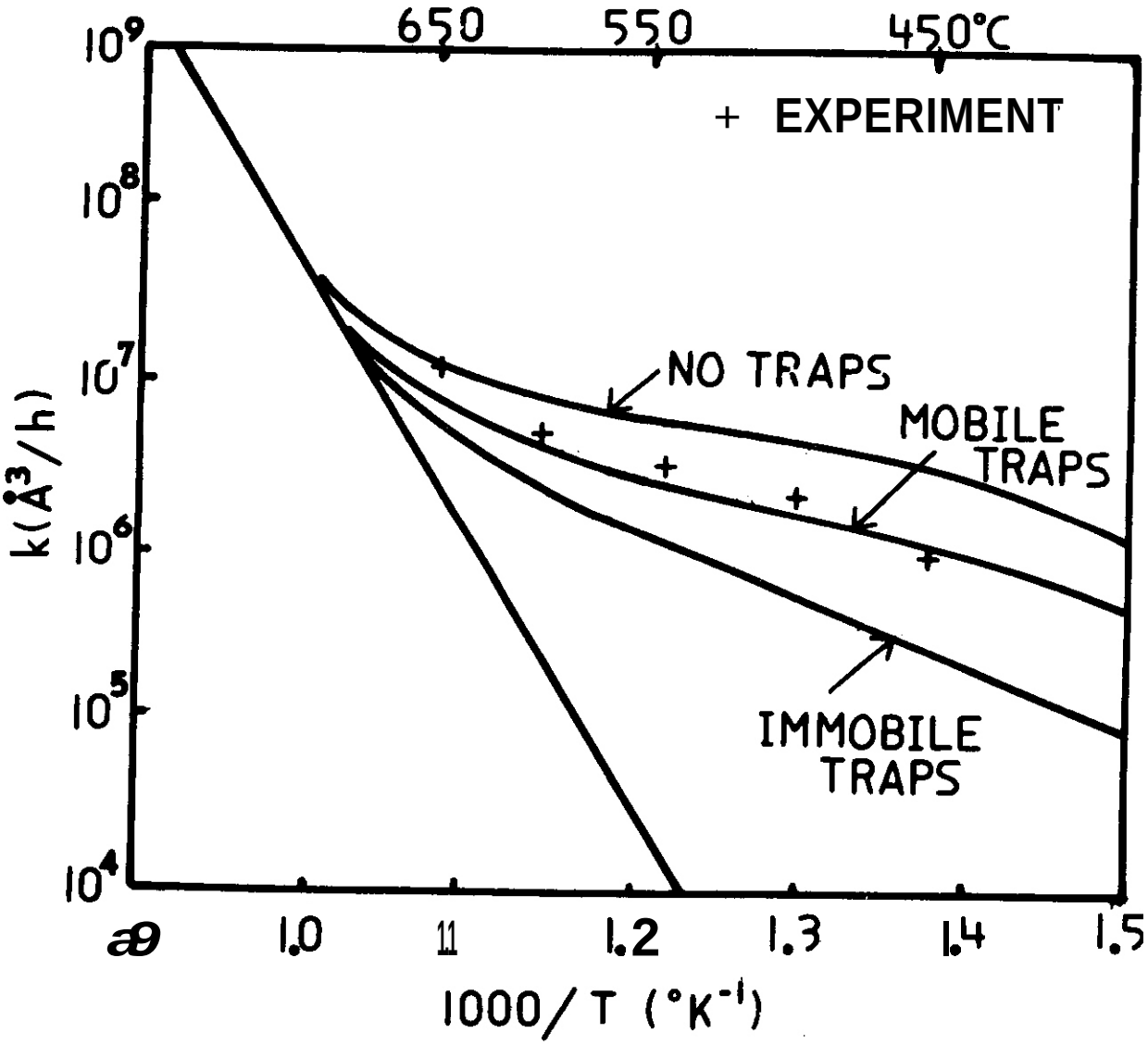

Fig. 7. Coarsening rate constant k as function of inverse temperature for a Ni-12.7 at. % Si alloy during Ni-ion bombardment of a displacement of ∿2.7 10^{-3} dpa/s (+). The curves were calculated from rate theory assuming that interstitials form immoble complexes (immobile traps), mobile complexes (mobile traps) with silicon atoms, or do not become trapped at silicon atoms. [12]

contributions of the excess defects in competing phases can lead to shifts in the phase boundaries. These shifts are expected to be small and no unambiguous experimental evidence for such a shift seems to exist. Some conceptual difficulties for phase boundary shifts resulting from excess defects exist when the interface between the competing phases act as a defect sink.

Displacements tend to disorder a solid and can change a crystalline phase in to an amorphous phase. Such transitions appear especially prevalent in covalently bonded semiconductors but are by no means restricted to this class of materials. Similarly, radiation can disorder an ordered alloy without a severe reduction of the crystallinity. At temperatures at which atomic rearrangements by diffusion, with or without radiation enhancement, occur at perceptable rates, the competition between radiation-induced disorder and reordering by atomic rearrangements may set up a "steady state degree or order" during irradiation. [14] Figure 8 shows some experimental evidence for this phenomenon taken from the work of Potter, [15] At lower temperatures the Ni_3Si film tends towards a lesser degree of order during irradiation. At higher temperatures reordering is fast enough to maintain the degree of order close to that at thermal equilibrium. Since reordering requires only short diffusion distances, phase changes due to radiation-induced disordering are expected to be important mainly at relatively low temperatures.

The third type of radtation-induced phase change, i.e., that caused by segregation, appears to be of the most practical importance and is by far the best documented type. Radiation-induced segregation has been reviewed recently by Okamoto and Rehn. [16] A simple theoretical treatment has been given by Wiedersich et al. [17] As previously mentioned, at intermediate temperatures, significant fractions of the randomly produced defects annihilate at sinks, thus, defect fluxes are induced. A preferential association and/or exchange of specific alloy components with defects couples net fluxes of components to defect fluxes, which in turn alters the local composition near defect sinks. Usually, the matrix near sinks becomes depleted of the large atomic size components and enriched

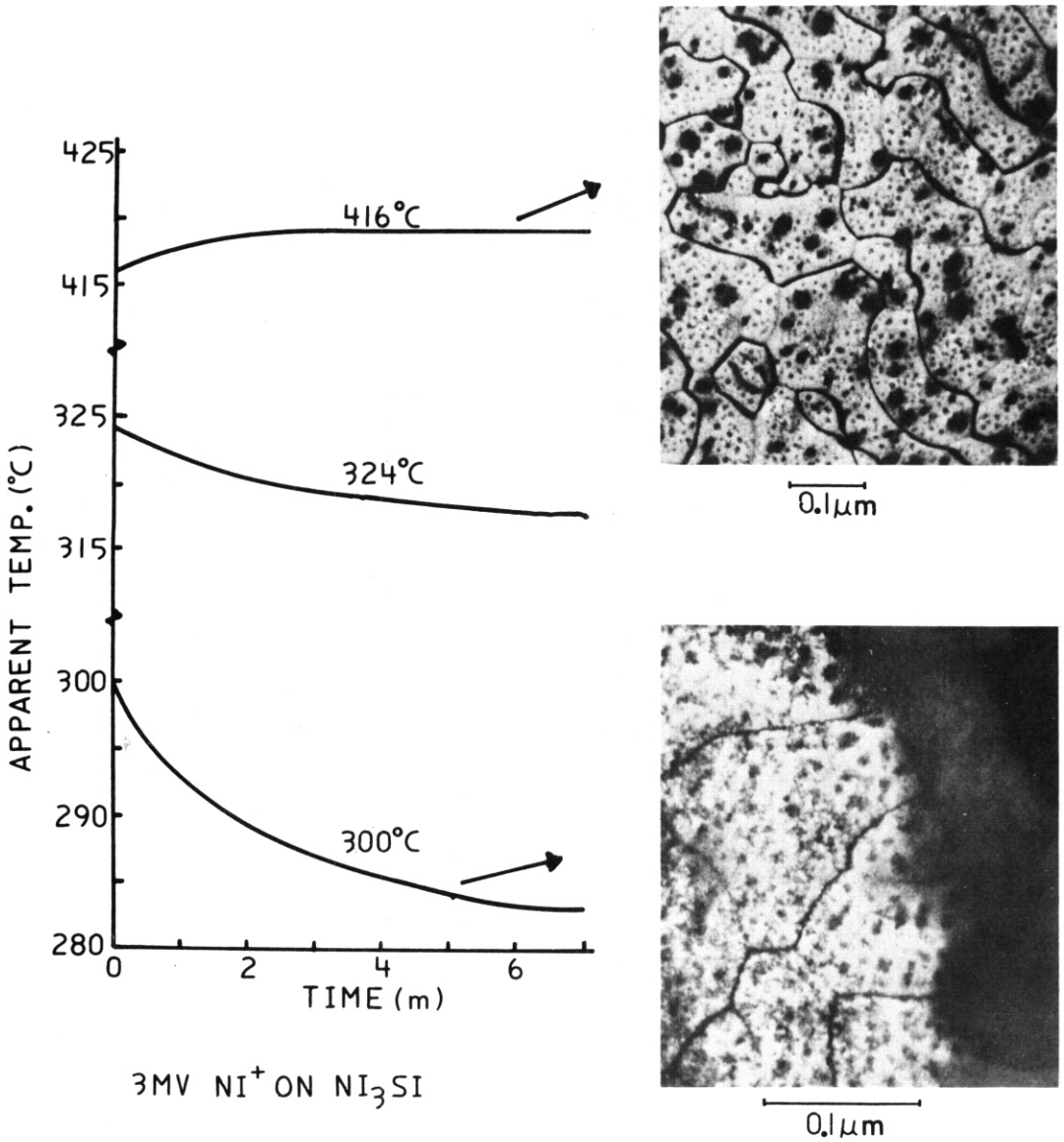

Fig. 8. Apparent temperature of Ni_3Si measured with an infrared pyrometer as function of bombardment time with Ni-ions. The constant actual temperatures are indicated at the curves. The apparent temperature changes are caused by emissivity changes resulting from changes in the degree order. TEM micrographs of the Ni_3Si surface films after bombardment at 416° and 300°C are shown on the right. Courtesy of D. I. Potter.

in the small atomic size compnents of the alloy. [16] Local enrichments of solutes may be sufficiently large to exceed the solubility limit and precipitation can then occur in nominally solid solution alloys. Examples are shown in Fig. 9 for dilute Ni-Si alloys in which Ni_3Si precipitates form on surfaces (a), on dislocation loops (b) and on grain boundaries (c). [18] A normally single phase Ti-6Al-4V alloy forms a high density of 8-phase precipitates during elevated temperature irradiation as shown in Fig. 10. [19] Whether the hcp to bcc phase transformation in this case is in fact caused by local concentration changes has not been established as yet.

Solute depletion near sinks occurs in those alloys in which solvent atoms are preferentially transported with the defect fluxes to sinks. A corresponding enrichment of solute results in the matrix. However, in solid solution alloys the enrichments in the matrix are generally small compared to those discussed in the previous paragraph because the volume around sinks, in which significant concentration changes and gradients occur, is a rather small fraction of the total volume of the material. Hence, generally no precipitation will occur for solid solution alloys which show solute depletion at sinks, except when the average composition is close to the solubility limit.

The solute depletion case is, however, important for redistribution of phases in multiphase alloys as will be shown by examples from the work of Potter and co-workers on a *Ni-12.8* at. % Al alloy. [20] In contrast to the uniform distribution of γ' precipitates which is observed in the thermally aged alloy, precipitate free zones develop during irradition around defect sinks such as dislocation loops as illustrated in Fig. 11. Nickel enrichment around sinks brings the local composition into the solid solution range; γ' precipitates dissolve near these sinks and are concentrated in sink-free regions. As dislocations penetrate at high doses into regions with large and dense precipitates, precipitates partially dissolve at the dislocations as shown in Fig. 12. Fragmentation of precipitates occurs and renucleation takes place in previously precipitate free zones. The number density of precipitates eventually increases at high doses, so that the average precipitate size goes through a maximum

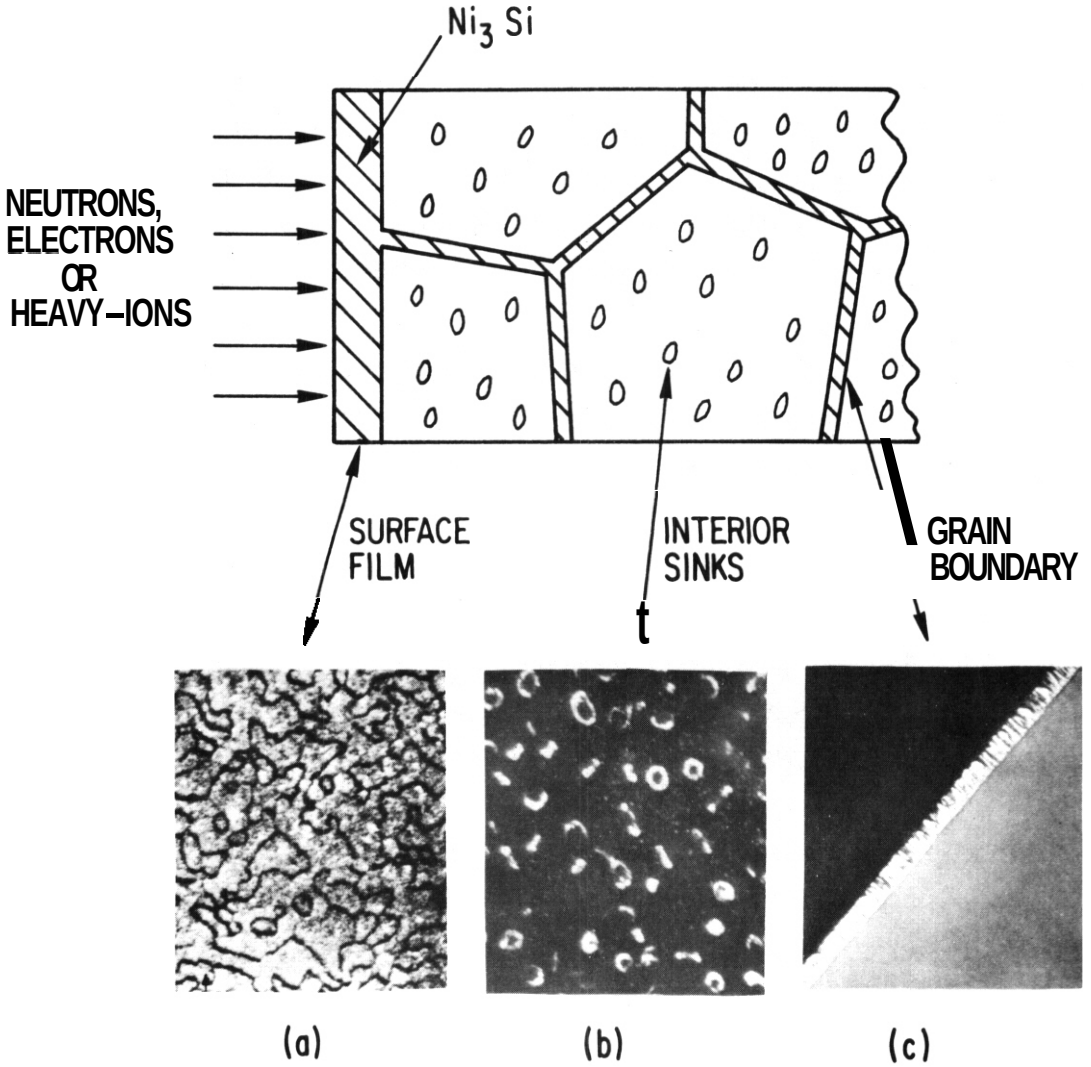

Fig. 9. Precipitation of Ni_3Si on defect sinks in solid **solution** Ni-Si alloys during irradiation (a) shows the domain structure of the continuous surface film of Ni_3Si film; (b) shows toroidal Ni_3Si precipitates that form on interstitial dislocation loops; (c) shows a Ni_3Si film that covers a grain boundary. Courtesy of P. R. Okamoto and K.-H. Robrock.

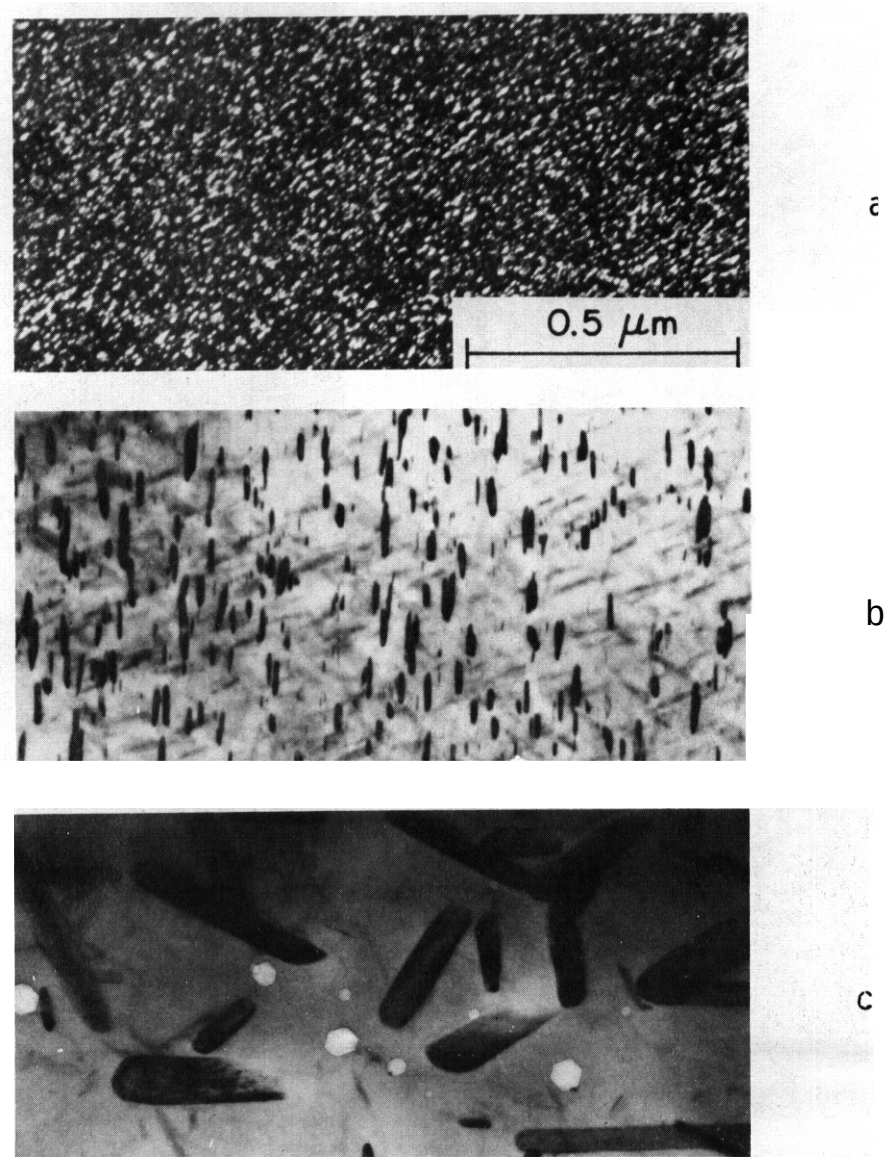

Fig. 10. Formation of b.c.c. precipitates in a h.c.p. commercial purity Ti-6 wt. % Al-4 wt. % V solution annealed alloy during V-ion bombardment; (b) 465°C, 25 dpa, (b) 547°C, 12 dpa, (c) 660°C, 25 dpa. Control specimens with the same temperature history, but shielded from the ion beam, remained single phase. [19]

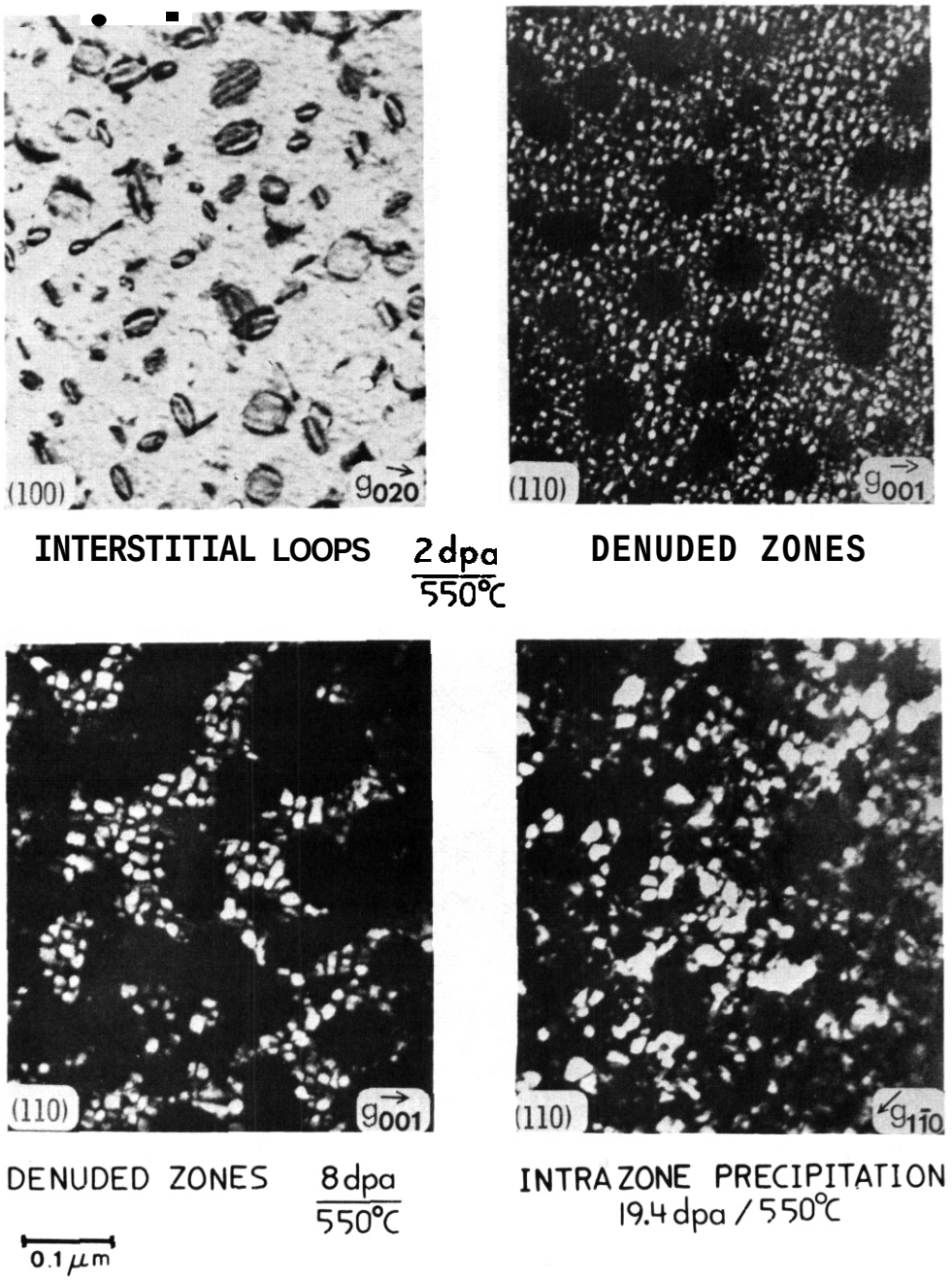

Fig. 11. Development of the precipitate microstructure during irradiation of a Ni-12.8 at. % Al two-phase alloy. Top: Precipitate free zones form around interstitial loops. Bottom left: The zones grow and precipitates become highly concentrated between zones. Bottom right: At high doses dislocation-precipitate interaction partially dissolve existing precipitates and renucleation in zones occurs. [21]

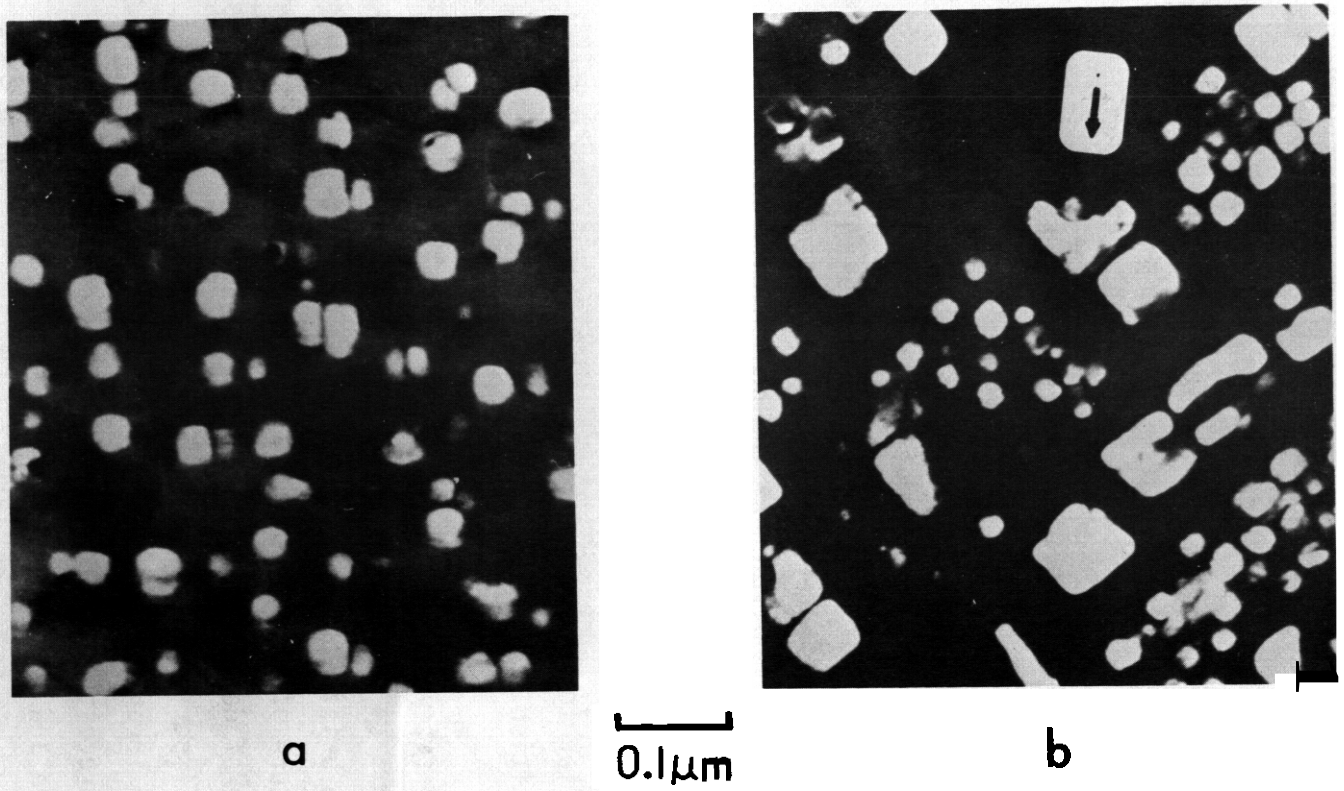

Fig. 12. Dislocation-precipitate interaction as illustrated by dissolution of particles present prior to irradiation. (a) Dislocation loops nucleate almost exclusively at γ/γ' interface in a sample aged 6 h at 715°C, then irradiated to 0.1 dpa at 550°C. (b) Growth of dislocation loops at locations such as that marked with an arrow is accompanied by localized dissolution of the particle, in a sample aged 38 h at 715°C, then irradiated to 5 dpa at 650°C. [12]

as a function of dose during irradiation, Fig. 13, in contrast to the monotomic increase in size during themral aging. [21]

Precipitate redistribution due to radiation-induced segregation also occurs, of course, in two-phase alloys in which solute enrichment at sinks prevails. Precipitates nucleate and grow preferentially at defect sinks, as discussed in conjunction with Fig. 9 for solid solutions. The matrix loses solute and eventually all precipitates not associated with defect sinks are dissolved.

In two component alloys the composition of the precipitate phase should be close to that of the thermal equilibrium phase aside from possible concentration gradients within the precipitates due to defect fluxes. In multicomponent systems, the different strengths of coupling between the various components and the defect fluxes can lead to precipitate compositions that differ markedly from their thermal equilibrium composition in the alloy, because the matrix composition at the precipitate interface may be altered significantly from the average matrix composition. An example of this phenomenon may be the so called G-phase that is found after neutron irradiation in silicon-containing Fe-Cr-Ni based alloys. [22] The G-phase is structurally similar to $M_{23}C_6$, but has a significantly different lattice parameter and composition.

VI. PROBLEM AREAS IN QUANTITATIVE CHARACTERIZATION OF DEFECT CLUSTERS AND MICROSTRUCTURAL FEATURES

As is apparent from the brief discussions of the primary and the secondary damage microstructure presented in the two introductory papers to the Workshop, a multitude of defects, defect clusters and other microstructural features play an important role in the development of the damage structure in materials under irradiation. Although a good qualitative understanding of the major processes and features has been achieved during the past decade, quantitative and predictive descriptions of the response of a material during elevated temperature irradiations require a substantial increase of our knowledge about properties and structures of defect clusters. Some of the most important areas in which the techniques discussed in the Workshop could contribute are outlined here.

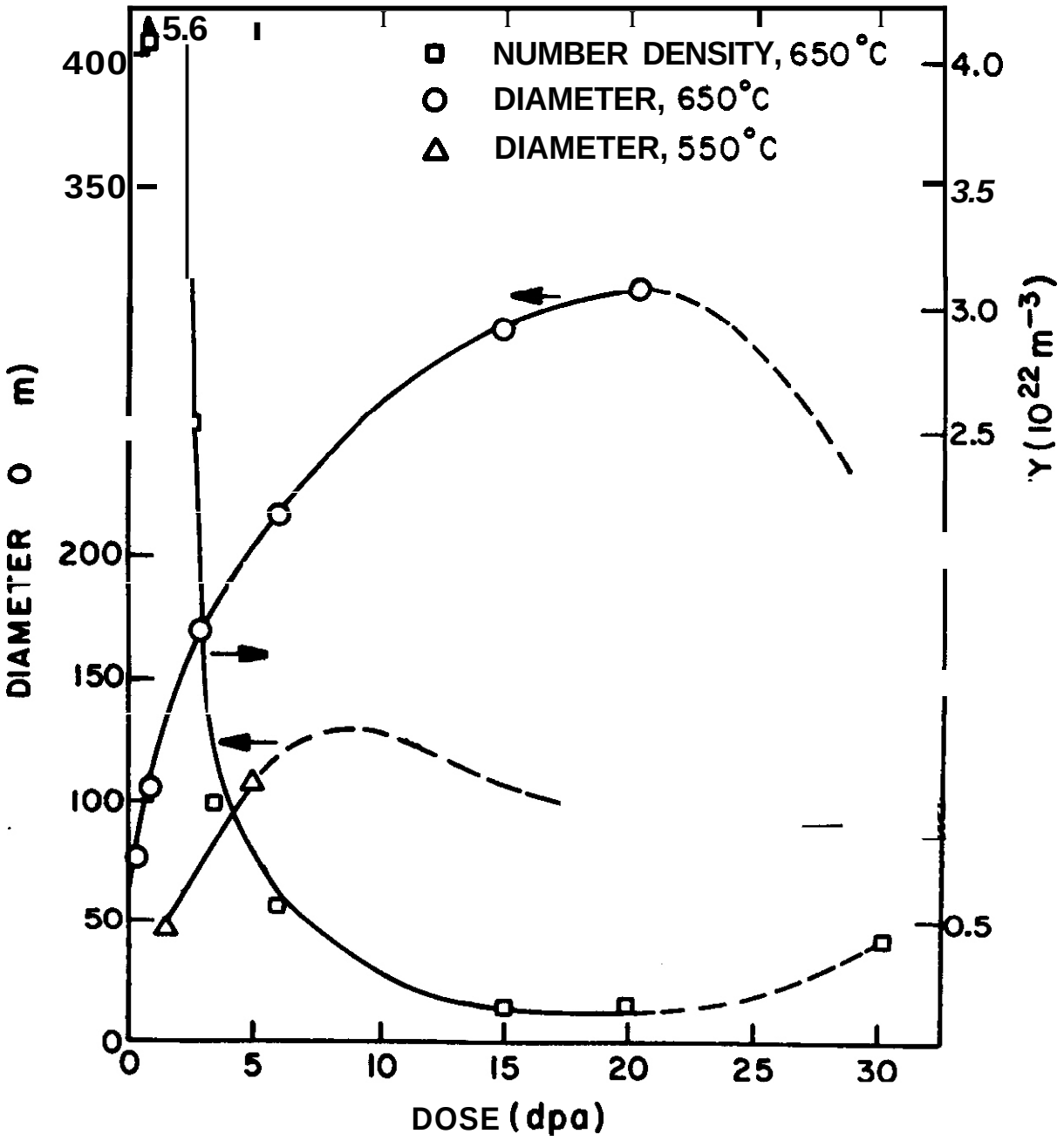

Fig. 13. Precipitate diameter and number density as function of dose in a Ni-12.8 at. Al alloy irradiated at the temperatures indicated. [21]

The structures, binding energies and kinetic properties of defect-solute complexes are of great importance to the quantitative understanding of alloying effects on nucleation of interstitial and vacancy aggregates as well as to the quantitative description of radiation-induced segregation processes. Quantitative information on structures, size-distributions, compositions and stabilities of vacancy, interstitial and solute aggregates, especially those whose size is below the resolution limit of conventional transmission electron microscopy, would provide valuable checks on existing theory and would give guidance for necessary improvements. Measurements of chemical composition and phase identification of precipitates in irradiated materials are prerequisites for a thorough description of phase stability during irradiation. At present most quantitative microstructural investigations rely on quantitative transmission electron microscopy which is highly labor-intensive. Characterization of size-distributions of voids, loops and precipitates and measurements of dislocation densities by less laborious methods would be highly desirable.

Irradiation microstructures are frequently nonuniform. For example, void and dislocation loop depleted regions occur near surfaces and grain boundaries; massive precipitation can be associated with defect sinks and precipitates may form continuous grain-boundary and surface films; frequently, preferential associations between different microstructural features are observed, e.g., voids attached to precipitates. It is easily surmized that such nonuniformities could affect, for example, crack propagation or the relative contribution of grain boundary sliding and intragranular slip to overall deformation. At present, no valid concepts seem to exist for useful, quantitative descriptions of these nonuniformities, nor are reliable models available for relating them to properly changes.

ACKNOWLEDGEMENT

The author expresses his appreciation for many fruitful discussions on the subjects overed in this paper with his collegues at Argonne National Laboratory as well as for their generous contributions of illustrative figures, part of which are unpublished.

REFERENCES

Note: The references given here are intentionally kept to a minimum and an attempt was made to give only rather recent publications where possible.

1. Proc. Intl. Conf. on Radiation Effects in Breeder Reactor Structural Materials, eds. M. L. Bleiberg and J. W. Bennet, AIME, New York, 1977.

2. Proc. First Topical Meeting on Fusion Reactor Materials, eds. F. W. Wiffen, J. H. DeVan and J. O. Stiegler, to be published in J. Nucl. Mater.

3. Workshop on Solute Segregation and Phase Stability During Irradiation, November 1-3, 1978, Gatlinburg, TN, to be published in J. Nucl. Mater.

4. H. Wiedersich in Radiation Damage in Metals, eds. N. L. Peterson and S. D. Harkness, ASM, Metals Park, OH, 1976, p. 157.

5. A. D. Brailsford and R. Bullough, J. Nucl. Mater. 69 & 70, (1978) 434.

6. L. K. Mansur. Proc. Workshop on Correlation of Neutron and Charged Particle Damage, CONF-760673, 1976, p. 61.

7. D. I. Potter, private communication.

8. J. J. Laidler, F. A. Garner and L. E. Thomas in Radiation Damage in Metals, eds. N. L. Peterson and S. D. Harkness, ASM, Metals Park, OH, 1976, p. 194.

9. R. A. Erck, D. I. Potter and H. Wiedersich, J. Nucl. Mat., in press.

10. B. A. Loomis, A. Taylor and S. B. Gerber, in Fundamental Aspects of Radiation Damage in Metals, eds. M. T. Robinson and F. W. Young, Jr., CONF-751006-P2, 1975, P-T245.

11. D. I. Potter and A. W. McCormick, Acta Meta., in press.

12. D. I. Potter and H. Wiedersich, in Ref. [3].

13. S. I. Maydet and K. C. Russel, J. Nucl. Mater. 64 (1977) 101.

14. P. Wilkes in Ref. [3], K-Y. Liou and P. Wilkes, submitted to J. Nucl. Mat.

15. D. I. Potter, private communication.

16. P. R. Okarnoto and L. E. Rehn, in Ref. [3].

17. H. Wiedersich, P. R. Okamoto and N. Q. Lam, in Ref. [3].

18. P. R. Okamoto and K.-H. Robrock, private communication.

19. S. C. Agarwal, G. Ayrault, D. I. Potter, A. Taylor and F. V. Nolfi, Jr. in Ref. [2].

20. D. I. Potter and H. A. Hoff, Acta Meta. 24 (1976) 1155.

21. D. I. Potter and D. G. Ryding, J. Nucl. Mater. 71 (1977) 14.

22. L. E. Thomas, in Ref. [3].

RADIATION DAMAGE ANALYSIS BY POSITRON ANNIHILATION SPECTROSCOPY*

R. W. Siegel
Materials Science Division
Argonne National Laboratory
Argonne, IL 60439

I. INTRODUCTION

Positron annihilation spectroscopy (PAS) has in recent years become a valuable new tool for investigating defects in metals. The ability of the positron to localize in a trapped state at various defect sites, in which the positron annihilates with unique characteristics. has enabled the positron to be used as a localized probe of these defect sites. Several reviews of the application of PAS to the study of defects in metals have been published [1-8], as have more general treatises on the applications of positron annihilation to the study of solids [9,10]. PAS has made, and has considerably greater potential for, a significant contribution to radiation damage analysis in two areas of importance: (1) the determination of atomic-defect properties, a knowledge of which is necessary for the modeling required to couple the results of model experiments using electron and ion irradiation with the expected irradiation conditions of reactor systems, and (2) the monitoring and characterization of irradiation-induced microstructure development. A unique aspect of PAS for radiation damage analysis is the defect specificity of the annihilation characteristics of a trapped positron. In addition to its value as an independent analytical tool, PAS can be a useful complement to more traditional techniques for defect studies.

II. POSITRON ANNIHILATION

The physical basis for PAS can be described with the aid of fig. 1. When a positron (e^+) is injected into a metal, usually from a radioactive source such as ^{22}Na, it becomes rapidly ($\sim$1 ps) thermalized resulting in a positron initially in a Bloch state (see fig. 2) in the lattice, but which can subsequently be trapped in a highly localized state in a defect (e.g., see fig. 3). At a time δt (distributed from zero up to some hundreds of

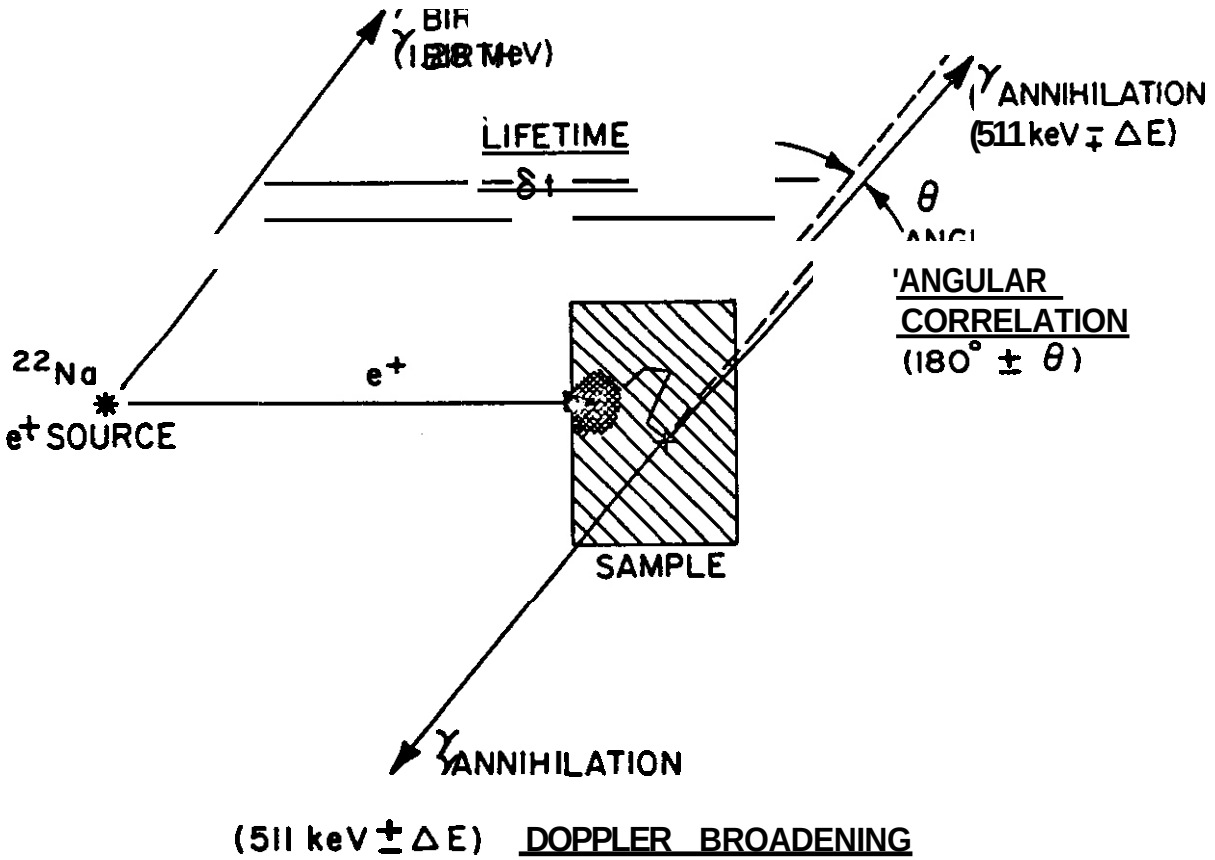

Fig. 1. Positron annihilation spectroscopy. Schematic representation of positron annihilation indicating the bases for three experimental techniques: lifetime, angular correlation, and Doppler broadening (Ref. 6).

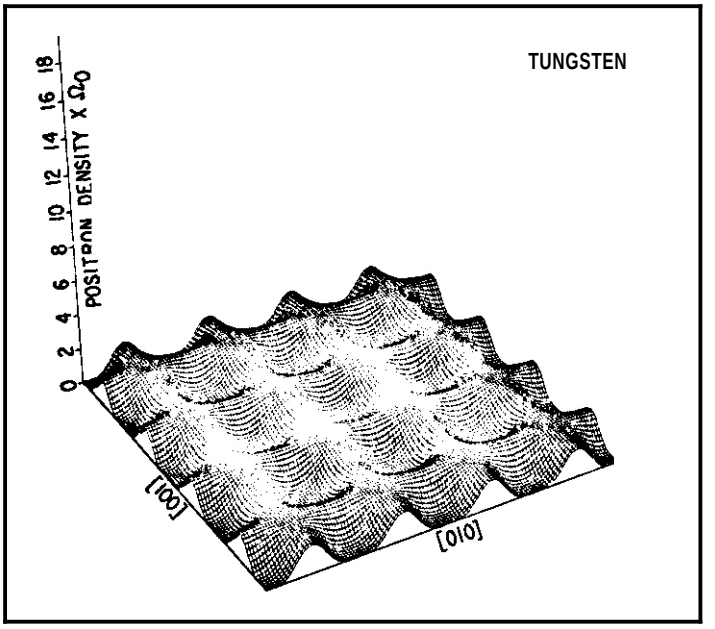

Fig. 2. Positron density x Ω_0 in W in the Bloch state of the positron, shown on a network of 25 atomic sites in the (001) plane containing no vacancies; a_0 is the volume of the primative unit cell in which the calculated positron density is normalized (Ref. 11).

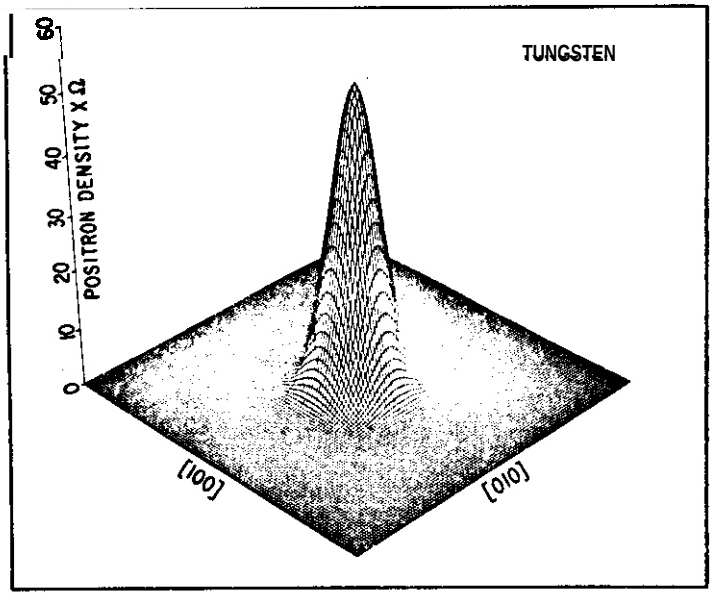

Fig. 3. Positron density x Ω in W in the vacancy-trapped state of the positron, shown on a network of 25 atomic sites in the (001) plane with the vacancy at the center; Ω is the volume of the supercell (Ref. 11) in which the calculated positron density is normalized (Ref. 11).

ps) after positron injection into the metal, signaled in the case of a ^{22}Na positron source by the essentially simultaneous emission of a 1.23 MeV "birth" γ-ray, the positron will annihilate with an electron yielding, almost always, two y-rays.

Although the positron lifetimes and source intensities are such that no more than one positron usually exists in the metal sample at a given instant, the PAS measurement techniques integrate over a large number (often $\sim 10^6$) of annihilation events. The distribution of the measured δt values for a number of these events yields information regarding the total electron density $\rho^-(\vec{r})$ in the region of positron-electron annihilation, since the rate of positron annihilation, λ, equal to the reciprocal of the positron lifetime, is given by the overlap integral of the electron and positron densities as

$$\lambda = \pi r_0^2 c \int \rho^-(\vec{r})\rho^+(\vec{r})\, d^3r \quad , \tag{1}$$

where r_0 is the classical electron radius, c is the velocity of light and $\rho^+(\vec{r})$ is the positron density in the crystal. A typical set of experimental positron lifetime spectra are shown in fig. 4 for pure a-Fe with and without defects (from Ref. [12]). It can be seen from fig. 4 that the presence of defects in the a-Fe increases the observed positron lifetimes, a result of the positron being trapped and subsequently annihilating in a region of lower-than-average electron density, the defect (e.g., vacancy, dislocation, void).

Owing to the necessity of energy and momentum conservation in the annihilation process, the two γ-rays resulting from the electron-positron pair annihilation each have an energy equal to the rest-mass energy of an electron or positron (m_0c^2 = 511 keV) plus or minus an energy increment ΔE and propagate in opposite directions plus or minus an angular deviation θ (see fig. 1). The deviations ΔE and θ arise from the net momentum of the annihilating positron-electron pair. However, since the positrons have only thermal energies ($\sim kT$) just prior to annihilation, the values of ΔE and e correspond to essentially only the momenta of the annhilating crystal electrons, either valence or core, with the higher-momentum core electrons contributing pro-

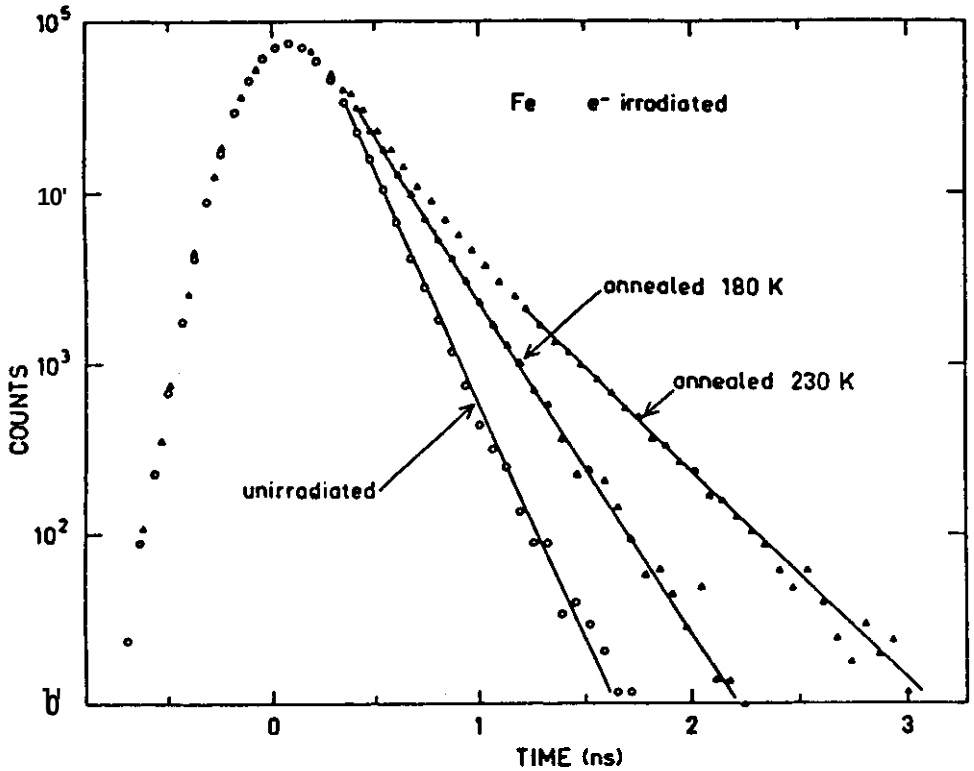

Fig. 4. Positron-lifetime spectra after source-background subtractions in electron-irradiated high-purity α-Fe at various stages of isochronal annealing (high-dose case, see Fig. 9 and text) (Ref. 12).

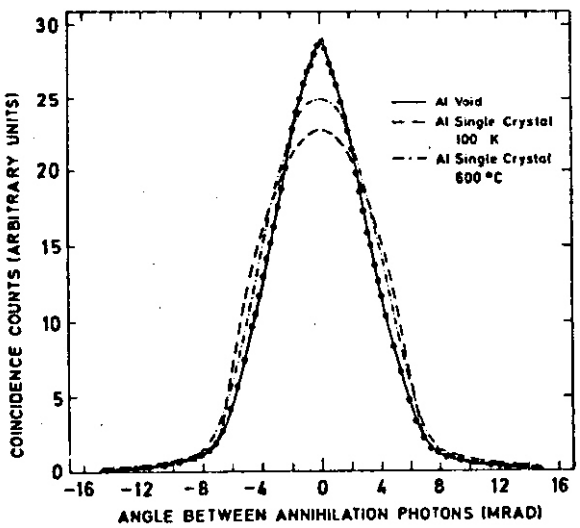

Fig. 5. Angular-correlation curves from Al at 100K, 600°C, and containing voids (Ref. 5).

portionately more to the largest values of ΔE and d. This can be seen in fig. 5 in which typical angular-correlation curves, $N(\theta)$ versus θ, are shown'for Al at 100K containing no vacancies, Al at 600K containing $\sim 10^{-5}$ vacancies, and Al containing voids (from Ref. [5]). Since fewer core electrons are present at the defect site at which the positron is trapped, and from which it subsequently annihilates, the angular-correlation curves are seen to be more sharply peaked for the Al containing vacancies or voids. A similar effect on the Doppler-broadening spectra, $P(\Delta E)$ versus AE, also results from the presence of defect traps for the positron.

The similarity of information available from Doppler-broadening and angular-correlation experiments (of the one-dimensional or long-slit type) can be most easily seen by comparing the expressions for $N(\theta)$ and $P(\Delta E)$ in terms of the independent-particle model probability, $R(\vec{p})$, that positron-electron annihilation yields 2γ-emission with total momentum ;

$$R(\vec{p}) = \pi r_o^2 c \sum_k n_k \left| \int d^3r\, e^{-i\vec{p}\cdot\vec{r}} \psi_+(\vec{r})\psi_-(\vec{r}) \right|^2 , \tag{2}$$

where $\psi_+(\vec{r})$ and $\psi_k(\vec{r})$ are the positron and electron wavefunctions, respectively, n_k is the Fermi function, and k represents both the electron wavevector $\vec{k}$ and the band index. The expressions for $N(\theta)$ and $P(\Delta E)$ are then

$$N(\theta_z) = \iint dp_x dp_y\, R(\vec{p}) \tag{3}$$

and

$$P(\Delta E_x) = \iint dp_y dp_z\, R(\vec{p}) , \tag{4}$$

where the direction of the emitted y-rays has been taken as x in a Cartesian coordinate system, and the momenta, angles and energies are related by $p_j = mc\theta_j$ and $\Delta E_j = cp_j$, where m is the electron mass. Indeed the positron lifetime, $\tau \equiv \lambda^{-1}$, gives even more-integral information regarding the region from which it annihilates, as can be seen from its expression in terms of $R(\vec{p})$ as:

$$\tau^{-1} \equiv \lambda = (2\pi)^{-3} \int d^3p \; R(\vec{p}) \quad , \tag{5}$$

which is equivalent to eq. (1). However, since the average electron density at a defect site can be quite defect specific, positron lifetime measurements have offered a unique method for investigating, for example, vacancy-clustering processes at the smallest cluster sizes. The momentum measurements (angular correlation or Doppler broadening) can also yield detailed defect-specific information, as indicated by eqs. (3) and (4), but few attempts to date have been made to apply this information to defect studies. A further advance in this area should come from the advent of two-dimensional angular-correlation studies on metals containing defects [13], since the annihilation spectrum obtained from such experiments,

$$N(\theta_z,\theta_y) = \int dp_x \; R(\vec{p}) \quad , \tag{6}$$

yields the least-integral, and hence most detailed, information regarding the region from which the positron annihilates.

III. TRAPPING MODEL

The results of PAS experiments on metals containing defects are normally analyzed in terms of the two-state trapping model [14-16]. In this model it is assumed that the positron: (1) exists in either one of only two states in the metal, the bulk or Bloch state (see fig. 2) and the defect-trapped state (e.g., see fig. 3), in relative concentrations $n_b(t)$ and $n_t(t)$, respectively; (2) enters the system at time t=O only through the Bloch state; and (3) is thermalized at t=0. This model can thus be described by the set of coupled differential equations:

$$\frac{dn_b}{dt} = -n_b\lambda_b - n_b\kappa_t \tag{7a}$$

$$\frac{dn_t}{dt} = +n_b\kappa_t - n_t\lambda_t \quad , \tag{7b}$$

where λ_b and λ_t are the positron-annihilation rates in the Bloch (lattice) and defect-trapped states, respectively, and κ_t is the total transition or trapping rate of the positron from the Bloch state to its defect-trapped state. The positron lifetimes in the Bloch and defect-trapped states are defined by $\tau_b \equiv \lambda_b^{-1}$ and $\tau_t \equiv \lambda_t^{-1}$, respectively.

Equations (7a and b) are readily solved to yield an expression for the fraction $N(t)$ of positrons present in the system at time t*

$$N(t) = n_b(t) + n_t(t)$$

$$= (1-I_2)\exp(-\Lambda_1 t) + I_2 \exp(-\Lambda_2 t) \quad , \tag{8}$$

where Λ_1, Λ_2, and I_2 are the decay rates and intensity that can be obtained from a deconvolution analysis of an observed positron lifetime spectrum. An experimentally observed lifetime spectrum for such a system is the time derivative of eq. (8) convoluted with the resolution function of the experimental lifetime apparatus plus any additional contribution from the positron source itself (see fig. 4). The experimentally obtainable parameters Λ_1, Λ_2, and I_2 are related to the physical quantities λ_b, λ_t, and κ_t by:

$$\lambda_b = (1-I_2)\Lambda_1 + I_2\Lambda_2 = \Lambda_1 - \kappa_t \tag{9a}$$

$$\lambda_t = \Lambda_2 \tag{9b}$$

$$\kappa_t = I_2 (\Lambda_1 - \Lambda_2). \tag{9c}$$

---

*Use is made here of the ergodic hypothesis, which draws the equivalence between a set of sequential individual events (e.g., positron-electron pair annihilations in a metal) and the time average or sum of these events (e.g., an experimentally collected lifetime or momentum spectrum).

It can be seen from eqs. (8) and (9) that $\Lambda_2 \equiv \tau_2^{-1}$ is the decay rate corresponding to the position in its defect-trapped state and may thus be used in determining the nature of the defect trap present in the metal. The intensity I_2, on the other hand, is directly related to the probability of position trapping at the defect and is thus a measure of the defect-trap concentration.

The mean positron lifetime, τ, is given by

$$\tau = \int_0^\infty N(t)\, dt = \tau_b \left(\frac{1+\tau_t\kappa_t}{1+\tau_b\kappa_t}\right) \tag{10a}$$

$$= (1-A_t)\,\tau_b + A_t\tau_t \quad , \tag{10b}$$

where

$$A_t = \int_0^\infty \lambda_t n_t(t)dt = \frac{\kappa_t}{\lambda_b + \kappa_t} \tag{11}$$

is the probability that the positron annihilates from the defect-trapped state. An expression analagous to eq. (10b) can be written for any of the characteristic shape-parameters, which we denote generically by F, obtained from analyses of the angular-correlation or Doppler-broadening spectra. Thus,

$$F = (1-A_t)F_b + A_tF_t \quad , \tag{12}$$

where A_t is given by eq. (11) and F_b and F_t are the spectrum shape-parameters characteristic of positron annihilations from the Bloch and defect-trapped states, respectively. For any of these momentum (or energy-shift) distribution shape-parameters, F, or the mean positron lifetime, τ, its relationship to the total positron trapping rate, κ_t, is given by

$$\kappa_t = \lambda_b(P-P_b)/(P_t-P) \quad , \tag{13}$$

where P can represent any F or τ.

The trapping rate κ_t, within the trapping model [see eqs. (9c) and (13)]

is proportional to the concentration of defect traps. For a single defect type it is simply $\kappa_t = \mu_t c_t$, where μ_t is the (specific) positron trapping rate per unit defect concentration and c_t is the defect-trap concentration. For an ensemble of various defects (j) that trap positrons, $\kappa_t = \sum_j \mu_j c_j$, where μ_j and c_j are the specific positron trapping rate of the jth type defect and the concentration of this defect, respectively. In such a multi-defect trap situation, the values of τ_t and F_t obtained from two-state trapping-model analyses of PAS experiments are essentially weighted averages of the τ_j's or F_j's for the individual defect types present in the system. Furthermore, in this case κ_t is proportional to the total concentration of defects that act as positron traps, with the proportionality constant being an appropriately weighted average of the specific trapping rates for the defect ensemble.

Thus in summary, the concentration of defects to which the positron is sensitive (e.g., vacancies, vacancy clusters, voids, dislocations) can be monitored directly by experimental PAS determinations of κ_t, or somewhat less directly through I_2 [see eqs. (8) and (9)]. In addition, the nature of the defect being monitored by the positron can be deduced by means of its characteristic positron-annihilation parameters $\tau_t \equiv \tau_2$ or F_t. This combination of available information from PAS regarding both the concentration and nature of the defects to which the positron is sensitive forms the basis for the application of PAS to the study and characterization of defects in metals.

IV. APPLICATIONS OF PAS TO DEFECTS

We now turn to some examples of the application of PAS to defects in metals; applications that have direct bearing on the analysis of radiation damage. It should first be pointed out, however, that the positron is not equally sensitive to all lattice defects in metals, and in a very definite sense this is one of the positive attributes of PAS as applied to defect studies. While the positron is very sensitive to local regions of lower-than-average electron density in metals, such as vacancies, small vacancy clusters, voids or dislocation lines and jogs, it is essentially insensitive to regions of higher-than-average electron density, as found at an interstitial or small

interstitial cluster. Thus, PAS is able to differentiate between the earliest stages of vacancy and interstitial clustering in irradiated systems in a manner not directly possible by resistometric techniques or transmission electron microscopy.

A major application of PAS has been in the study of the physical properties of vacancies. A knowledge of these properties is necessary both for an understanding of radiation-damage development in metals and in order to be able to predict the behavior of complex defect systems in neutron-irradiated metals from the results of model experiments in electron- or ion-irradiated metals. The measurement of vacancy formation enthalpies, H_v^F, in metals by PAS has been recently reviewed [6] and compared with other available techniques. A typical set of experimental PAS Doppler-broadening data [17] for the measurement of H_v^F in Cu is shown in fig. 6, in which a lineshape-parameter F(T), defined by a region around $\Delta E=0$, is plotted as a function of temperature, T. At temperatures below $\sim 500^{\circ}C$ in Cu the positron is insensitive to the rather low equilibrium concentration of vacancies ($c_v \lesssim 10^{-7}$) and, hence, F(T) is simply $F_b(T)$, the lineshape parameter corresponding to the positron annihilating in its Bloch state. The parameter $F_b(T)$ varies linearly with temperature in this temperature region, as indicated by the lower dashed line in fig. 6, a behavior which is theoretically understood [18,19] in terms of lattice expansion and phonon-coupling effects. At the highest temperature, F(T) approaches a saturation, indicated by the upper dashed line, which is representative of the lineshape parameter $F_v(T)$, corresponding to the positron annihilating from its vacancy-trapped state. The parameter $F_v(T)$ is also linearly temperature dependent, although more weakly so than $F_b(T)$, since only lattice-expansion is expected to affect this parameter [11].

The temperature dependence of F(T) in the transition region of the sigmoidal curve shown in fig. 6 between these two states is controlled by the transition or trapping rate $\kappa_V(T) = \mu_V c_V = \mu_V \exp(S_v^F/k) \exp(-H_v^F/kT)$, where the subscript v refers to the vacancy and the other quantities have their usual meanings. Thus, an Arrhenius plot of these data, shown in fig. 7, yields a straight line from which a value of $H_v^F = 1.31 \pm 0.05$ eV has been deduced [17] for Cu. A representative, but limited set of recent PAS results for values of H_v^F in several metals is presented in table 1. It can be

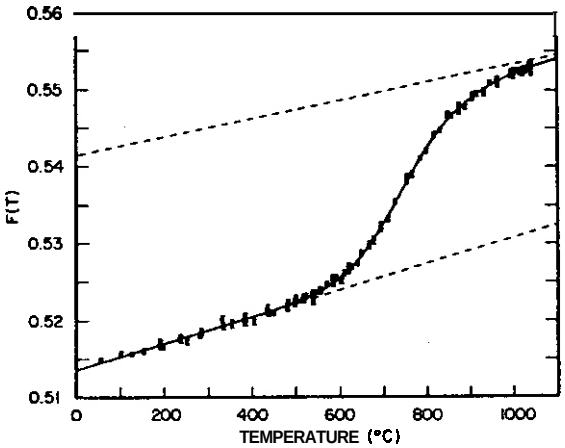

Fig. 6. Doppler-broadening lineshape-parameter F(T) for Cu versus temperature, T, and the two-stage trapping model fit to the data (Ref. 17).

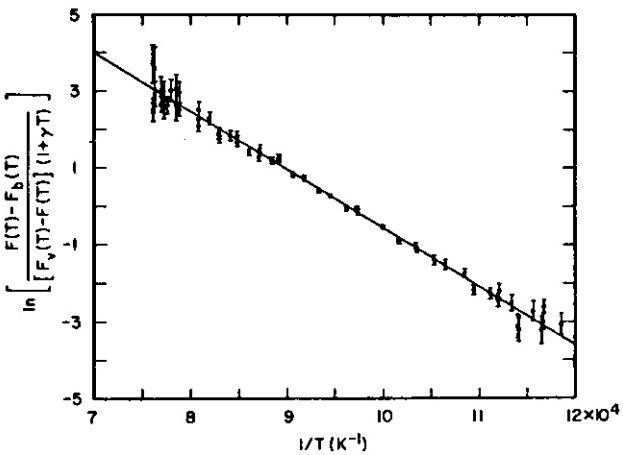

.Fig. 7. Arrhenius plot of the data and fit for Cu shown in Fig. 6 (Ref. 17).

TABLE 1.

Some recently measured values of the vacancy formation enthalpy, H_V^F, for several metals by PAS

Metal	H_V^F(eV)	Reference
Al	0.66±0.02	[20]
Ag	0.16±0.02	[21]
Au	0.97t0.01	[21]
Cu	1.31+0.05	[17]
Ni	1.74±0.06	[22]
V	2.1 t0.2	[23]
Nb	2.6±0.3	[23]
Mo	3.0±0.2	[23]
Ta	2.8±0.6	[23]
W	4.0±0.3	[23]

seen that PAS has been useful in deterining values of H_V^F in a variety of metals, even the bcc refractory metals for which little vacancy-formation information had previously been available. These values for H_V^F when combined with the results from tracer self-diffusion measurements of the activation enthalpy for diffusion also yield values of the vacancy migration enth lpy, often the most reliable source of such information regarding vacancy mobility in metals [6].

In addition to investigations of vacancy formation in pure metals, a number of similar PAS measurements of vacancy formation in dilute alloys have also been carried out. These have yielded information regarding the interaction energies between a vacancy and a solute atom in the systems investigated, since this interaction is responsible for an enhanced vacancy concentration at a given temperature. The results of much of this work, and the basis upon which the experiments have been analyzed, have been reviewed elsewhere [24].

PAS has also been applied quite extensively to post-irradiation annealing behavior in metals, both in attempts to study the mobility of the atomic defects produced by irradiation and to investigate the nature of the vacancy

precipitation process and the resulting defect structures. It is useful to look at a few examples from this class of PAS experiments in order to point out the types of defect information available from PAS and to elucidate the particular advantages of PAS over more traditional techniques for such defect studies.

Some results of a set of Doppler-broadening studies [5, 25, 26] of Cu, irradiated at 10K with 3 MeV electrons to an initial Frenkel-pair concentration of $\sim 3 \times 10^{-4}$, are presented in fig. 8. These studies have been unique to date, in that they have utilized the defect specificity of the electron-momentum information available from PAS in investigating the developing microstructure during post-irradiation annealing. A comparison is made in fig. 8(a) between the isochronal-annealing behavior of two Doppler-broadening shape parameters, I_v and I_c defined in fig. 8(c), and that of the more traditional electrical resistivity. While the resistivity measurements can only indicate the loss of electron-scattering centers (vacancies or interstitials or both) during stage-I11 (at ~250K) annealing, the PAS-parameter measurements, which are primarily sensitive to vacancy-like defects, rather clearly indicate the loss of vacancies via precipitation into void-like precipitates. This can be seen more clearly in fig. 8(b), in which a parameter designed to be defect-type specific, but defect-concentration independent, is plotted for the irradiated Cu and compared with a similar plot for quenched Au and parameter calibrations for dislocation loops, vacancies, and liquid-state trapping sites in Cu. It should be possible in the future to define parameters of the PAS momentum distributions that are even more defect specific than that shown in fig. 8(c) when our understanding of the positron-annihilation spectra for various defects becomes sufficient for this purpose. At that time, PAS Doppler-broadening and angular-correlation studies will become even more powerful tools than they are at present for the study of defects in irradiated metals.

Positron lifetime measurements on metals containing previously undefined defect ensembles have the distinct advantage at the present time that the positron lifetime in a particular defect-trapped state is a more well-defined physical quantity than the various momentum-distribution shape-parameters in use, and can alsa be theoretically estimated with reasonable, if not precise, certainty. Thus, the positron lifetimes in vacancies and voids are

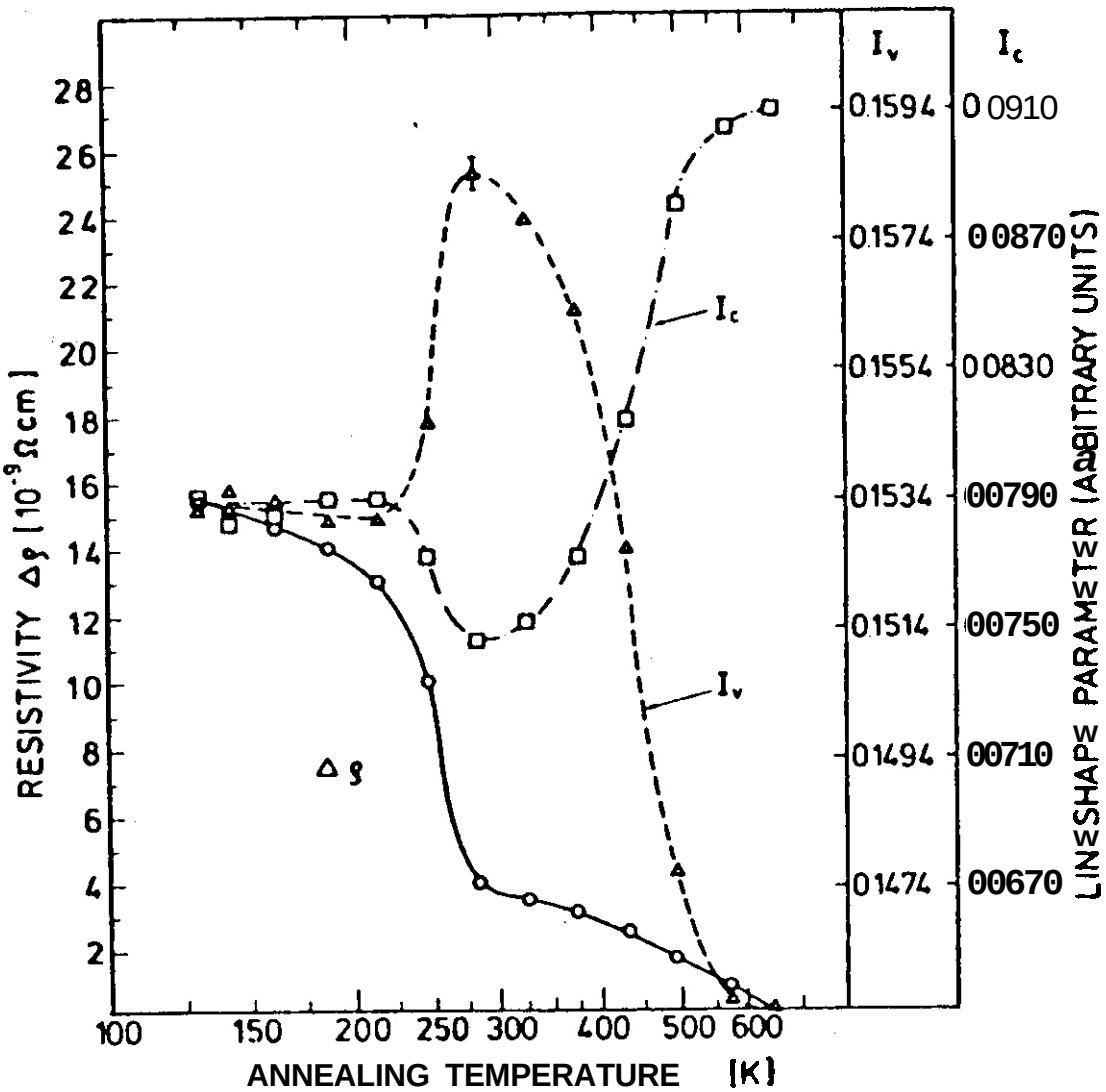

Fig. 8A Doppler-broadening study of electron-irradiated Cu: (a) Isochronal annealing of the lineshape-parameters I and I_V and I_t defined in (c) and the electrical-resistivity increment $\Delta\rho$.

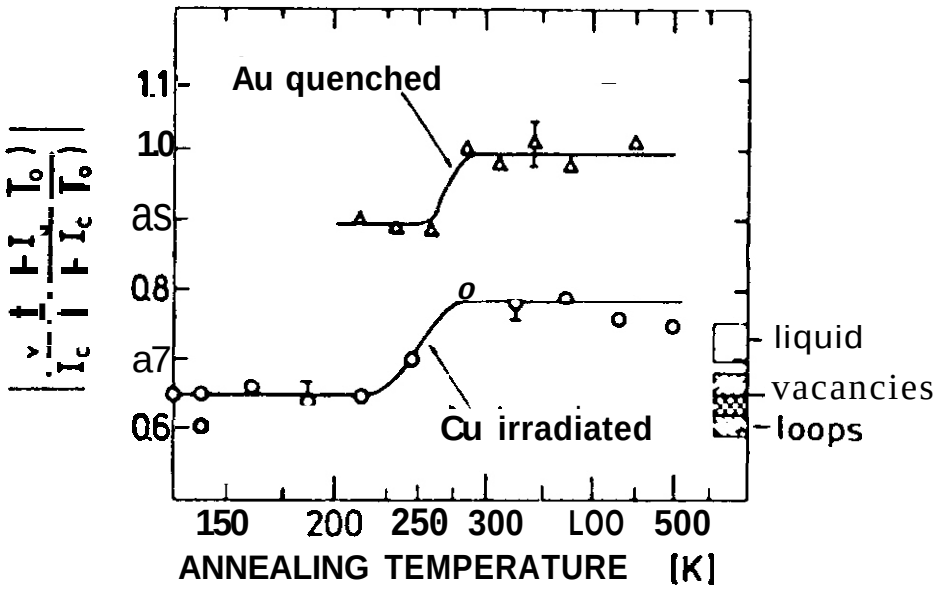

Fig. 8B The ratio of lineshape-parameter differences for electron-irradiated Cu versus annealing temperature is compared with that for quenched Au and calibrated values in Cu for vacancies, dislocation loops, and the liquid.

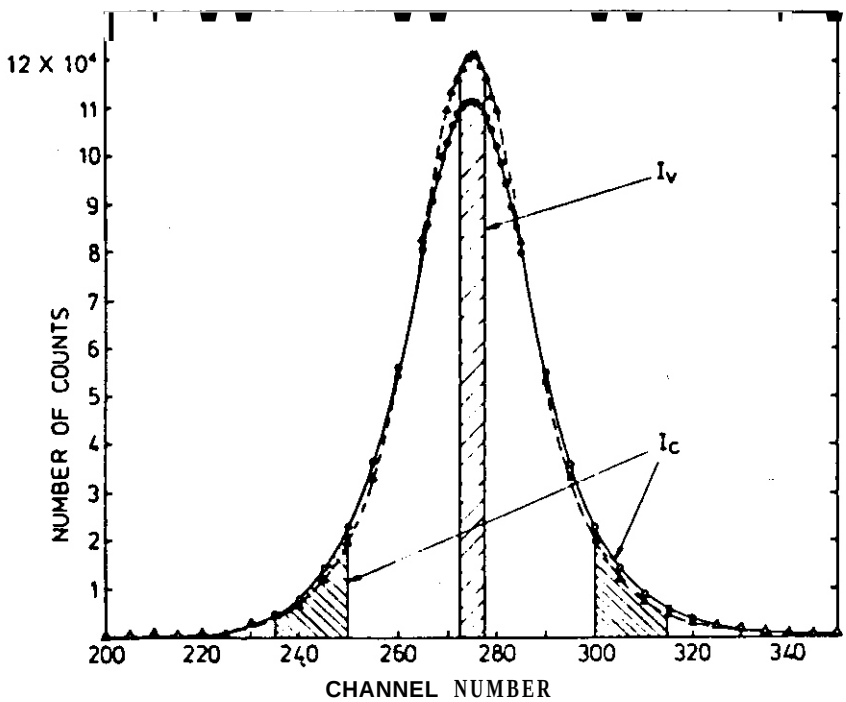

Fig. 8C. The lineshape-parameters I_v and I_c are indicated on Doppler-broadened annihilation lines (spectra) for annealed (circles) and electron-irradiated (triangles) Cu (Refs. 5, 25, 26).

rather well-established quantities and can be used in evaluating the results of lifetime experiments on irradiated metals. An example of such results [12] is presented in fig. 9, in which the isochronal-annealing behavior of the defect-trapped positron lifetime, τ_2, and the intensity of this component, I_2, are shown for high-purity α-Fe electron irradiated to two different doses (initial Frenkel-pair concentrations of ~0.7 and ~7 x 10^{-4}). It seems clear from fig. 12 that vacancy clusters are being formed at temperatures ~220K, although these clusters with 250 ≲ τ_2 < 300 ps do not appear to be well-defined three-dimensional voids, which would yield a somewhat higher lifetime for positrons trapped therein. Furthermore, the annealing behavior of I_2 in the low-dose sample, in combination with the absence of any change in τ_2 at ~140K, indicates that vacancy-interstitial recombination occurs at ~140K in electron-irradiated a-Fe. This work, and a number of others in various laboratories, points up a particular and unique advantage of PAS in the study and characterization of defects in irradiated metals, namely, the sensitivity of the positron and its annihilation characteristics to both individual vacancies and their clusters up to sizes large enough to be considered well-defined voids. This sensitivity is unique to PAS in comparison with the more traditional techniques (e.g., electrical resistometry, transmission electron microscopy, etc.) for defect and radiation damage analysis.

We finally turn to an example of a set of investigations on void formation during ischronal annealing following irradiation of Mo by 1.5 x 10^{18} cm^{-2} fast neutrons [27] or 2 x 10^{18} cm^{-2} electrons [28], the latter of which has been futher quantitatively analyzed [29] in terms of the vacancy-clustering process. Figure 10 shows the post-irradiation annealing behavior of the defect-trapped positron lifetime, τ_2, in Mo from [27] and [28]. It can be seen that while τ_2 in the electron-irradiated case has an initial value representative of the vacancy in Mo, the initial value of τ_2 in the neutron-irradiated case is already considerably higher, indicating the void-like nature of the depleted zones present in this case. Upon ageing at elevated temperatures, vacancy precipitation into voids is indicated by the continuous increase of τ_2 up to values ~450 ps. The rise of τ_2 above these values at higher temperatures has subsequently been shown [30] to be due to impurity contamination of the voids, an effect to which PAS is also quite sensitive and a potentially useful

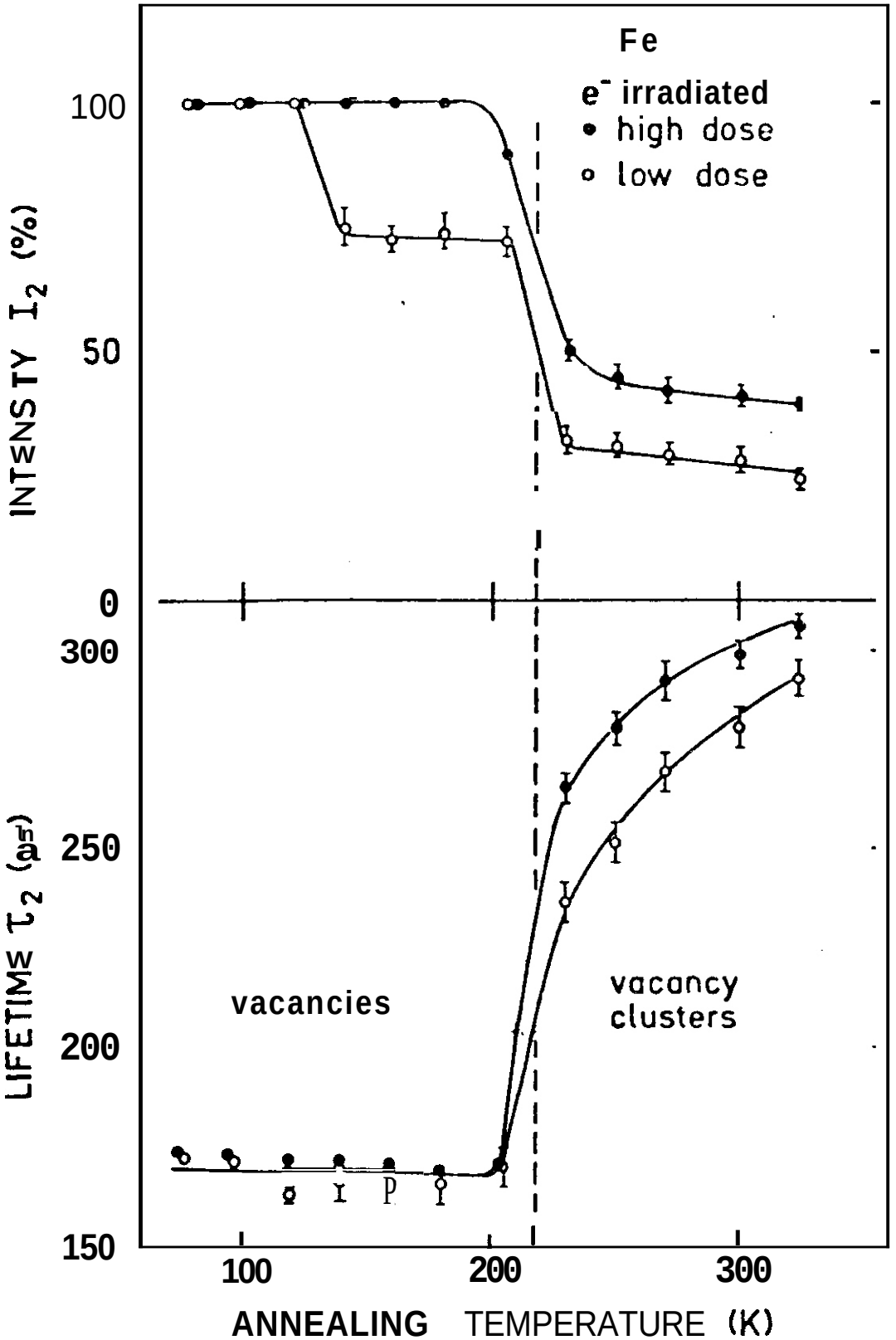

Fig. 9 The lifetime τ_2 and intensity I_2 of trapped positrons in electron-irradiated high-purity a-Fe versus isochronal-annealing temperature; from [12].

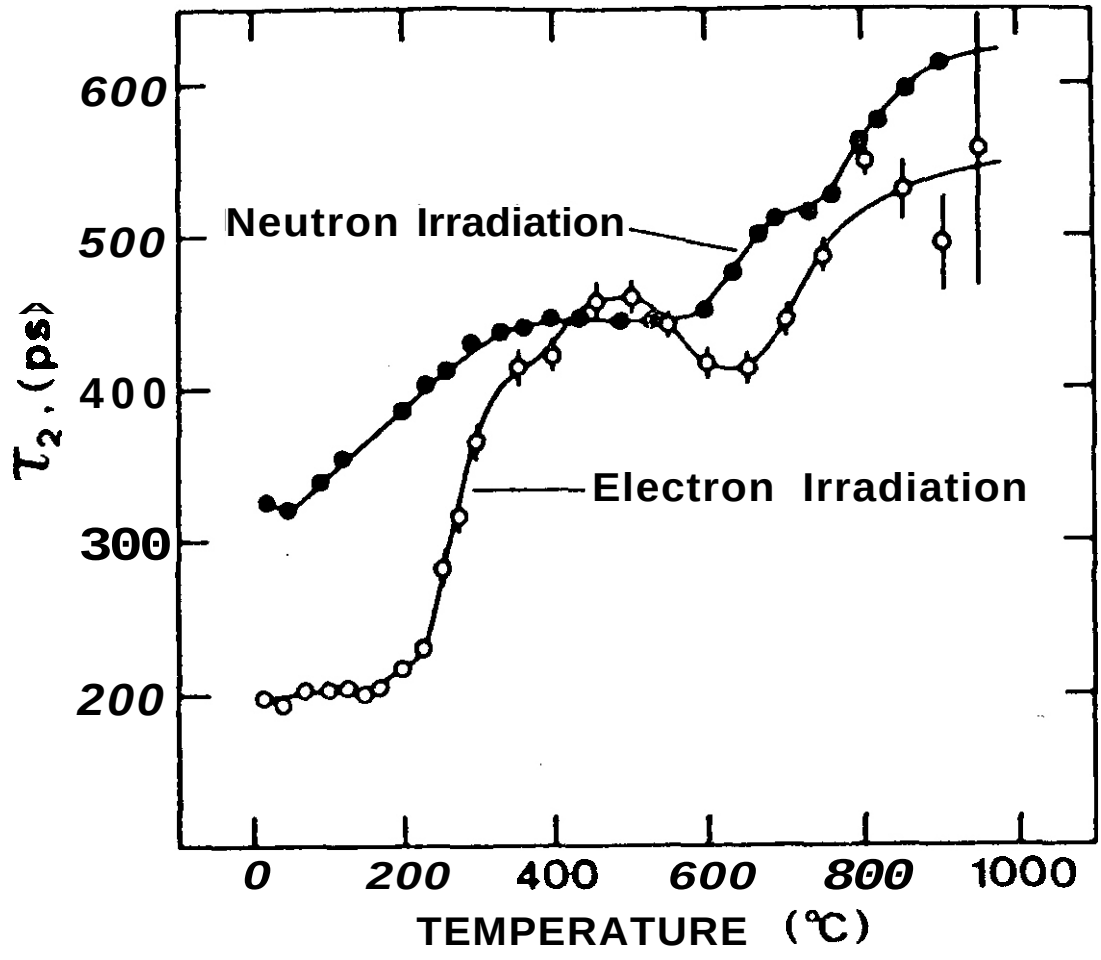

Fig.10 Isochronal-annealing behavior of the defect-trapped positron-lifetime τ_2 in neutron-irradiated [27] and electron-irradiated [28] Mo; from [30].

investigative tool.

In an attempt to make such PAS lifetime data more quantitatively useful in investigating the void-formation process, theoretical estimates using the jellium model have been made [29] of the positron lifetime in its void-trapped state in Al and Mo as a function of the number (1...50) of vacancies in assumed-spherical clusters, shown in fig. 11(a). The application of these calculations to the results of [28] are shown in fig. 11(b), in which the deduced number of vacancies in the (average) microvoid as a function of annealing temperature is indicated. While these calculations are still rather crude, especially in the case of very small clusters (e.g., divacancies and trivacancies), they indicate clearly the additional potential of PAS as a detailed quantitative tool for the analysis of defect-clustering processes in metals; a potential that will be more fully realized with the availability of more sophisticated theoretical models for positron annihilation in small vacancy clusters.

V. CONCLUSION

In conclusion, it is evident that positron annihilation spectroscopy has already become a valuable technique in our arsenal of methods for the study of atomic defects in metals. Owing to the ability of the positron to localize in a variety of metal defects where it subsequently annihilates yielding information regarding its local electronic environment, we now have a new and unique tool available for radiation damage analysis in metals, which both complements and supplements previously available methods. Many new advances in PAS experimental and theoretical techniques and additional applications to problems concerning defects and microstructures in metals are evolving in this rapidly developing area [31]. Nevertheless, it already seems clear that in the future PAS will continue to increase its usefulness for the characterization of defects and the study of radiation damage in metals.

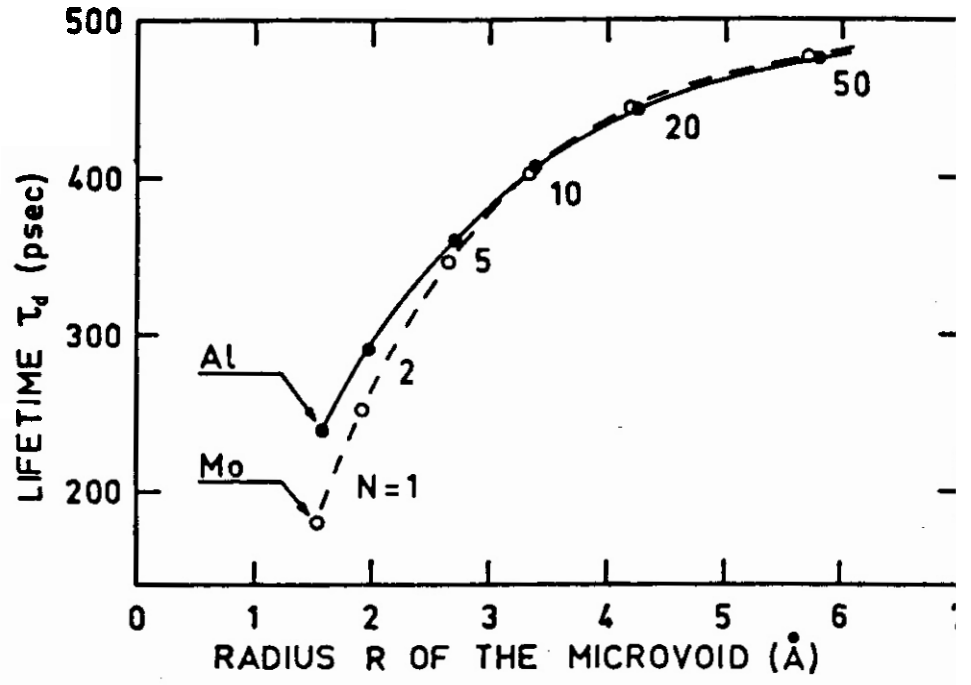

Fig. 11A. Calculated positron lifetimes in microvoids in Al and Mo as a function of void-radius R; N is the number of vacancies in the assumed-spherical void (Ref. 29).

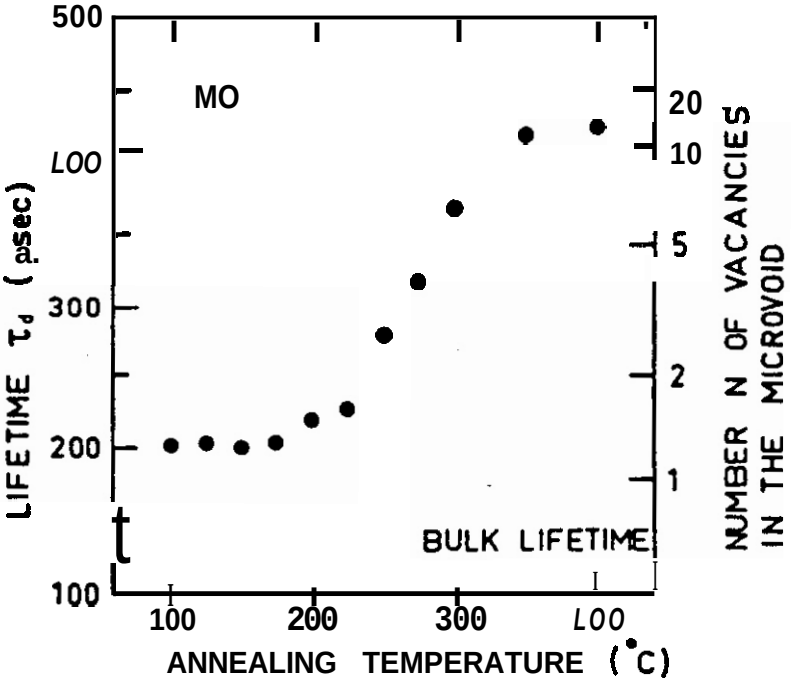

Fig. 11B. A combination of calculation results from Ref. 29 for Mo shown in Fig. 11A and the experimental positron lifetimes from Ref. 28 shown in Fig. 10 indicating the estimated number of vacancies per average-size microvoid as a function of annealing temperature (Ref. 29).

REFERENCES

1. A. Seeger, Crystal Lattice Defects 4, 221 (1973).

2. A. Seeger, J. Phys. F: Metal Phys. 3, 248 (1973).

3. M. Doyama and R. R. Hasiguti, Crystal Lattice Defects 4, 139 (1973).

4. A. Seeger, Appl. Phys. 4, 183 (1974).

5. W. Triftshäuser, Festkörperprobleme (Advances in Solid State Physics) XV, 381 (1975).

6. R. W. Siegel, J. Nucl. Mat. 69 & 70, 117 (1978) (Proc. Intl. Conf. on the Properties of Atomic Defects in Metals, Argonne 1976).

7. R. N. West, in Positrons in Solids, P. Hautojärvi, ed. (Springer-Verlag, Berlin, Heidelberg, 1979) p. 89.

8. R. M. Nieminen and M. J. Manninen, in Positrons in Solids, P. Hautojärvi, ed. (Springer-Verlag, Berlin, Heidelberg, 1979) p. 145.

9. R. N. West, Positron Studies of Condensed Matter (Taylor and Francis Ltd., London, 1973); ibid, Adv. in Phys. 22, 263 (1973).

10. I. Ya. Dekhtyar, Phys. Reports (Phys. Lett. C) 9, 243 (1974).

11. R. P. Gupta and R. W. Siegel, Phys. Rev. Lett. 39, 1212 (1977); ibid, to be published.

12. P. Hautojärvi, T. Judin, A. Vehanen, J. Yli-Kauppila, J. Johansson, J. Verdone, and P. Moser, Solid State Comm., in press (1979).

13. S. Berko, private communication.

14. W. Brandt, in Positron Annihilation, A. T. Stewart and L. O. Roelling, eds. (Academic Press, New York, 1967) p. 155.

15. B. Bergersen and M. J. Stott, Solid State Comm. 7, 1203 (1969).

16. D. C. Connors and R. N. West, Phys. Letters 30A, 24 (1969).

17. M. J. Fluss, L. C. Smedskjaer, R. W. Siegel, D. G. Legnini, and M. K. Chason, Proc. Fifth Intl. Conf. on Positron Annihilation, Lake Yamanaka, Japan, April 1979, in press; ibid, to be published.

18. S. W. Tam, S. K. Sinha, and R. W. Siegel, J. Nucl Mat. 69 & 70, 596 (1978)(Proc. Intl. Conf. on the Properties of Atomic Defects in Metals, Argonne 1976).

19. M. J. Stott and R. N. West, J. Phys. F: Metal Phys. 8, 635 (1978).

20. M. J. Fluss, L. C. Smedskjaer, M. K. Chason, D. G. Legnini, and R. W. Siegel, Phys. Rev. B 17, 3444 (1978).

21. W. Triftshauser and J. D. McGervey, Appl. Phys. 6, 177 (1975).

22. S. Nanao, K. Kuribayashi, S. Tanigawa and M. Doyama, J. Phys. F: Metal Phys. 7, 1403 (1977).

23. K. Maier, M. Peo, B. Saile, H. E. Schaefer, and A. Seeger, Phil. Mag. A, in press (1979).

24. M. Doyama, J. Nucl. Mat. 69 & 70, 350 (1978)(Proc. Intl. Conf. on the Properties of Atomic Defects in Metals, Argonne 1976).

25. S. Mantl and W. Triftshauser, Phys. Rev. Lett. 34,1554 (1975).

26. S. Mantl and W. Triftshauser, Phys. Rev. B 17, 1645 (1978).

27. K. Petersen, N. Thrane, and R. M. J. Cotterill, Phil. Mag. 29, 9 (1974).

28. M. Eldrup, 0. E. Mogensen, and J. H. Evans, J. Phys. F: Metal Phys. 6, 499 (1976).

29. P. Hautojärvi, J. Heiniö, M. Manninen, and R. Nieminen, Phil. Mag. 35, 973 (1977).

30. N. Thrane and J. H. Evans, Proc. Fourth Intl. Conf. on Positron Annihilation, Helsingør. Denmark, August 1976, unpublished, part 2, p. 100.

31. Proc. Fifth Intl. Conf. on Positron Annihilation, Lake Yamanaka, Japan, April 1979, in press.

HIGH SPATIAL RESOLUTION CHEMICAL MICROANALYSIS IN DAMAGE STUDIES

David C. Joy
Bell Laboratories
Murray Hill, NJ 07974

I. INTRODUCTION

A valuable adjunct to high resolution micro-structural studies of damaged materials is the ability to determine the chemistry of the sample, if possible at about the same level of spatial resolution. This chemical micro-analysis should be able to both identify what elements are present in any given area of the sample and measure the concentrations of these elements. Such an analysis could then be applied to either the bulk composition of the specimen, or to the identification of second phases, precipitates or inclusions in the matrix of the sample.

The techniques of imaging and microanalysis at high resolution can be coupled by using an electron microscope equipped with spectrometers to detect and analyse the fluorescent x-rays and characteristic energy losses which occur as a result of the interactions between the electron beam and the sample in the microscope. Figure (1) shows the arrangement of the specimen, incident electron beam, and the spectrometers in such a device. The microscope could be either a conventional 100kV transmission electron microscope (TEM) equipped with a scanning attatchment (STEM), or else a dedicated STEM. In both cases the electron probe is focussed to a diameter of between 50 and 500A and scanned over the sample to generate a high resolution scanned transmission image of the specimen. This probe can also be used to select any region of interest for analysis. With modern commercial instruments the current density into this probed area is of the order of 20 amp/cm^2, corresponding to an incident current of about 10^{-10} amps at the sample.

With this instrumental configuration either, or both, of the spectrometer systems can be operated while an image is being collected. The microanalytical data obtained can thus be placed in the context of the microstructure of the specimen. In general, any specimen that is thin enough

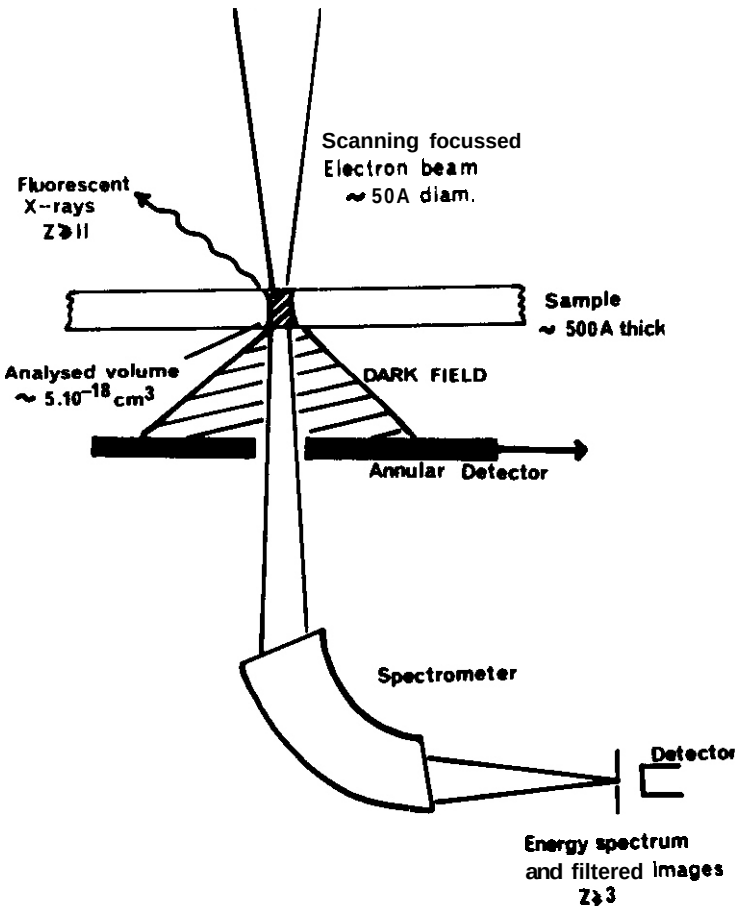

Figure 1. The schematic arrangement of the electron beam, the specimen, and the spectrometers in an analytical electron microscope.

to yield a good image will also be suitable for high spatial resolution micro-analysis, but because the requirements for the energy dispersive x-ray (EDXS) and electron energy loss (EELS) spectrometry are different the limitations placed on the sample in this respect will be discussed in more detail later.

II. ENERGY DISPERSIVE X-RAY MICROANALYSIS

The incident beam of electrons ionises some of the atoms in the thin sample as it passes through. These ionised atoms subsequently decay back in their ground state, and in so doing a fraction ω produce characteristic x-rays which can be collected by a suitable detector. The energy carried by any x-ray photon produced in this process represents the difference in binding energy between two allowed states of the aotm. This energy is unique to a particular element, and so a measurement of the energy (or wavelength) of the photon is sufficient to unambiguously identify the element from which it came. In the usual arrangement the x-rays are collected by means of a lithium drifted Silicon diode, placed in line of sight of the sample (see the sketch in figure 2a). The detector is typically of about 20 mm^2 active area and placed at 15 to 20 mm from the beam axis. The x-rays which enter it produce a charge pulse whose magnitude is directly proportional to the energy of the photon. This pulse can then be amplified, shaped and processed by a multi-channel analyser to yield a spectrum of the x-rays produced by the sample. As many as 10^4 photons/second can be processed in this way, thus all x-rays produced by the specimen and lying within the energy range accepted by the detector are effectively collected simultaneously.

With the notation of figure 2a, the number of x-rays per second detected from each atom of any element present in the volume of the sample irradiated by the beam is

$$\text{x-ray count rate} = J.\sigma.\omega.\ \text{Efficiency} \qquad (1)$$

where J is the incident electron flux (electrons/cm^2/sec), σ is the appropiate ionisation cross-section (cm^2/atom) and ω is the fluorescent yield for the

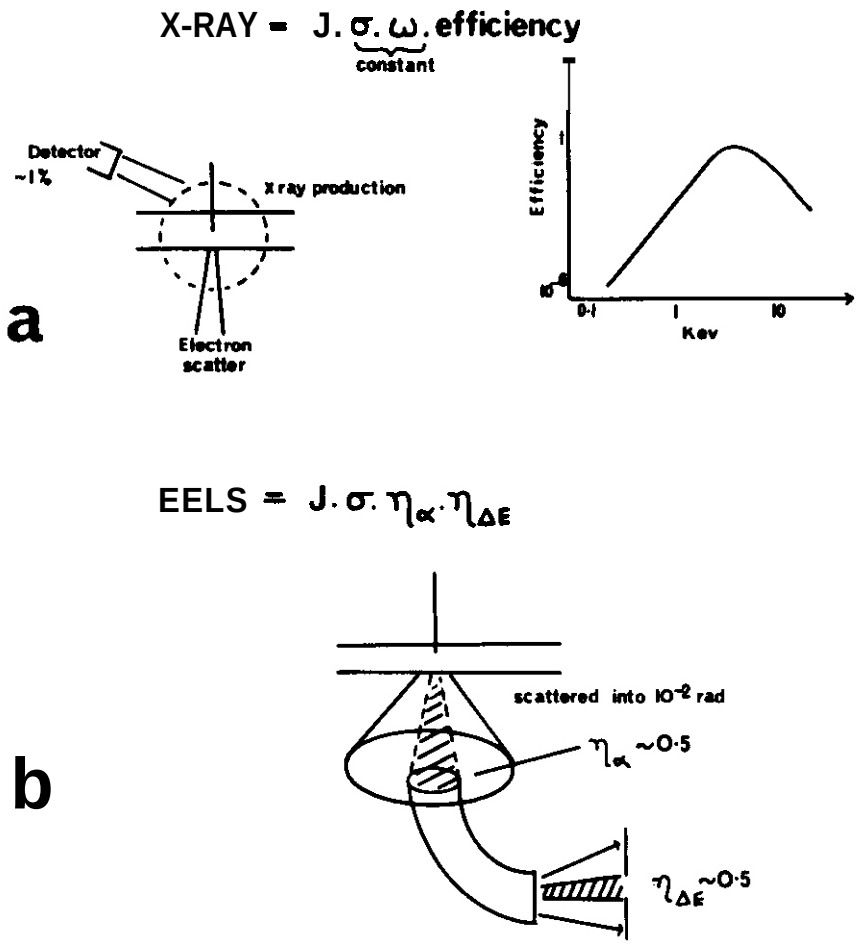

Figure 2. (a) The factors affecting the sensitivity of X-ray analysis, and (b) the factors affecting electron energy loss analysis.

x-ray collected. For all elements with an atomic number Z greater than 3 the product of $\sigma.\omega$ is about constant indicating that the number of x-rays produced is also constant. However the efficiency with which these x-rays are detected varies enormously as we move through the periodic table. The overall efficiency of collection and detection is controlled by two factors:

1. The x-rays are emitted uniformly into a spherical distribution from the thin foil, so that only those traveling directly towards the diode are detected. Taking the dimensions quoted before as a guide, the diode is subtending about 0.1 sterad at the sample and the collection efficiency is thus at most $0.1/4\pi$ i.e. about 1%.

2. In order to keep out the 100kV electrons (as well as other photons such as those lying in the visible range) the detector is protected by a beryllium window some 8 microns thick. In addition there are gold layers on the silicon to make connections and form a Schottky diode. Between them these metals absorb soft x-rays so that, for photons of 1 keV energy or less, the effective detection efficiency falls rapidly to zero. At the other end of the spectrum high energy photons (energies of 10 keV or more) can pass right through the diode, so that again the detection efficiency will fall, giving the overall response sketched in figure 2a. Within the optimum energy range (2 - 10 keV) x-rays from all elements above Mg in the periodic table can be obtained. Assuming an incident electron flux of 20 amp/cm^2, an analysis time of 100 seconds and a properly adjusted spectrometer system, figure 3 shows the minimum mass of the element Z that can be detected. In the presence of other elements the sensitivity of the analysis will be less because of the Bremstrahlung background contributed by the matrix in which the element is sitting. The amount by which the MDM is increased will depend on the distribution of the element within the matrix, as well as on the composition of this matrix.

The optimum case is that in which the element of interest is present as a precipitate etc and with a thickness close to that of the foil. In such a case the electron beam can be focussed down so as only to irradiate the area required, and the MDM will then be close to the values predicted from figure 3. The procedure just described raises the mass fraction of the element in the volume analysed to a value close to unity. In other, less

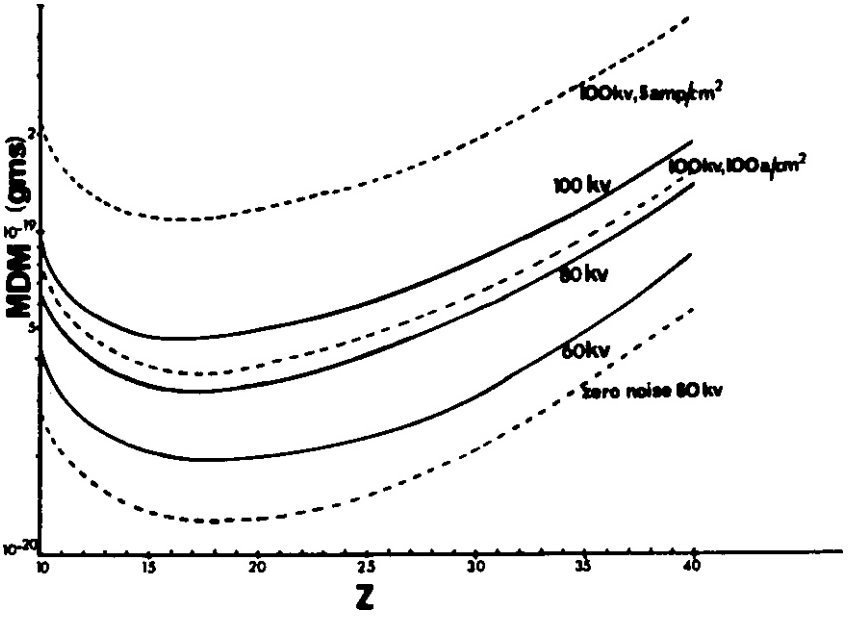

Figure 3. The variation in minimum detectable mass (MDM) as a function of atomic number in EDXS. See reference 1.

favorable, conditions (such as a homogeneous distribution of the element) where the mass fraction is substantially less than one, detection may only be possible if the beam is spread so as to irradiate the greatest volume of material so maximising the x-ray production from the desired component. High spatial resolution microanalysis is thus not compatible with the detection of trace amounts of an element, except when that trace is highly localised.

The electron beam is scattered as it passes through the sample and, because the electrons have to lose very nearly all of their energy before they are no longer able to excite an x-ray, volume within which x-rays are produced is generally larger than that defined by the probe diameter and the thickness of the foil. To a good approximation (see ref. 2) the point-to-point resolution be obtainable in the EDXS mode is given by the expression

$$b = 6.24 \times 10^5 \, (Z/E_0).(\rho/A)^{\frac{1}{2}} \, . \, t^{\frac{3}{2}} \qquad (2)$$

where E_0 is the accelerating voltage in eV, ρ is the density in gm/cm^3 A is the atomic weight, t is the thickness of the foil in cm. and b is given in cm. Substituting typical values for 100kv operation shows that a resolution of 51, 81 and 214 A could be achieved in 1000A thick foils of carbon, aluminum and copper respectively. A performance of this quality will, however, only be obtained if the background of stray electron and x-ray production from scattering within the microscope is completely supressed (see several discussion of this in ref. 3).

So long as the foil is "thin" the number of x-ray photons produced is proportional only to the variables defined in equation 1, and a quantitation can therefore readily be performed. The relative concentrations of two elements A and B will be given by

$$C_A/C_B = N_A/N_B \cdot k_B/k_A \qquad (3)$$

where N_A, N_B are the x-ray counts recorded from the elements in some time period, and the terms k_A and k_B include the cross section, fluorescence yield and efficiency factors of equation 1. The k-ratios (k_A, k_B...etc)

can either be determined experimentally or calculated from first principles. In certain conditions, however, there may be appreciable absorption of the emission of one element by another shich must be accounted for even though the foil is thin[2]. This effect will, of course, always be more severe when the foil becomes thicker although on the other hand a thicker specimen produces many more x-rays. Balancing the conflicting claims of resolution, absorption and sensitivity it is reasonable to suggest that the ideal sample thickness for EDXS studies is about 1000A.

III. ELECTRON ENERGY LOSS SPECTROSCOPY

While the x-ray technique is ideal for many applications it cannot detect (with useful sensitivity) such important light elements as Be, B, C, N or O, because of the rapid fall-away in the efficiency of the x-ray detector. This problem can be overcome by using instead the technique of electron energy loss spectroscopy (EELS) in which the energy distribution of the electrons which have passed through the foil is examined. In order to ionize an atom a certain amount of energy is required, and this can only be obtained from the incident electrons. The energy spectrum of the transmitted electrons therefore shows characteristic features ("edges") at energies corresponding to the classical binding energies. These edges are as unique a property of the element as its x-ray lines, and they can therefore equally well be used for the purposes of elemental indentification.

The EEL analysis is performed by passing the electron beam into a magnetic "prism" which disperses it by an amount depending on its loss in energy relative to the incident beam. A selecting slit placed in the exit plane of the prism can then isolate electrons of any given energy loss and, by scanning the dispersion across the slit, an energy loss spectrum can be built up. This can be stored in a multi-channel analyser in a way analogous to the EDX spectrum, with the difference that the EEL spectrum is acquired sequentially. The time spent collecting any one elemental edge is thus only a small fraction of the total analysis time.

Figure (4) shows a typical EEL spectrum, taken from a thin carbon film contaminated with sulfur. Note that the intensity axis is plotted on a

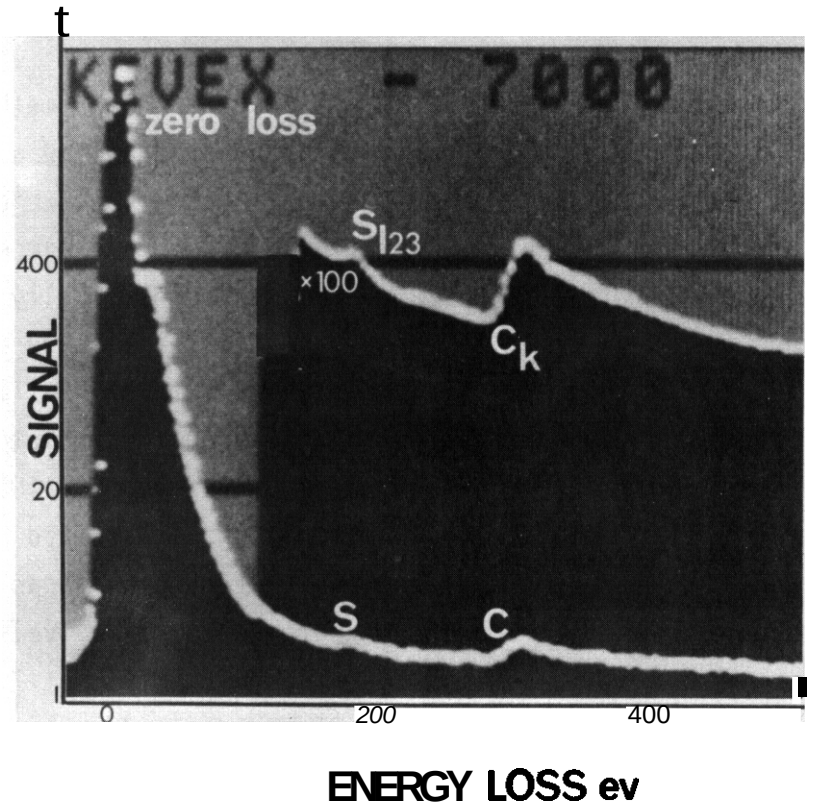

Figure 4. Electron energy **loss** spectrum recorded at 100 kV from a thin carbon **film.**

logarithmic scale, with a range of nearly 10^4 to 1. About 95% of the electrons are seen to have passed through the film losing less than about 20eV, but on increasing the recording gain of the system, two edges at energy losses of about 180 and 280 eV can be seen, these representing the L_{23} edge of sulfur and the K-edge of carbon respectively. A simple measurement of the energy loss at which the edge starts is sufficient to identify the element responsible.

The energy loss technique has two advantages over the EDXS method. Firstly, we are observing the primary event (the ionisation of an atom) rather than the secondary decay which produces the x-ray. The EEL count rate (see figure 2b) is thus proportional only to J and σ, and since σ rises as Z falls the sensitivity of an EEL analysis should actually be better for light rather than heavier elements. Secondly, the transmitted electrons are forward scattered, a majority of them lying within 10 milliradians of the incident beam axis. A practical electron spectrometer can thus collect a fraction, $\eta\beta$, of this signal that is close to 100%. and use it for analysis. The fraction, $\eta\beta$, of the signal accepted by the spectrometer that is actually passed through the selecting slit can also be very high, so that the inherent sensitivity of EEL micro-analysis is excellent. Figure 5 shows the estimated MDM, as a function of Z, for an optimised EELS system compared to the EDXS data discussed above. The advantage of the EELS technique for light elements is clear. However, as in the x-ray case, these idealised predictions are modified when the element is analysed in the presence of other materials. Full calculations of the likely sensitivity under practical operating conditions still remain to be done, but approximate computations suggest that in a matrix of medium Z (eg iron or copper) and 500A thick, a 200A diameter probe might be able to detect as little as 10^6 carbon atoms.

Because the electrons collected by the electron spectrometer have only been deflected through small angles there is no beam spreading to consider and so the spatial resolution of the EEL technique will be governed only by the diameter of the incident probe.

The thickness of the specimen is important in determining the form of the EEL spectrum. Figure 6 shows the shape of the nitrogen K-edge,

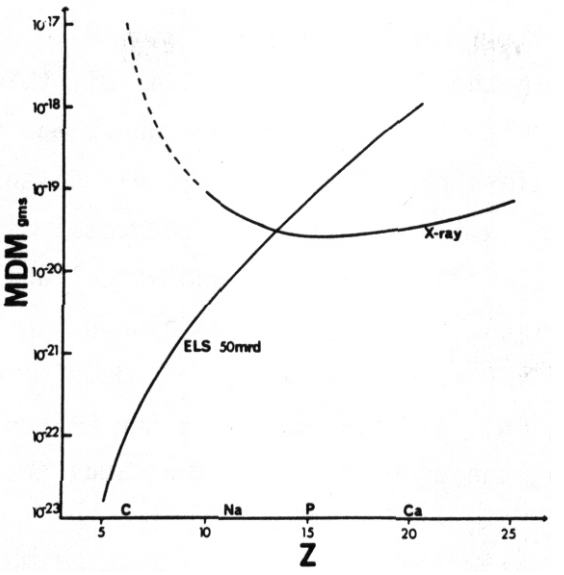

Figure 5. A comparison of the minimum detectable mass sensitivities, as a function of Z, for EELS and EOXS at 100 kV, J = 20 amp/cm^2.

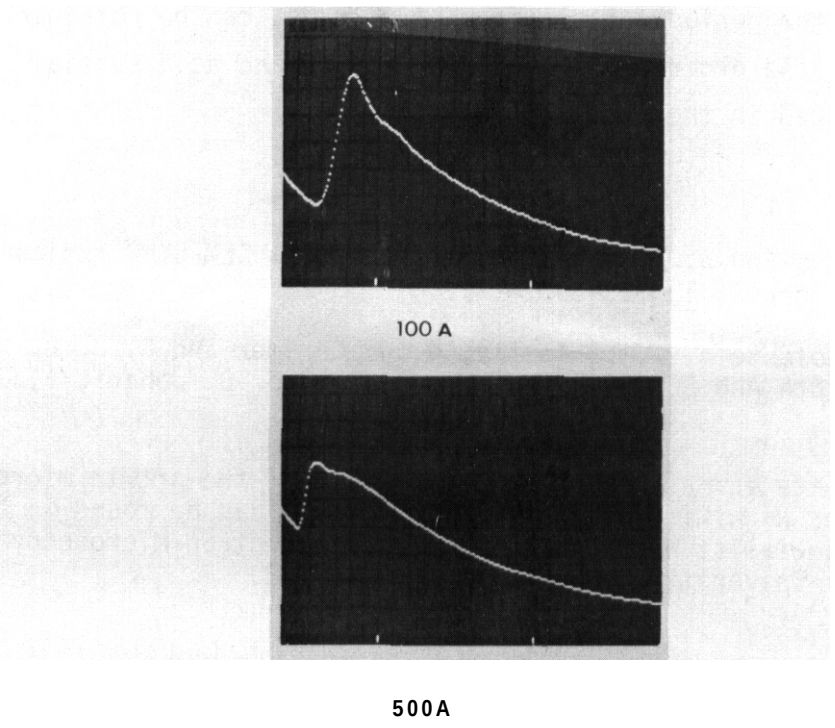

Figure 6. A comparison of nitrogen K-edges from silicon foils 100 and 500 Å thick showing the effects of multiple scattering on the visibility of the edge.

recorded from two samples of silicon ion-implanted with nitrogen to a concentration of 10%. In the first case, with a foil thickness of 100A, the edge is clearly visible but in the second, where the foil was 500A thick, the edge is both less pronounced and visibly distorted. A further increase in thickness can actually result in the total disappearance of the edge with the consequent loss of micro-analytical ability. Unlike the x-ray case, the best EEL specimen is thus always the thinnest Techniques for the quantitation of EEL spectra are now well developed both for relative and absolute concentrations (see ref. 3) using the K- and L-edges obtained from the elements giving these edges within the usual energy loss range of interest (0 - 1 keV).

IV. SUMMARY

To summarise therefore, taken together the EDXS and EELS techniques provide the means wherebye chemical micro-analytical data covering all the elements in the periodic table from Li upwards, can be obtained with a sensitivity of the order of 10^{-19} gms or better and at a spatial resolution measured in the range of 50 to 300A.

REFERENCES

1. O. C. Joy and D. M. Maher; Proc. 10th ANN. SEM SYMP (Chicago:IITRI) ed. O. Johari, 1, 325-335, 1977.

2. J. I. Goldstein, J. L. Costly, G. W. Lorimer and S. J. B. Reed; Proc. 10th ANN.SEM.SYMP (Chicago:IITRI) ed. O. Johari, 1, 315-324, 1977.

3. A complete summary of the present state-of-the-art in microanalysis together with many valuable review papers can be found in "Proceedings of a Specialist Workshop on Analytical Electron Microscopy" (Ithaca: Cornell University) MRL Report #3082, 1978.

HIGH RESOLUTION TRANSMISSION ELECTRON MICROSCOPY AND MICRODIFFRACTION FOR RADIATION DAMAGE ANALYSIS

Robert Sinclair
Department of Materials Science and Engineering
Stanford University
Stanford, California 94305

I. INTRODUCTION

High resolution TEM techniques have developed to quite a sophisticated level over the past few years. In addition TEM instruments with a scanning capability have become available comercially which permit in particular the formation of a small electron probe at the specimen. Thus direct resolution and microdiffraction investigations of thin specimens are now possible, neither of which have been employed to any great extent in the analysis of radiation damage. This abstract highlights some recent advances which are thought to be relevant to this specific area of research.

11. HIGH RESOLUTION TEM

A. Structure Imaging

The electron micrograph containing the most information about the specimen is produced by using as many diffracted electron beams as pssible in the image formation process. Thus 'structure images" are taken with the transmitted beam and many (>20) diffracted beams passing through the objective aperture. The experimental conditions for obtaining readily interpretable pictures are quite stringent: the specimen should be thin (say less than 100Å for a lOOkV microscope), exactly oriented to a zone axis orientation and the objective lens focus set to the appropriate value to bring the participating reflections together at the correct amplitude and phase (Scherzer focus). This type of imaging has been pioneered by Iijima, Cowley and coworkers and is reviewed in Physics Today (March 1977). with many original articles contained in Acta Cryst. 1972 onwards.

The resolution limit of lOOkV microscopes is in the range 3-48 and so pictures of atomic arrangements can only be taken in those materials

for which the separation of heavy metal atoms is of this order. This requirement is filled by many oxide systems, but not by close packed materials such as metals or many useful structural ceramics. The identification of point defects and their migration has been demonstrated in a niobium oxide (see Iijima et al. Acta Cryst. A30, 251 (1974)) and the structure of perfect and imperfect crystals has been examined in many systems at the atomic level. However the resolution limitation makes this mode unsuitable for radiation damage studies of many useful materials with current IOOkV instruments.

The resolution of a TEM is improved most dramatically by increasing the accelerating voltage, and some of the first micrographs illustrating this achievement have recently been published (see Horiuchi et al., Acta Cryst. A34, 939 (1978)). A resolution of about 2.28 has been found in current high voltage (1 MeV) high resolution microscopes in Japan, and this is approaching the level necessary to resolve atomic separations in metals (~2Å in the most convenient projections). Atomic level studies may then be possible with these higher resolution machines, and even point defects (e.g. interstitials) should be detectable from a contrast point-of-view (see Fields and Cowley, Acta Cryst. A34, 103 (1978)). Whether displacement damage occurring in the high voltage microscopes will detract from the images, or alternatively allow in situ radiation study, is an interesting prospect to follow.

B. Fringe Imaging

The investigation of metals at high resolution has been pursued by imaging one set of lattice planes, using transmitted and one diffracted beam for the imaging process. A study by Howe and Rainville (Rad. Eff. 16, 203 (1972)) showed that the fringes are distorted by the presence of radiation damage (e.g. voids, loops) but that it is extremely difficult to obtain meaningful information about the structure in the vicinity of the defect. Careful experimentation is required to obtain tractable data from this imaging mode, but several important metallurgical phenomena have been studied recently. Thus lattice distortion near dislocation cores may be

investigated when the dislocation line is straight and parallel to the imaging planes and electron beam (see Bourret et al. J. Microscopie Spectroscopie Electronique, 2, 467 (1977)). Stacking faults and interfaces may be imaged at atomic plane resolution provided they also are tilted parallel to the electron beam (see Sinclair, Proc. EMSA 35, 110 (1977)). Small precipitates and short-range order are readily visible. However the imaging of individual point defects does not seem possible by this mode.

One important area of application of the fringe method appears to be the determination of local composition from the local lattice fringe spacing. More sensitive compositional variations may be found than by energy dispersive techniques so long as the lattice parameter varies sensitively with composition, which particularly occurs for interstitial solid solutions. (see Sinclair and Thomas, Met. Trans. 9A, 373 (1978); Sinclair in "Analytical Electron Microscopy" edited by D. C. Joy et al., Plenum, in press). This approach may be quite significant for determining segregation phenomena in irradiated alloys.

C. Aberration Free Focus Imaging

The multi-beam image at lOOkV has been found recently to have superior resolution in some highly specific circumstances by taking the image at a well-defined value of defocus for which high spatial resolution reflections also contribute appropriately to image formation (see Hashimoto et al., J. Phys. Soc. Japan 42, 1073 (1977)). There is some serious current discussion over whether this mode will provide faithful information about imperfect crystals. Nevertheless some dramatic pictures have been presented on radiation damage in silicon, both on interstitial and vacancy clusters, which indicate that this mode certainly deserves further consideration in the future (see Izui et al, Proc. 9th Int'l Congr. on Electron Microscopy 1, 292 (1978), Proc. EMSA, 37 in press (1979)).

111. MICRODIFFRACTION

An alternative way to extract structural information about materials is from a diffraction pattern. In conventional transmission electron

microscopy the patterns are taken areas as small as 1μ diameter, but not lower than this because of spherical aberration errors.

Scanning TEM instruments utilise a small electron probe to produce the image, and this can be employed in turn to limit the volume of material through which the electrons pass and from which the microdiffraction pattern is obtained. Regions only 40Å in diameter are relatively easy to probe, and smaller areas are quite feasible in STEM's fitted with a field-emission electron source.

There are several ways of taking microdiffraction patterns (see Thompson et al. Norelco Reporter 1978). The electron probe may be stopped on the area of interest, or scanned over a small region. If the contamination rate is severe the diffraction pattern may degrade quite quickly in these modes. Alternatively a rocking beam mode may be utilized to circumvent this contamination problem (see Geiss, Appl. Phys. Lett. 27, 174 (1975)). The usual crystallographic information can be derived from such patterns although the beam divergence is often not sufficiently low for high precision data (e.g. about lattice parameters) to be obtained. Clearly the choice of microdiffraction pattern or direct lattice imaging for high resolution data depends on the type of information to be obtained. The decision between imaging and diffraction is often made with conventional experiments on the same basis and an additional perspective is commonly obtained by combining the two approaches.

An additional microdiffraction mode, which has exploited recently with some success, is the convergent beam method (see Steeds et al. Proc. 9th Intl Cong. on Electron Microscopy, 1, 620 (1978)). In this situation a highly convergent beam is focussed onto the area of interest and fine structure in the pattern can yield information on local crystallography and sensitive variations in lattice constant. Convergent beam patterns taken from areas containing lattice defects may prove to be quite useful in the future: a recent pattern from a dislocation in silicon shows splitting of all the Kikuchi lines apart from one set of lines, which is probably related directly to the exact structure of the dislocation. (see Spence, 9th Western Regional Conf. on Electron Mircroscopy, 1979; Bentley, the present workshop).

IV. SUMMARY

Quite a number of high resolution TEM imaging and microdiffraction techniques are now well developed but have rarely been applied to radiation damage analysis. Careful experimentation is required to take such pictures and a good theoretical background is often necessary for their interpretation. Nevertheless the level of aotmic resolution is being rapidly approached and this should provide an important tool for the critical investigation of radiation-associated problems.

APPLICATION OF ION CHANNELING TO RADIATION DAMAGE STUDIES*

S. T. Picraux
Sandia Laboratories†
Albuquerque, NM 87185

I. INTRODUCTION

Ion channeling has been used to study implantation damage in semiconductors, metals and insulators, and also to study impurities in association with the defects.[1-6] During ion channeling energetic particles undergo correlated collisions with the atomic rows or planes in a single crystal. This results in a spatial redistribution so that there is a large reduction in the particle probability density near the rows or planes and an increase near the channel center. Thus close encounter events, such as ion backscattering, are reduced approximately 1 to 2 orders of magnitude for channeled particles with lattice atoms in perfect lattice sites, whereas there *is* a much higher interaction probability with displaced atoms.

In this summary we primarily discuss those aspects of the technique which relate to the usefulness of channeling for high temperature radiation damage studies in metals. The majority of ion channeling studies have been applied to implantation damage in semiconductors. In contrast, little quantitative work on implantation or other radiation damage studies in metals have been carried out, although recent progress in the understanding of ion channeling now allows such studies to be performed.

II. ION CHANNELING ANALYSIS

Ion channeling is primarily sensitive to individually displaced atoms, such as interstitials, or to perturbations in the atomic rows or planes, such as may occur around dislocations or at voids in a crystal. The direct scattering of channeled particles by displaced atoms and the dechanneling of particles into random directions are monitored by ion backscattering. By energy analysis of the backscattered particles the depth of the interaction in the crystal can be determined. The channeling signal can be considered to consist of two components: (1) the direct scattering and; (2) the dechanneled component. For implantation damage in metals the direct scattering

*This work is supported by the U. S. Department of Energy, DOE, under Contract DE-AC04-76-DP00789.
†A U. S. Department of Energy Facility.

component is to first order neglibibly small under many conditions and the dechanneled signal at a given depth z is approximately given by[2-4]

$$\chi_D(z) \approx \chi_V(z) + [1-\chi_V(z)] \left\{1-\exp[-\sigma \int_0^z n(z')dz']\right\} , \qquad (1)$$

where χ_D is the dechanneling in the damaged crystal, χ_V is the dechanneling signal in a virgin crystal (in both cases normalized by the random scattering fraction at that depth), σ the cross section for dechanneling by the defects and n the density of defects. Thus under these assumptions the density of defects at a given depth z is given by

$$n(z) = \frac{\partial}{\partial z} \left\{\frac{1}{\sigma} \ln \left[\frac{1-\chi_V(z)}{1-\chi_D(z)}\right]\right\} , \qquad (2)$$

where the channeling parameter in brackets in Eq. 2 can be easily measured from the damaged and virgin crystals.

The physics of the process is contained within the cross section, σ, which may be calculated or, alternatively, measured provided the total density of defects is known in a given calibration sample. If a variety of defects of different σ result in comparable dechanneling signals simultaneously, then the channeling analysis will only give a qualitative indicator of the total damage present. However, if the radiation damage condition, together with the choice of channeling parameters, is such that a single type of defect dominates the dechanneling and the above analysis applies, then quantitative studies of the damage density with depth resolution ~100 Å can be carried out. In such studies it is always valuable to perform selected transmission electron microscopy (TEM) analyses on the samples to provide information on the larger defects present and to give further self-consistency to the interpretation of the channeling results.

111. APPLICATION OF ION CHANNELING

The dechanneling cross section σ depends on the nature of the defect and can exhibit quite different functional dependencies on channeling para-

meters such as the energy of the incident beam for different types of defects.[2-5] For example, the dechanneling for dislocation lines increases as the square root of energy, for stacking faults or voids is approximately independent of energy and for randomly distributed point defects such as interstitials decreases linearly with energy. Also, for the case where interstitial-like defects dominate, the direct scattering component becomes large and a different analysis may be applied; this is more frequently the case for semiconductors.' Thus, in addition to qualitative checks by transmission electron microscopy, measurements of the dechanneling at a given depth as a function of energy, for example, provide for a self-consistent check on the interpretation of the results. Also, by combining channeling measurements with TEM measurements for cases where independent determination of the density of defects can be made, the cross sections for such defects as dislocations have been measured and have been shown to give good agreement with simple theoretical estimates.[3]

Given preliminary measurements to sufficiently characterize the system and determine the applicability of the above analysis, then eq. 2 can be used to obtain the depth profile of the disorder. High concentrations of disorder are required, for example, $\sim 10^9$-10^{10} dislocation/cm^2, and good depth resolutions, ~ 100 Å, can be obtained. In this way the technique is highly complementary to transmission electron microscopy, where a survey of the nature of the defects can be readily obtained, but it is quite tedious to obtain quantitative depth information in general and, for the densities of defects which can be measured by channeling, is nearly impossible due to overlapping strain contrast.

As an example of the application of the technique we consider heavy ion implantation damage in Al.[2] By TEM one can show that a dense network of dislocations are formed by implantation to relatively hiqh fluences (10^{15}-10^{17}/cm^2), and from the energy dependence of the dechanneling consistency is found for dechanneling dominated by strain-like regions, as occur for dislocations. Figure 1 shows the channeling-ion backscattering spectra, both for a major axial and a major planar direction in Al. Implantation conditions correspond to a fluence of 7 x 10^{15}/cm^2 150 keV Ni ions at room temperature.

Figure 2 shows results of analysis of the Al spectra by Eq. 2 to obtain the depth distribution of the density of disorder. Also shown is the Ni

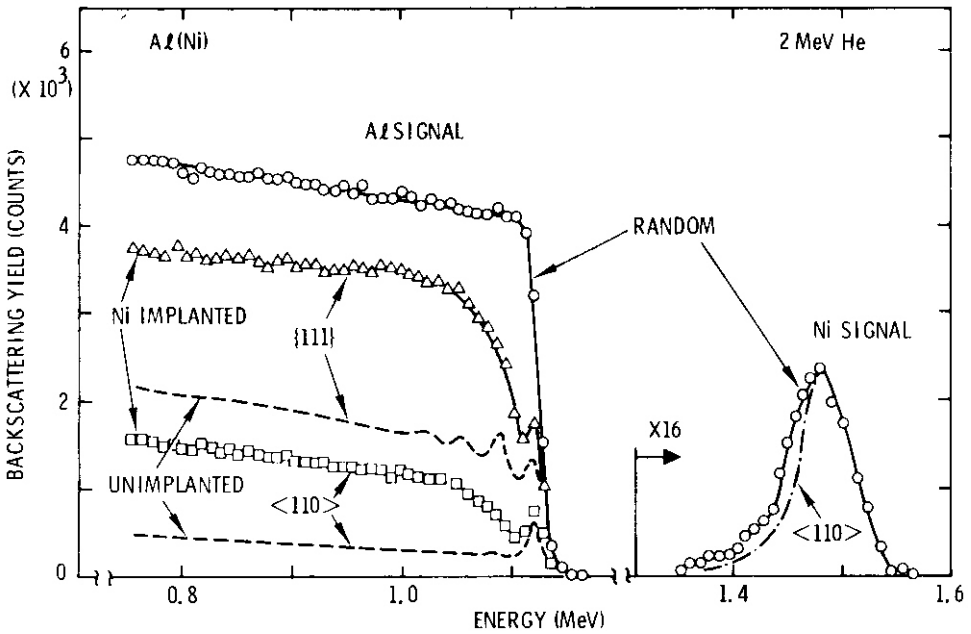

Figure 1. The 2-MeV He ion backscattering spectra for <110> axial and {111} planar channeling in AP before and after 7 x 10^{15} Ni/cm^2 implantation.

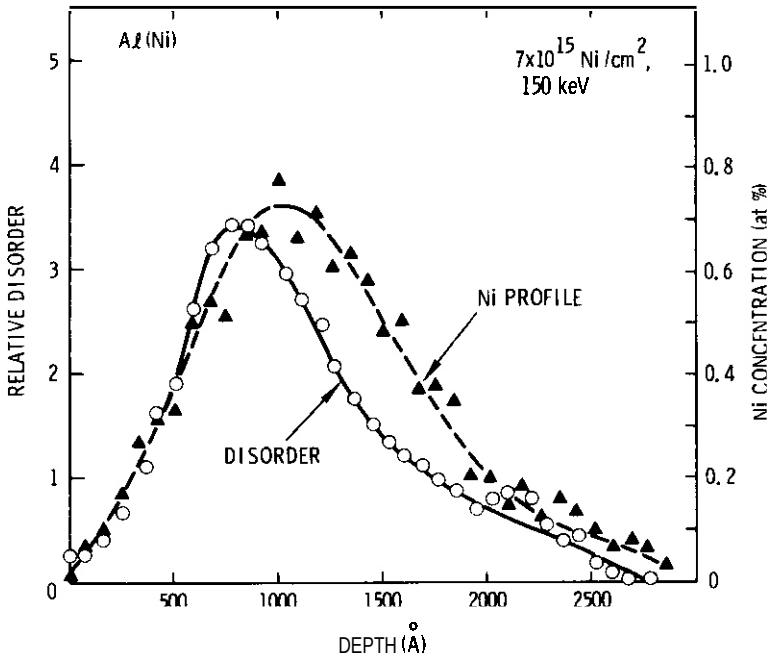

Figure 2. Disorder and Ni depth profiles obtained from the spectra of Figure 1.

profile obtained from the ion backscattering measurements. Planar channeling analysis is found to be quite useful here, although it is only recently that it has been applied to such studies. The depth distribution of the disorder relative to that of the implanted ions is quite similar to that predicted theoretically for the depth distribution of the primary damage energy production by the implanted ions. Also there is an indication of a somewhat lower density of defects near the surface, probably due to the competition of the surface as a sink for the primary defects which are produced.

IV. SUMMARY OF TECHNIQUE ADVANTAGES AND LIMITATIONS

The channeling technique is particularly useful for studies of high densities of defects where complementary techniques such as transmission electron microscopy may be difficult to apply quantitatively. Under conditions where a single type of defect dominates the dechanneling, the channeling technique can be quite quantitative. In addition, the depth distribution of defects can generally be determined in such cases without layer removal techniques. The functional dependence of the dechanneling varies with defect type, so that self-consistent checks can be made to further verify the nature of the defect probed. Sufficient sensitivity exists to both primary and high temperature secondary defects in metals such that a wide variety of radiation damage conditions may be studied. Also, there is an advantage that the ion channeling and backscattering analysis allows the solute depth distribution within the matrix to be monitored, which in many cases may be related to the defect flow and annihilation and the resulting damage distribution. In addition, by lattice location measurements information about the structure of solute-defect centers can also be obtained.[6]

Some of the disadvantages of the channeling technique are that single crystals are required and, as typically used, the lateral resolution is poor ($\sim$1 mm). In addition, the technique probes relatively shallow depths ($\lesssim$ 10 μm) and requires careful analysis for interpretation of the results. It is not a survey technique and can most profitably be applied when the dechanneling cross section and number density of defects is such that dechanneling by a given class of defects dominates over other defects present.

The channeling technique has recently been demonstrated to hold promise for application to radiation damage studies in metals, but relatively little work of a quantitative nature has been carried out so far. The technique is well suited to the high damage levels which might be anticipated in fusion reactor environments. One area of possible application would be studies of the mechanisms and kinetics of the secondary defect production and evolution as a function of fundamental parameters such as flux, temperature and solute concentrations. Finally, the channeling technique is most valuable when used in conjunction with other defect-specific techniques such as transmission electron microscopy.

REFERENCES

1. See, for example, Channeling, Ed. by D. V. Morgan (J. Wiley, NY, 1973) or Proc. Third Intl. Conf. on Ion Beam Analysis Ed. by E. A. Wolicki, J. W. Butler and P. A. Treado (North-Holland, NY, 1978).

2. S. T. Picraux, D. M. Follstaedt, P. Baeri, S. U. Campisano, G. Foti and E. Rimini, Proc. Intl. Conf. on Ion Beam Modification of Materials, Budapest, 1978 (to be published by Rad. Effects).

3. S. T. Picraux, E. Rimini, G. Foti and S. U. Campisano, Phys. Rev. B18, 2078 (1978).

4. S. T. Picraux and P. Rai-Choudhury, Semiconductor Characterization Techniques, Ed. by P. A. Barnes and G. A. Rozgonyi, Electronics Div., Vol. 78-3 (Electrochemical Society, Princeton, 1978) p. 447.

5. Y. Quere, J. Nucl. Materials 53, 262 (1974).

6. M. L. Swanson, L. M. Howe and A. F. Quenneville, J. Phys. F: Metal Phys. 6, 1629 (1976).

SMALL ANGLE AND DIFFUSE SCATTERING OF X-RAYS AND NEUTRONS

This subject was covered during the conference but no manuscript was available at publication.

THE STUDY OF DEFECTS AND RADIATION DAMAGE IN SOLIDS BY FIELD-ION AND ATOM-PROBE MICROSCOPY

David N. Seidman
Cornell University
Department of Materials Science and Engineering
and the Materials Science Center,
Bard Hall, Ithaca, New York 14853

I. INTRODUCTION

In this short paper an attempt is made to introduce the reader to the basic physical ideas involved in the field-ion and atom-probe field-ion microscope techniques (§2), and to the applications of these techniques to the study of defects and radiation damage in solids (53). The final section (54) discusses, in precis form, the application of the atom-probe field-ion microscope to the study of the behavior of implanted ^{3}He and ^{4}He atoms in tungsten. The paper is heavily referenced so that the reader can pursue his specific research interest in detail.

11. GENERAL BACKGROUND MATERIAL

The invention of the field-ion microscope (FIM) and the atom-probe FIM by Muller[1,2] has provided the experimentalist with tools which allow both the direct observation of all the common defects (point, line and planar) on an atomic scale and the simultaneous determination of chemical effects on an atomic scale (the minimum detectable mass is the mass *of* a single atom).

The atomic structure of the direct lattice is observed for those atoms which lie on the surface of a sharply pointed (~200 to 500Å in diameter) FIM specimen; the area imaged is $\sim 10^{-10}$ to 10^{-11} cm^2. The information concerning the positions of the atoms is carried to a phosphor screen or a channel electron multiplier array[3,4] by an imaging gas which is typically helium or neon. The imaging gas atoms are ionized, by a tunneling mechanism, in the high local electric fields (~4.5 V Å^{-1} to ionize a helium atom) that exist at the site of individual atoms as a result of a positive potential applied to a sharply pointed FIM sharply pointed FIM specimen.[5] The positively-charged ions are repelled from the specimen and then travel along the electric

field lines to the phosphor screen which is at earth potential; typically the phosphor screen is at a distance of between 4 to 10 cm from the FIM specimen. The image formed of the atoms on the surface of the FIM specimen, in the above manner, constitutes a point projection image with sufficient magnification to resolve individual atoms.

The interior of the specimen can be examined employing the field-evaporation process. The latter process consists of increasing the electric field to a value such that the potential energy curve of an ion on the surface of the specimen (this statement assumes that the state in which the metal atoms exist on the surface of the specimen is the ionic state) is deformed by the applied field to form a Schottky hump.[6] The ions then evaporate (sublime) by either jumping over this small Schottky hump or by tunneling through it; this process is called field desorbtion or field evaporation. The field evaporation process can be controlled by applying the positive potential in the form of short (1 to 10 msec in width) high-voltage pulses. This latter technique is called pulse field evaporation; it is possible by this technique to dissect an atomic plane one or two atom at a a time. Thus, the atoms contained within the interior of the specimen can be imaged, albeit at the surface, at a rate which is determined by the experimentalist. In practice one can examine $\sim 10^{-16}$ to 10^{-17} cm^3 of material, during the course of one experiment, via the pulse field evaporation technique. At Cornel1 we have developed semi-automated techniques for the process of applying the field evaporation pulse in conjunction with the simultaneous recording of large numbers of frames of 35 mm ciné film [$(15 \text{ to } 30)\times 10^3$ frames per day] as well as developing techniques for the scanning of this film.[7] It is clear, with the advantage of hindsight, that these two steps were essential to the successful application of the FIM technique to problems in the field of radiation damage.

The invention[2] of the time-of-flight (TOF) atom-probe FIM has provided us with a unique instrument for the study of the interaction of impurity atoms or alloying elements with point, line or planar defects. The TOF atom-probe FIM (hereafter called an atom probe) consists of an FIM combined with a special TOF mass spectrometer. This spectrometer allows the investigator to identify chemically any atom that appears in an FIM image. Thus,

it is now possible to both image the microstructural features of a metal specimen and to measure the mass-to-charge ratio (m/n) of individual atoms from preselected regions of a specimen with a lateral spatial resolution (i.e., within the surface) of a few angstroms and a depth spatial resolution that is determined by the interplanar spacing; the latter quantity can be tenths of an angstrom. An atom probe with a straight TOF tube has a mass-resolution ($m/\Delta m$) of $\sim$200 while an atom probe with a Poschenrieder lens[8] has an $m/\Delta m$ value of >1000.[9]

Additional material concerning the FIM and atom-probe techniques and their applications can be found in reference numbers 5, 10, 11, 12, 13, 14, 15, 16, 17. The work performed at Cornell in the fields of defect physics and radiation damage has been summarized in several review articles.[18-21] For technical details concerning the computer controlled atom probe we have constructed at Cornell see reference numbers 22-26.

III. A CATALOG OF APPLICATIONS TO THE STUDY OF DEFECTS AND RADIATION DAMAGE IN SOLIDS

In this section we present, in catalog form, a list of problems to which we have applied the FIM and atom probe techniques. The reader is referred to the references for the details concerning each problem.

A. Diffusive Properties of Self-Interstitial Atoms (SIAs)

1. Measured enthalpy change of migration (Δh^m_{1i}) of SIAs in both pure metals, alloys and order-disorder alloys.

2. Measured the pre-exponential factor (D^o_{1i}) of the SIA self-diffusion coefficient.

3. Have studied SIAs in Stages I, II, and III of ion, electron or fast-enutron irradiated specimens.

4. The particular systems studied to date are W, W(Re), W(C), Mo, Pt, Pt(Au), Ni_4Mo and Pt_3Co.

5. For details see reference numbers 18, 19, 21, 27-40.

B. Volume Change of Migration (Δv^m_{1i}) of SIAs

1. Measured Δv^m_{1i} for the SIA in W, Pt and Mo in detail. Experiments were also performed on Ni_4Mo and Pt_3Co but in less detail.

2. For further details see reference numbers 18, 19, 27, 28, 31, 37, 38, 40, 41.

C. Binding Enthalpy of an SIA to a Solute Atom (Ah^b)

1. Measured Ah^b by determining a dissociation enthalpy (Ah^d) and then determining Ah^b from the expression $\Delta h^d = Ah^b + \Delta h^m_{1i}$. The system Pt(Au) was studied in great detail and two detrapping stages (II_B and II_C) were observed in Stage II.

2. The systems W(Re) and W(C) were also studied but in less detail.

3. For further details see reference numbers 19, 21, **33, 36, 39,** 40.

D. Diffusive Properties of Vacancies

1. Measured ratio of divacancy concentration to monovacancy concentration for one quench temperature in platinum specimens.

2. From (a) it was possible to determine the Gibbs free binding energy (Δg^b_{2v}) in platinum.

3. Measured vacancy concentration in tungsten specimens which had been quenched from near the melting point.

4. The measurements discussed in (a) to (c) are important for interpreting the high-temperature self-diffusion data by point-defect mechanisms.

5. For further details see reference numbers 18, 42, 43, 44, 45, 46.

E. Diffusive Properties of Gases in Metals

1. Diffusion of ^3He and ^4He in tungsten and platinum.

2. Diffusion of ^1H and ^2H in tungsten.

3. For further details see reference numbers 47, 48, 49, 50, 51, 52.

F. Range Profiles of Low-Energy Implanted Gases in Metals

1. Range profiles of ^3He and ^4He in tungsten and platinum (100 to 1500 eV singly-charged ions).

2. Range profiles of ^1H and ^2H in tungsten.

3. For further details see reference numbers 47, 48, 49, 50, 51, 52.

G. Point-Defect Structure of Depleted Zones: The Primary State of Radiation Damage

1. Depleted zones in ion-irradiated metals [W, Pt, Pt(Au)]
   a. Dimensions of depleted zones (DZx)
   b. Number of vacancies per DZ.
   c. Vacancy concentration within DZs.
   d. The distribution of 1st-nearest-neighbor vacancy clusters.
   e. The radial distribution function (RDF) for the vacancies out to 9th-nearest-neighbor.

2. Effect of projectile mass (M_1) on the structure of DZs at constant projectile energy.

3. Effect of M_1 on the structure of DZs at constant reduced energy (E).

4. For further details see reference numbers 18, 20, 21, 49, 53, 54, 55, 56, 57.

H. Damage Profiles

1. Ne' (250 to 2500 eV) irradiated Ni_4Mo and Pt_3Co (order-disorder alloys). Damage profiles determined by measuring the change in the Bragg-Williams long-range order parameter(S) as a function of depth.

2. 30 keV W^+, Cr^+ or Mo^+ Irradiated Tungsten.

3. For further details see reference numbers 38, 49.

I. Sputtering of Surfaces

1. The sputtering of a metal surface is the result of the intersection of a collision cascade with it. In this work we compared the vacancy

structure of depleted zones, produced by 30 keV W^+, Mo^+, Cr^+, Cu^t, or Ar^+ ions, that were found to have intersected the surface of a tungsten FIM specimen with the depleted zones found in the bulk of the specimen.

2. For further details see reference number 57.

J. Voids in Neutron-Irradiated Metals [Mo, Mo(Ti), Fe(Cu)]

1. Void number density: need a number density of $\approx 10^{17} cm^{-3}$ in order to be able to make measurements.

2. Void size distribution: same comment as in X.a. applicable.

3. Direct observation of segregation.

4. For further details see reference number 58, 59, 60.

K. Distribution of SIAs in the Primary Damage State

1. *SIA* distribution in ion-irradiated tungsten (30 keV W^+, Mo^+, Cr^+).

2. Range of replacement collision sequences. (RCSs)

3. For further details see reference numbers 53, 61.

IV. RANGE PROFTLES OF LOW-ENERGY (100 to 1500 eV) IMPLANTED ^3He AND ^4He ATOMS AND THE OIFFUSIVITY OF ^3He AND ^4He IN TUNGSTEN

A. General Background

Current interest in the fundamental properties of helium in metals has been generated by the materials problems associated with the development of the 1iquid-metal fast-breeder reactor[62] and the controlled thermonuclear reactor.[63] However, because of a lack of appropriate experimental techniques the investigations *of* the range of *low-energy* (<1 keV) implanted He ions and the diffusivity of He in metals have been largely theoretical.[64-66] Measurement of the range profiles of implanted He ions have been confined to energies[67] >1 keV; furthermore, the measurement of both the range profiles of implanted He and the diffusivity of He in metals have relied exclusively on the trapping of He at lattice defects introduced as a result of heavy-ion irradiation.[68]

The accomplishments of our research on helium implanted in tungsten

were: (1) the establishment of the ability of the atom-probe FIM to detect either implanted ^3He or ^4He atoms retained in a perfect (i.e., totally defect-free) lattice; (2) the detection of the presence of an isolated and immobile ^3He or ^4He atom in a perfect tungsten lattice; (3) the measurement of the range profiles of low-energy (100 to 1500 eV) implanted ^3He or ^4He atoms in a perfect tungsten lattice; and (4) the measurement of the diffusivities of ^3He and ^4He in a perfect tungsten lattice.

The basic physical ideas involved in the experimental procedures are illustrated sequentially in Fig. 1. A single-crystal W FIM specimen, at an irradiation temperature (T_i), was irradiated in situ with $^3He^+$ or $^4He^+$ ions parallel to the [110] direction as shown in Fig. 1(a). To study the diffusional behavior of either ^3He or ^4He in tungsten it was necessary to implant the helium under the condition of no radiation damage. For example, a 300-eV ^4He atom can transfer a maximum energy of ~25 eV to a W atom in a head-on two-body elastic collision. Since the minimum displacement energy for the production of a stable Frenkel pair in W is ≈42 eV(69), no self-interstitial atoms (SIA's) or vacancies are created at an implantation energy of 300 eV for either ^3He or ^4He. Thus for the diffusion experiments a standard implantation energy of 300 eV was employed. With no SIA's or vacancies present to act as trapping centers, implanted ^3He or ^4He atoms can remain in the specimen only if ^3He or ^4He is immobile at T_i. Thus, the state of the W specimen after an implantation consisted of imnobile interstitial ^3He or ^4He atoms implanted in a perfect W lattice with a depth distribution that was determined solely by the range profile of the low-energy ions. Next the specimen was analyzed chemically, by the atom-probe technique, at a standard reference temperature (T_r), where $T_r \leq T_i$, and a ^3He or ^4He integral profile was plotted as shown in Fig. 1(b); this was an integral profile since it measured the cumulative number of ^3He or ^4He atoms as a function of the cumulative number of W atoms (depth) from the irradiated surface. The depth scale was converted from cumulative number of W atoms to angstroms from the measured number of W atoms per (110) plane contained within the cylindrical element samples; see Fig. 1(a). Finally the ^3He or ^4He range profile, Fig. 1(c), may be constructured by taking the first derivative of the integral profile shown in Fig. 1(b); or alternatively by plotting a frequency distribution diagram.

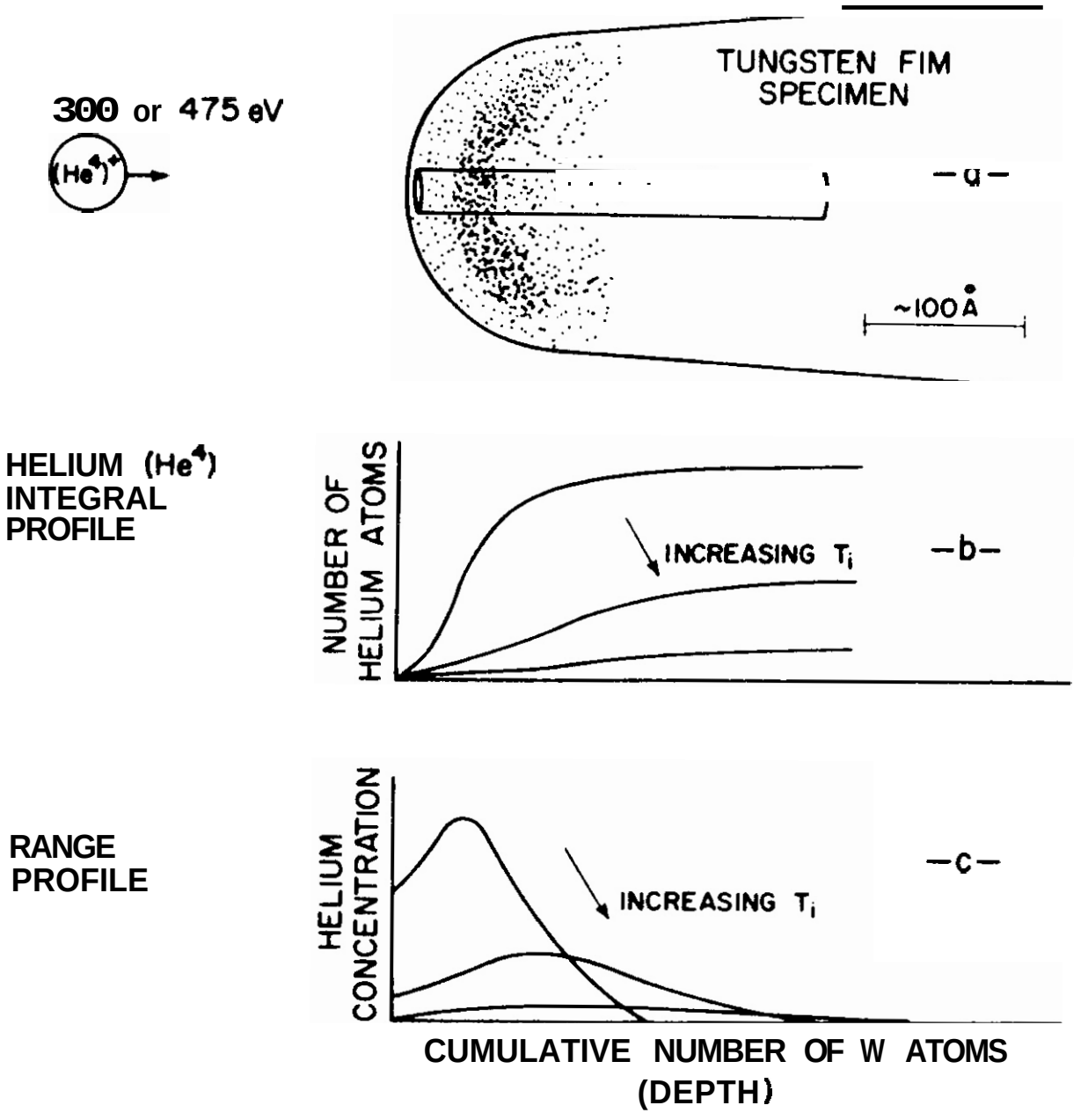

Figure 1. (a) The in situ irradiation of a W FIM specimen with 300-eV $^4He^+$ ions at a Ti where the implanted ^4He atoms are immobile. The density of spots corresponds to the approximate range profile of ^4He in W. The cylindrical volume element represents the volume chemically analyzed by the atom probe. (b) The number of ^4He atoms versus depth as a function of Ti. Note that the ^4He integral profile tends to flatten out as a T_i is increased. (c) The range profiles of ^4He in W as a function of Ti.

A novel technique for the determination of an absolute depth scale was developed; Fig. 2 schematically illustrates the method. During the atom-probe analysis the specimen was oriented and the magnification adjusted so that only the central portion of the W(110) plane was chemically analyzed. The specimen was then pulse field evaporated through the repeated application of high-voltage pulses. Three successive stages in the pulse field evaporation of one (110) plane are indicated in Fig. 2(a). As the plane was pulsed, field-evaporated atoms were detected as indicated by the positive slope in Fig. 2(b). When a plane was completely evaporated the slope of the curve in Fig. 2(b) returned to zero. Therefore the removal of one (110) plane resulted in a single-step increase in the plot of the number of W atoms detected versus the number of field-evaporation pulses applied to the specimen. Since the W lattice was employed as a depth marker, the absolute depth of each implanted ^{3}He or ^{4}He atom from the initial irradiated surface was measured to within one (110) interplanar spacing (≈2.24 Å) independent of the total depth of analysis. Thus the spatial depth resolution of the atom-probe technique is limited solely by the interplanar spacing of the region being analyzed.

B. Integral and Range Profiles of Low-Energy Implanted ^{3}He and ^{4}He Atoms

In this section we present a number of integral profiles and range profiles for both ^{3}He and ^{4}He which had been implanted in tungsten at 60 K. The term integral profile reflects the manner in which the data was recorded [see fig. 1(b)], whereas the range profile was constructed by plotting a frequency distribution diagram from the integral profile [see fig. 1(c)]. The range profile can also be obtained by drawing a smooth curve through the integral profile and taking the first derivative of this curve. In all cases we have obtained the range profile by the former rather than the latter technique.

Figure 3 exhibits ^{3}He integral profiles for the implantation energies 100, 500 and 1500 eV; the 100 eV profile is a composite of two integral profiles each with a dose of 4.7×10^{15} ion cm^{-2}; both the 500 and 1500 eV integral profiles were obtained after implanting to a dose of 3×10^{15} ion cm^{-2}. In fig. 4

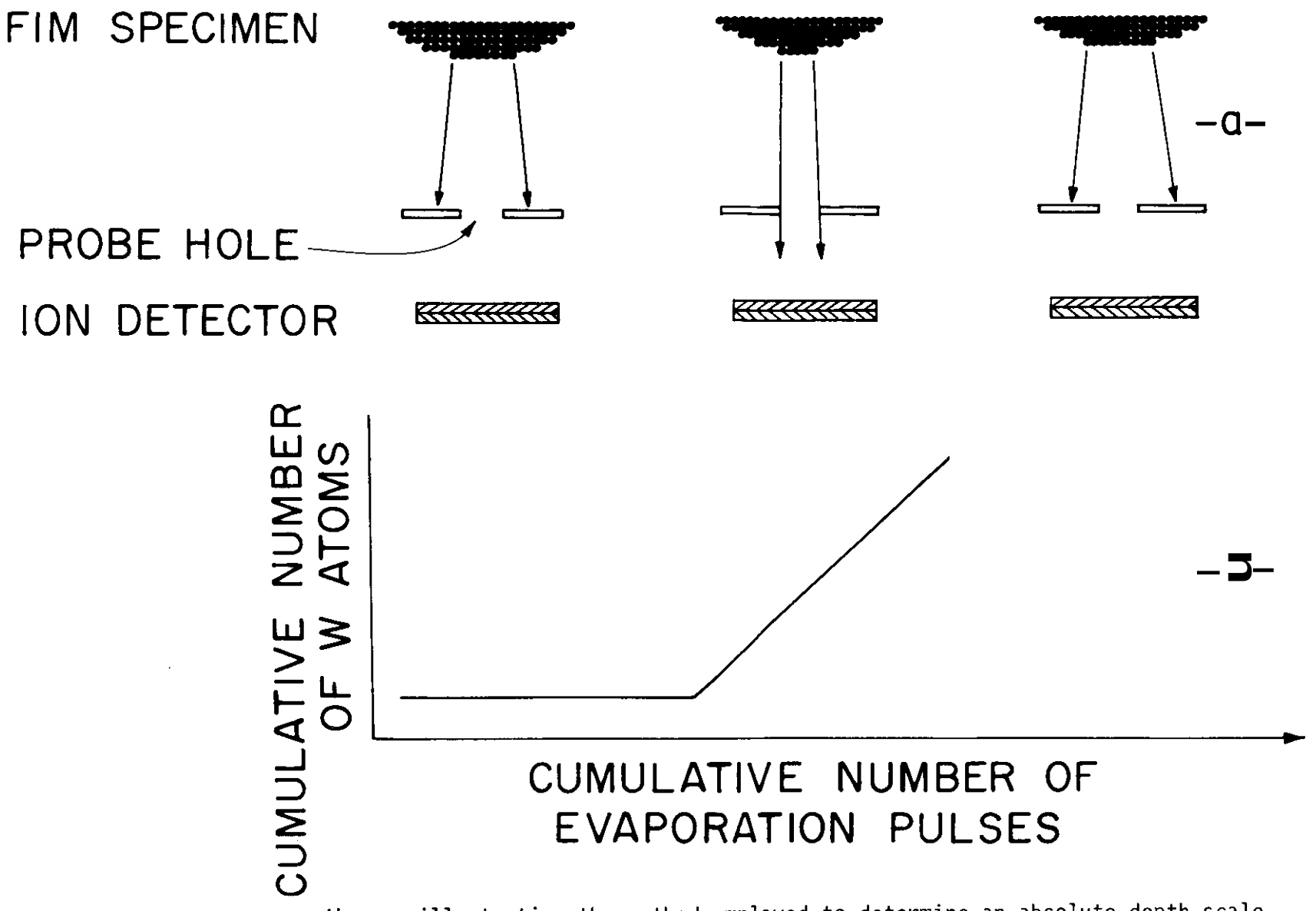

Figure 2 A schematic diagram illustrating the method employed to determine an absolute depth scale. Three states in the field evaporation of one (110) plane of W are shown in (a). The field-evaporation behavior of this plane is indicated in (b) by the steplike increase in the rate at which tungsten atoms are detected.

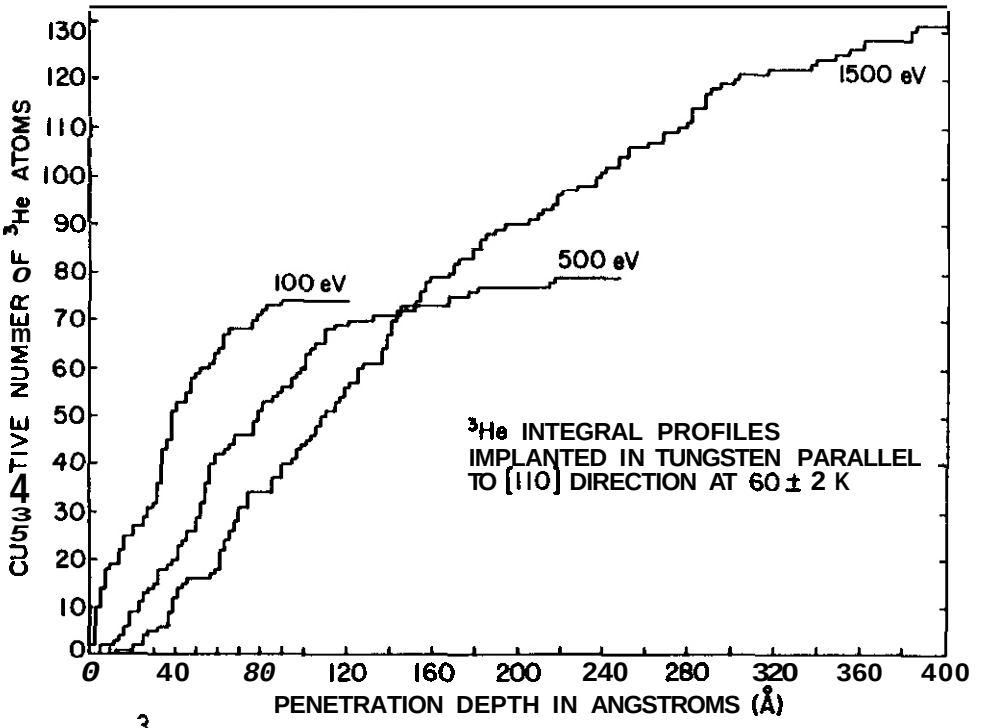

Figure 3. The ^{3}He integral profiles for the implantation energies of 100, 500, and 1500 eV. Tungsten specimens were implanted to 60 K parallel to the (110) direction.

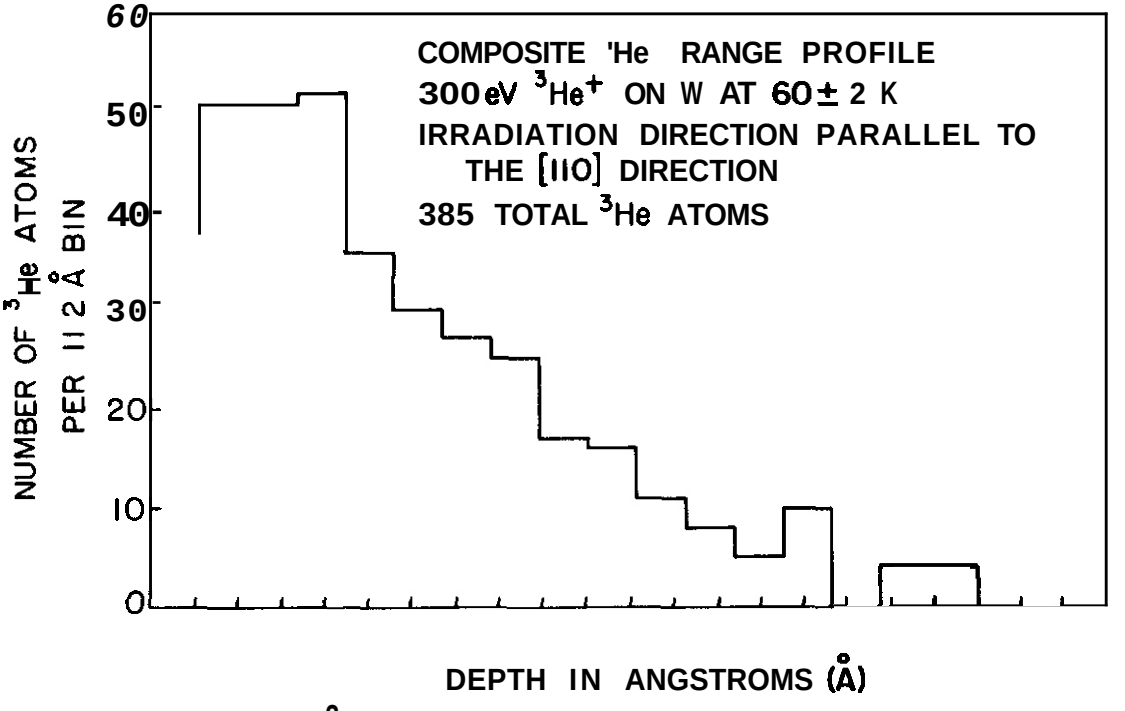

Figure 4. A composite ^{3}He range profile for all 300-eV implantations at 60K. A total of 385 3He events were involved in the construction of this range profile.

we show a composite range profile for 300 eV ^{3}He ions; this range profile was constructed from seven integral profiles and includes a total of 385 ^{3}He events; the values of the mean range ($\bar{x}$) and the straggling (Δx) are 54.9 and 41.5 Å respectively.

Figure 5 exhibits ^{4}He integral profiles for the implanation energies 150, 500 and 1000 eV; the 150 eV data consists of a single integral profile for a specimen that had been implanted to a dose of 3×10^{15} ion cm^{-2}; the 1000 eV data is for a single integral profile for a specimen that had received a dose of 4×10^{15} ion cm^{-2}. In fig. 6 we show a composite range profile for a 1000 eV ^{4}He implantation; this range profile was constructed from three integral range profiles and includes a total of 147 ^{4}He events; the values of $\bar{x}$ and Δx are 133 and 104.2 Å respectively.

All of the ^{3}He and ^{4}He integral profiles exhibited positive skewness as expected for low-energy irradiations (Biersack and Haggmark[70]); this implied that the mean range[7] was greater than the most probable range (or mode) and that the majority of the large deviations were to the right (positive) side of $\bar{x}$. The coefficient of skewness is related to the third moment about $\bar{x}$ and is given (Parratt[71]) by:

$$\text{Coefficient of Skewness} = \frac{\sum_{i=1}^{n} (x_i - \bar{x})^3}{N(\Delta x)^3} . \qquad (1)$$

where x_i is the measured depth of the ith detected helium atom from the initial irradiated surface, N is the total number of helium events detected and Δx is the standard deviation of straggling.

The values of $\bar{x}$ and Δx were calculated directly from the integral profiles for the ^{3}He and ^{4}He implantations. The values $\bar{x}$ and Δx must be corrected for the following systematic errors: (1) the random arrival of helium atoms at the surface of the specimen, from the residual partial pressure of helium, during the atom-probe analysis of the irradiated specimen; and (2) the effect of the finite curvature of the FIM tip. A detailed analysis of the above effects is given elsewhere (Amano, Wagner and Seidman[72]), where it was shown that the corrections to $\bar{x}$ and Δx were very minimal in our experiments. Thus we shall not employ the word uncorrected any further in this paper.

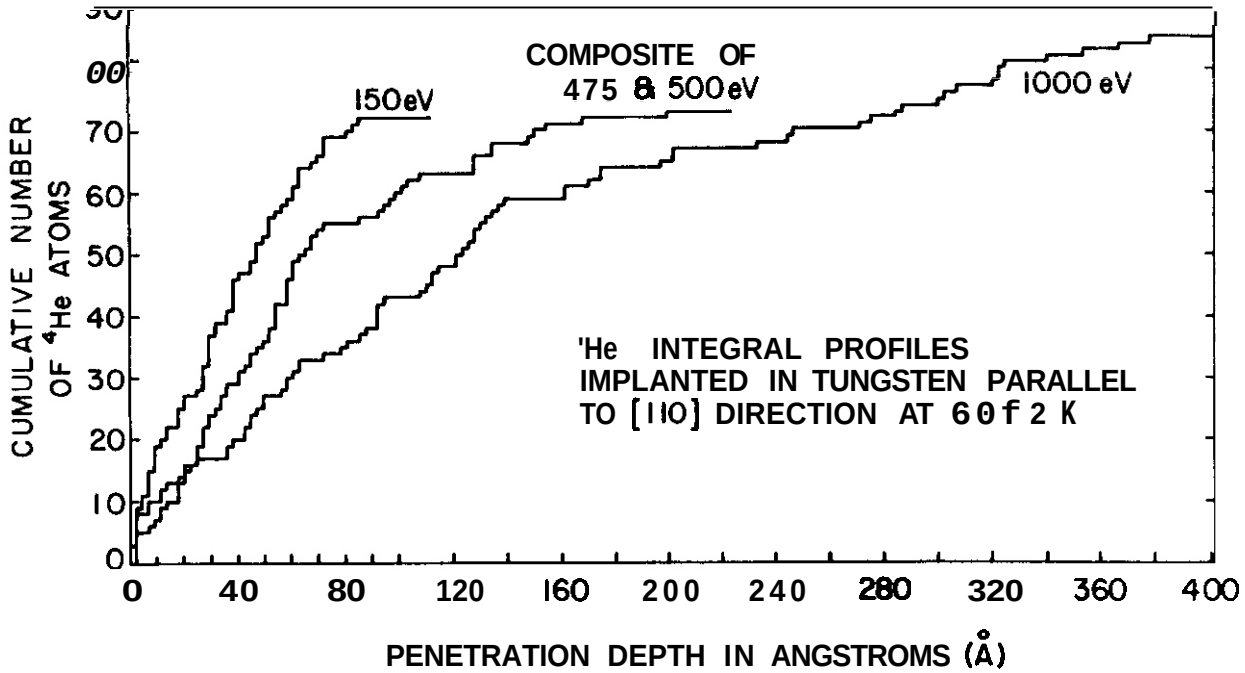

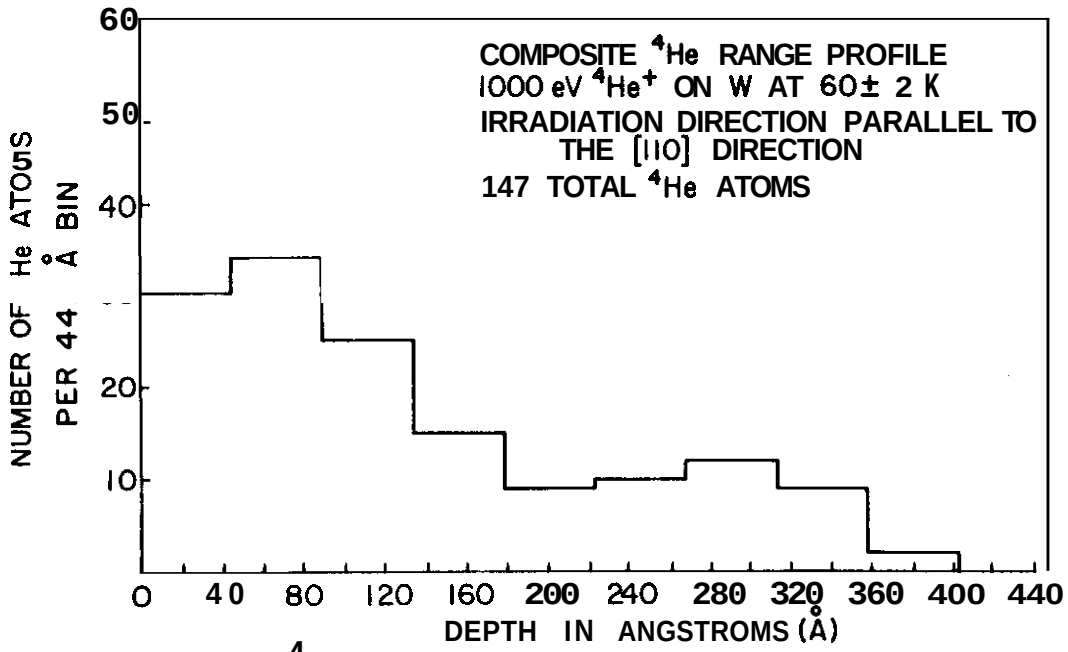

Figure 6. A composite ^{4}He range profile for all the 1000-eV implantations at 60K. A total of 147 ^{4}He events were recorded in the construction of this range profile.

Figure 7 exhibits $\bar{x}$ (in Å) versus the incident ion energy (in eV) for both the ^{3}He (solid black circles) and the ^{4}He (open circles) implantations. The total length of each error bar is two standard deviations in the mean (Δx_m), i.e., plus or minus one Δx_m. The quantity Δx_m is given by:

$$\Delta x_m = \Delta x/\sqrt{N} \ , \qquad (2)$$

where N was the total number of helium events detected at a particular incident ion energy for the composite profile. Figure 7 clearly shows that the quantity Δx_m was negligibly small when N exceeded 50 events. The smallest sample size was for the 100 eV ^{4}He implantation where N was equal to 21 events. In this case Δx_m was 3.5 Å and the fractional standard error ($\Delta x_m/\bar{x}$) was ~0.19. This was the only data point that laid slightly below the smooth line that passed through all the other data points for the ^{4}He implantations.

The results presented in fig. 7 show that $\bar{x}$ for both ^{3}He and ^{4}He increased monotonically, although not linearly, with increasing incident helium ion energy. Overall, for both ^{3}He and ^{4}He, the value of $\bar{x}$ increased from 18.7 to 194.9 Å as the incident ion energy was increased from 100 to 1500 eV. For an incident helium ion energy of less than 600 eV the $\bar{x}$'s for ^{3}He were greater than the $\bar{x}$'s for ^{4}He; this indicated that ^{3}He penetrated more deeply into the lattice, on the average, than ^{4}He. This is the result expected for a lighter species implanted in an amorphous solid. At incident helium ion energies greater than 600 eV the $\bar{x}$'s for ^{4}He exceeded the $\bar{x}$'s for ^{3}He. A detailed discussion of these effects is given elsewhere (Amano, Wagner and Seidman[72]).

Figure 8 displays Δx as a function of the incident helium ion energy for both ^{3}He and ^{4}He; Δx is very commonly known as the straggling, since it determines the width of the range profile. The length of each error bar in fig. 8 is equal to two universe standard deviations in the sample standard deviation (Δx_s), i.e., plus or minus one Δx_s. The quantity Δx_s, for a normal distribution, is given by (Parratt[71])

$$\Delta x_s = \Delta x/\sqrt{2N} \ . \qquad (3)$$

We have used eqn. (3) to obtain approximate values of Δx_s for our range pro-

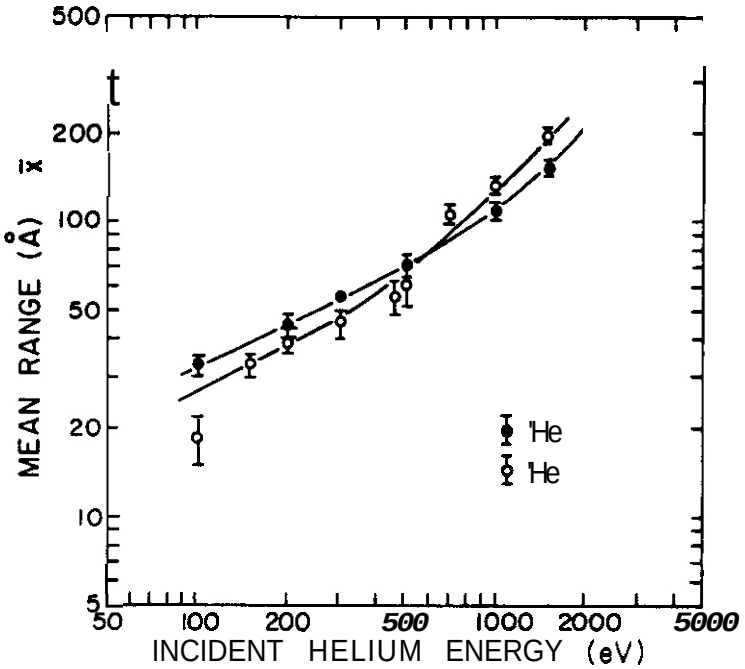

Figure 7. Mean range ($\bar{x}$) in angstroms versus incident helium energy (eV) for all the 3He and 4He implantations in tungsten at 60K.

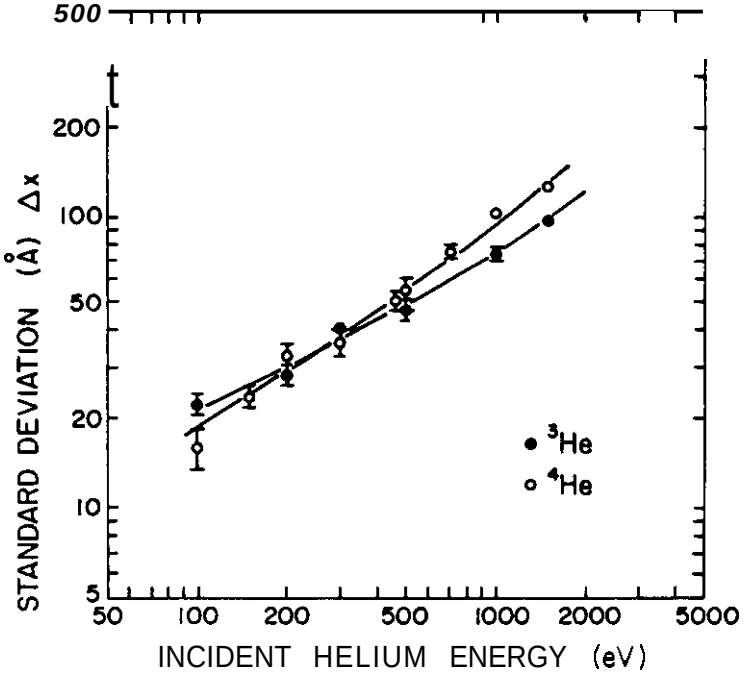

Figure 8. Standard diviation or straggling in angstroms (Ax) versus incident helium energy (eV) for all the 3He and 4He implantations in tungsten at 60K.

files which are actually skewed from a normal distribution. It is seen from fig. 8 that for the sample sizes we employed the values of Δx_s were all rather small.

For both ^{3}He and ^{4}He the value of Δx increased monotonically, although not linearly, with increasing incident helium ion energy (see fig. 8). The quantity Δx ranged from 16 to 124 Å as the incident helium ion energy was increased from 100 to 1500 eV. At an incident helium ion energy of ~300 eV the two curves crossed one another and the Δx's for ^{4}He were greater than those for ^{3}He. This indicated that as the incident ion energy was increased the ^{4}He was distributed in space, both wider and deeper than ^{3}He.

Figure 9 exhibits the relative variance $[(\Delta x)^2/(\bar{x})^2]$, of the ^{3}He and ^{4}He range profiles, as a function of the incident helium ion energy (in eV). Within the scatter of the data the quantity $(\Delta x)^2/(\bar{x})^2$ for ^{3}He exhibited a constant value of ~0.47 and the same quantity for ^{4}He was ~0.61. Thus in the energy range 100 to 15000 eV the value of $(\Delta x)^2/(\bar{x})^2$ for ^{4}He was greater than for ^{3}He. This clearly indicated that the ^{4}He was distributed more broadly in space than was ^{3}He.

C. Detection of Possible Radiation Damage in the Case of the 300 eV Helium Implantations

In order to establish that the ^{4}He detected in the case of the 300 eV implantation experiment was not trapped at structural defects in the W lattice, the following isochronal recovery experiment was performed. A W specimen was irradiated along the [110] direction with 300-eV $^4He^+$ ions at ~30 K. After the irradiation ≈2(110) planes, corresponding to 24.48 Å of material, were pulse field evaporated from the specimen. This procedure removed the sputtered surface and restored the surface to a nearly perfect state. The specimen was then warmed isochronally from ≈30 to 90 K at a rate of 1.5 K min^{-1}, while the FIM image was photographed at a rate of two 35-mm cine frames sec^{-1}. No SIA contrast effects were observed during this experiment indicating that no SIA's crossed the surface of the FIM specimen. Our previous work[73] demonstrated that if SIA's were present they would have appeared throughout the entire range of 38 to 90 K. The specimen was then dissected by the pulse field-evaporation technique and was examined for point defects. The density of point defects was determined to be $<8\times10^{-4}$ (atomic

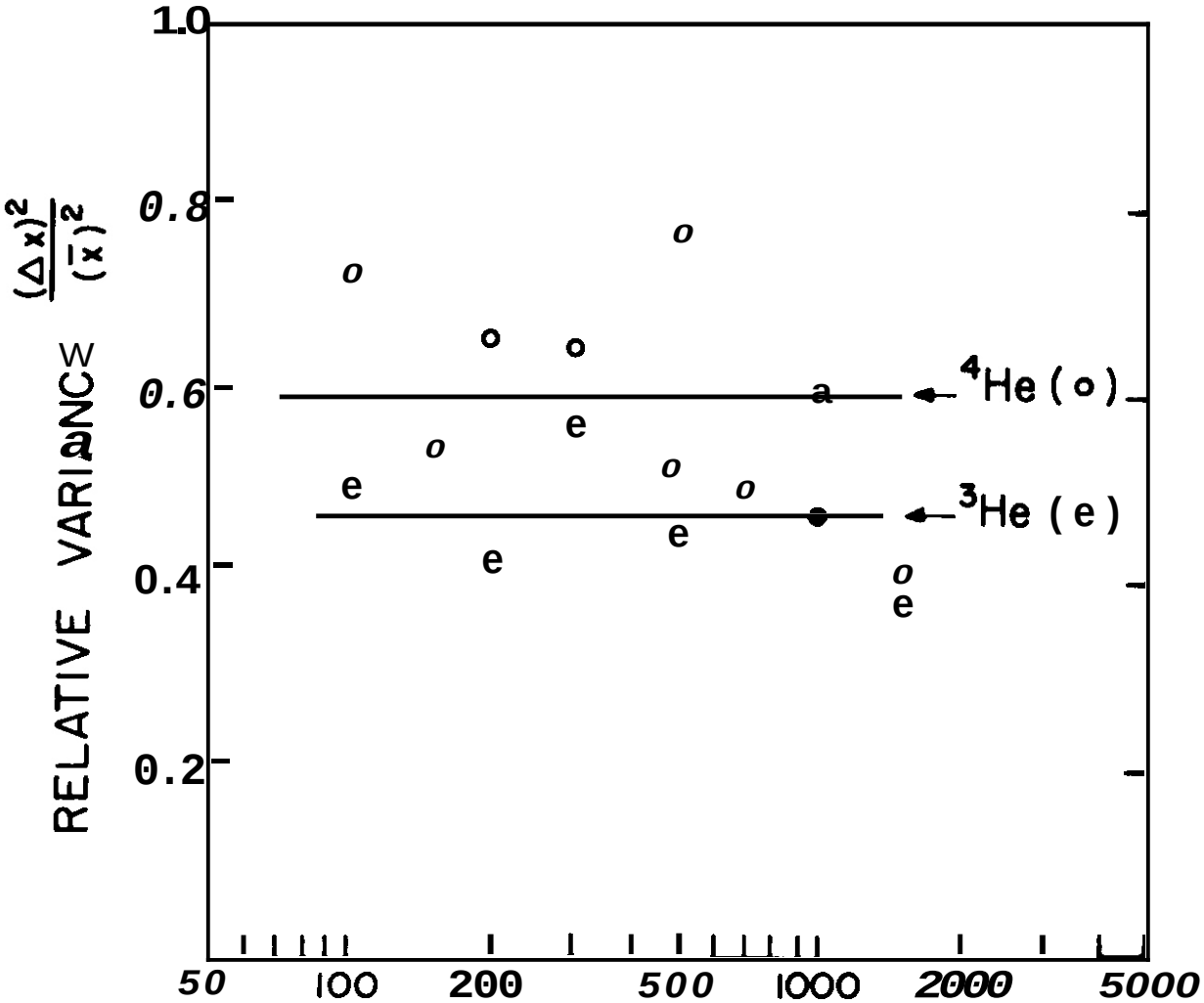

Figure 9. The relative variance $[(\Delta x)^2/(\bar{x})^2]$ versus the incident helium energy (eV) for all the ^{3}He and ^{4}He implantations in tungsten at 60 K.

fraction); their depth distribution was not related to the ^4He integral profiles. These results constitute conclusive evidence that the ^4He was not trapped at SIA's or vacancies. This indicated that the ^4He atoms were located in the interstices of the lattice and that they were immobile in tungsten at 60.

D. The Oiffusivities of ^3He and ^4He in Tungsten

The temperature at which the interstitial ^4He atoms became mobile in W was determined by implanting ^4He in an FIM specimen at different T_i's and then analyzing at T_r=60 K. The ^4He integral profile determined at T_r was independent of T_i only if the ^4He was immobile at all values of T_i. However, when T_i was above the temperature at which the ^4He interstitials became mobile, the ^4He implanted during the irradiation diffused to the surface of the FIM specimen and entered the gas phase. Therefore a sharp decrease in the measured ^4He concentration was expected as T_i was increased (see fig. 1). Since only T_i was varied, significant changes in the integral profile could only be attributed to a sharp increase in the mobility of the interstitial ^4He atoms at T_i. A dramatic change in the integral profile was observed upon increasing T_i from 90 to 110 K; thus indicating that interstitial ^4He atoms were immobile at 90 K but were highly mobile at 110 K. By employing a diffusion model, a value of the enthalpy change of migration ($\Delta h^m_{^4He}$) of 0.24 to 0.32 eV was estimated. The upper and lower limits on $\Delta h^m_{^4He}$ were determined by the values of the pre-exponential factor (D_o) chosen for the calculation of this quantity; the lower limit was determined by a D_o of $1x10^{-3}$ cm^2sec^{-1} and the upper limit by a D_o of $1x10^{-2}cm^2sec^{-1}$.

The diffusivity of ^3He in tungsten was determined by actually following the isothermal recovery of 300 eV implantation profiles which had been implanted at 90, 95, 98, 100 and 110 K. The diffusion equation was solved with appropriate initial and boundary conditions, to describe the diffusion of ^3He out of an FIM tip under isothermal conditions. The fit of the experimental isothermal recovery data to the solution of the diffusion equation yielded the diffusivity of ^3He as a function of temperature. The results of this work are shown in fig. 10. It is seen that the data is best described by the expression

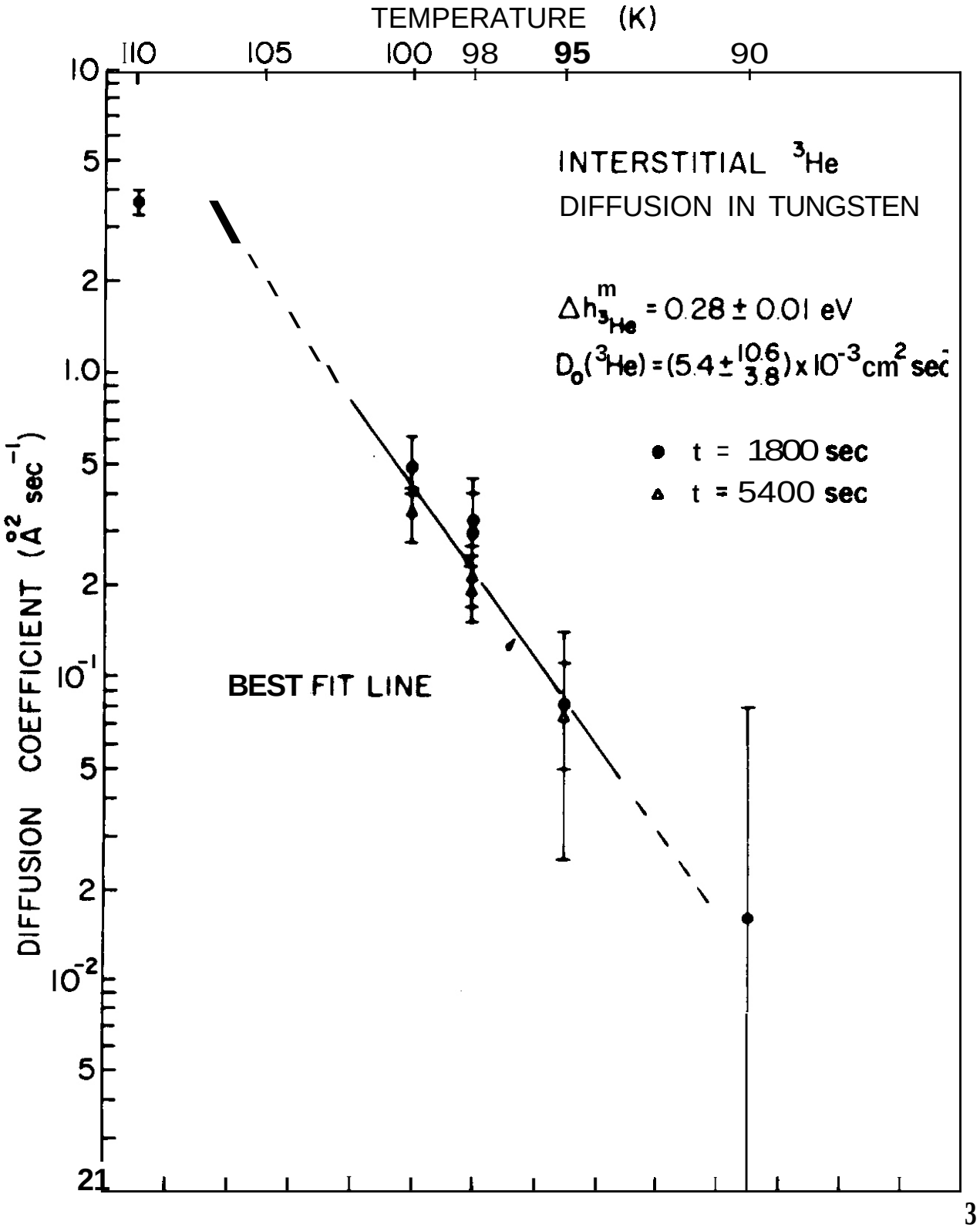

Figure 10. The diffusion coefficient of ^{3}He versus (1/T) in the temperature range 90 to 110 K. The times indicated correspond to different recovery times at each temperature.

$$D(^3He) = (5.4 \begin{smallmatrix} +10.6 \\ -3.8 \end{smallmatrix}) \times 10^{-3} \exp\left[\frac{-0.28 \pm 0.01 \text{ eV}}{kT}\right] \text{cm}^2\text{sec}^{-1}$$

Thus within the measured experimental uncertainties the Ah's for ^3He and ^4He in tungsten are identical. For further details on ^3He in tungsten see Amano and Seidman.[50]

ACKNOWLEDGEMENTS

This work was supported by the U. S. Department of Energy. Additional supported was received from the National Science Foundation through the use of the technical facilities of the Materials Science Center at Cornel1 University. I wish to thank my co-workers Drs. J. Amano and A. Wagner for permission to present results (see 54) in advance of more formal publication.

REFERENCES

1. E. W. Muller, Z. Physik 131, 136 (1951).

2. E. W. Muller, J. A. Panitz and S. B. McLane, Rev. Sci. Instrum. 39, 83 (1968).

3. P. J. Turner, P. Cartwright, M. J. Southon, A. van Oostrom and B. W. Manley, J. Sci. Instrum. 2, 731 (1969).

4. S. S. Brenner and J. T. McKinney, Surface Sci. 23, 88 (1970).

5. E. W. Muller and T. T. Tsong, Field-Ion Microscopy (American Elsevier, New York, 1969), Chapt. II.

6. E. W. Muller and T. T. Tsong, Field-Ion Microscopy (American Elsevier, New York, 1969), Chapt. III.

7. R. M. Scanlan, D. L. Styris, D. N. Seidman and D. G. Ast, Cornel1 Materials Science Center Report No. 1159 (1969).

8. W. P. Poschenrieder, Int. J. Mass Spectrom. and Ion Phys. 9, 357 (1972).

9. E. W. Muller and S. V. Krishnaswamy, Rev. Sci. Instrum. 45, 1053 (1974).

10. R. Gomer, Field Emission and Field-Ionization (Harvard University Press, Cambridge, Massachusetts, 1961).

11. Field-Ion Microscopy, edited by J. J. Hren and S. Ranganathan Plenum Press, New York, 1968).

12. Applications of Field-Ion Microscopy, edited by R. F. Hochman, E. W. Muller and B. Ralph (Advanced Research Projects Agency, AROA order No. 878 and the Georgia Institute of Technology, 1969).

13. K. M. Bowkett and D. A. Smith, Field-Ion Microscopy (American Elsevier, New York, 1970).

14. Field-Ion, Field Emission Microscopy and Related Topics, special issue of Surface Science 23, 1 (1970).

15. E. W. Muller and T. T. Tsong, in Program in Surface Science, edited by S. G. Davison (Pergamon Press, Oxford, 1973), Vol. 4, Part I, pp. 1-139.

16. J. A. Panitz, in Progress in Surface Science, edited by S. G. Davison (Pergamon Press, Oxford, 1978). Vol. 8, pp. 219-62.

17. Proceedings of the Int. Symp. on Application of FIM to Metallurgy, edited by R. R. Hasiguti, Y. Yashiro and N. Igata (Dept. of Metallurgy and Materials Science, Univ. of Tokyo, Tokyo, Japan, 1977).

18. D. N. Seidman, J. Phys. F: Metal Phys. 3, 393 (1973).

19. D. N. Seidman, K. L. Wilson and C. H. Nielsen, in Proceedings of the Int. Conf. on Fundamental Aspects of Radiation Damage in Metals, edited by M. T. Robinson and F. W. Young, Jr. (National Technical Information Service, U. S. Dept. of Commerce, Springfield, Virginia, 1975), pp. 373-96.

20. D. N. Seidman, in Radiation Damage in Metals, edited by N. L. Peterson and S. D. Harkness (American Society for Metals, Metals Park, Ohio, 1976), pp. 28-57.

21. D. N. Seidman, Surface Sci. 70, 532 (1978).

22. A. Wagner, T. M. Hall and D. N. Seidman, Rev. Sci. Instrum. 46, 1032 (1975).

23. T. M. Hall, A. Wagner, A. S. Berger and D. N. Seidman, Cornel1 Materials Science Center Report No. 2357 (1975).

24. T. M. Hall, A. Wagner, A. S. Berger and D. N. Seidman, Scripta Met. 10, 485 (1976).

25. T. M. Hall, A. Wagner and D. N. Seidman, J. Phys. E: Sci. Instrum. 10, 884 (1977).

26. A. Wagner, T. M. Hall and D. N. Seidman, J. Nuc. Mat. 69 & 70, 532 (1978).

27. R. M. Scanlan, D. L. Styris and D. N. Seidman, Phil. Mag. 23, 1439 (1971).

28. R. M. Scanlan, D. L. Styris and D. N. Seidman, Phil. Mag. 23, 1459 (1971).

29. P. Pétroff and D. N. Seidman, Appl. Phys. Lett. 18, 518 (1971).

30. D. N. Seidman and K. H. Lie, Acta Met. 20, 1045 (1972).

31. P. Pétroff and D. N. Seidman, Acta Met. 21, 323 (1973).

32. J. T. Robertson, K. L. Wilson and D. N. Seidman, Phil. Mag. 27, 1417 (1973).

33. D. N. Seidman, K. L. Wilson and C. H. Nielsen, Phys. Rev. Lett. 35, 1041 (1975).

34. K. L. Wilson and D. N. Seidman, Rad. Effects 33, 149 (1977)

35. D. N. Seidman, Scripta Met. 13, 251 (1979).

36. K. L. Wilson, M. I. Baskes and D. N. Seidman, Cornell Materials Science Center Report #4055 (1979); submitted to Acta Metallurgica for publication.

37. C. H. Nielsen, M. S. Thesis, Cornell University (1977).

38. J. Aidelberg, Ph.D. Thesis (in preparation), Cornell University (1979).

39. C-Y. Wei and D. N. Seidman, Rad. Effects 32, 229 (1977).

40. C-Y. Wei and D. N. Seidman, J. Nuc. Mat. 69 & 70, 693 (1978).

41. K. L. Wilson and D. N. Seidman, Rad. Effects 27, 67 (1975).

42. A. S. Berger, D. N. Seidman and R. W. Balluffi, Acta Met. 21, 123 (1973).

43. A. S. Berger, D. N. Seidman and R. W. Balluffi, Acta Met. 21, 323 (1973).

44. J. Y. Park, H-C. W. Huang, A. S. Berger, and R. W. Balluffi, in Defects and Defect Clusters in B.C.C. Metals and Their Alloys, edited by R. J. Arsenault (University of Maryland, College Park, MD, 1973), Nuclear Metallurgy, Vol. 18, pp. 420-439.

45. J. Y. Park, Ph.D. Thesis, Cornell University (1975).

46. H-C. W. Huang, Ph.D. Thesis, Cornell University (1975).

47. A. Wagner and D. N. Seidman, Phys. Rev. Letts. 42, 515 (1979).

48. A. Wagner, Ph.D. Thesis, Cornell University (1978).

49. D. N. Seidman, Department of Energy Report #COO-3158-77 (1979).

50. J. Amano and D. N. Seidman, to be published. (1979).

51. A. Macrander and D. N. Seidman, unpublished work (1979).

52. M. Yamamoto and D. N. Seidman, work in progress (1979).

53. L. A. Beavan, R. M. Scanlan and D. N. Seidman, Acta Metallurgica 19, 1339 (1971).

54. K. L. Wilson and D. N. Seidman, in Defects and Defect Clusters in B.C.C. Metals and Their Alloys, edited by R. J. Arsenault (University

54. of Maryland, College Park, MD, 1973), Nuclear Metallurgy, Vol. 18, pp. 420-439.

55. C.-Y. Wei and D. N. Seidman, Phil. Mag. A, 37, 257 (1978).

56. C.-Y. Wei, Ph.D. Thesis, Cornell University (1978).

57. M. I. Current and D. N. Seidman, to be published (1979).

58. S. S. Brenner and D. N. Seidman, Rad. Effects 24, 73 (1975).

59. S. S. Brenner, R. Wagner, J. Spitznagel, Met. Trans. A, 9A, 1761 (1978).

60. A. Wagner and D. N. Seidman, Cornell Materials Science Center Report #4007 (1978); to appear in J. Nuc. Mat. (1979).

61. C.-Y. Wei and D. N. Seidman, Cornell Materials Science Center, Report #4088 (1979).

62. Radiation-Induced Voids in Metals, edited by J. W. Corbett and L. C. Ianniello (National Technical Information Service, Springfield, Va., 1972).

63. See, for example, J. Nuc. Mater. 53 (1974), 76 (1978), and 77 (1978).

64. W. D. Wilson and C. L. Bisson, Radiat. Effects 22, 63 (1974).

65. O. S. Oen and M. T. Robinson, Nuc. Instrum. Methods 132, 647 (1976).

66. D. J. Reed, Radiat. Effects 31, 129 (1977).

67. B. Terreault, R. G. St-Jacques, G. Veilleaux, J. G. Martel, J. L'Ecuger, C. Brassard, and C. Cardinal, Can. J. Phys. 56, 235 (1978).

68. E. V. Kornelsen, Radiat. Effects 13, 227 (1972).

69. F. Maury, M. Biget, P. Vajda, A. Lucasson, P. Lucusson, Radiat. Effects 38, 53 (1978).

70. J. P. Biersack and L. D. Haggmark, submitted to Nuc. Instrum. Methods (1979).

71. L. G. Parratt, Probability and Experimental Errors in Science (John Wiley, New York, 1961), Chapt. 2.

72. J. Amano, A. Wagner and D. N. Seidman, Cornell Materials Science Center Report #4108 (1979).

73. R. M. Scanlan, D. L. Styris, and D. N. Seidman, Philos. Mag. 23, 1439 (1971); K. L. Wilson and D. N. Seidman, Radiation Effects 27, 67 (1975); D. N. Seidman, K. L. Wilson, and C. H. Nielsen, Phys. Rev. Lett. 35, 1041 (1975).

QUANTITATIVE DATA EXTRACTION FROM TRANSMISSION ELECTRON MICROGRAPHS

J. A. Sprague
Naval Research Laboratory

I. INTRODUCTION

Transmission electron microscopy (TEM) is widely recognized as a powerful tool for examining the effects of radiation on materials. Many of the radiation-induced defects, such as dislocation loops, voids, and precipitates, that produce significant changes in the behavior of engineering materials also produce characteristic electron diffraction and/or diffraction contrast effects that allow them to be identified and well characterized by TEM of thin foils. In many applications, such as comparison of experimental observations with theoretical predictions of damage evolution, the electron microscopist is called upon to provide quantitative data, such as size distributions, number densities, and spatial distributions, for the observed defects. This process, typically carried out by human counting and measurement of individual defect images with either manual or computer-aided recording of the results, is extremely tedious, time-consuming, and expensive. The benefits of successful automation of these measurement procedures would be very great in terms of the amount and quality of the information that could reasonably be generated. The aims of this paper are to examine some state-of-the-art image analysis methods in relation to the special problems presented by TEM of defects in solids, and to indicate areas in which additional development can provide useful advances in quantitative TEM data extraction. The discussion will cover an overview of quantitative TEM, the digital image analysis process, coherent optical processing, and finally a summary of the author's views on potentially useful advances in TEM image processing.

11. TEM DEFECT ANALYSIS

The study of defect clusters by TEM can be divided into three types of measurements: (1) defect identity and character; (2) defect size distribution; and (3) defect number density and spatial distribution. The last two of these

measurement types are potentially the most amenable to automated analysis. The determination of the size distribution of a set of defects requires the measurement of the distance(s) between equivalent points on each image to obtain a size or sizes that can be related to a characteristic dimension or dimensions of the physical defect. Images are therefore required with predictable relationships to the defects producing them, and with sufficiently localized (sharp) contrast to allow accurate measurement. For determination of number density and spatial distribution, a second micrograph must be added, to form a stereo pair, with the specimen tilted between the two pictures. It is preferable that the defect contrast be identical in the two micrographs for defects and surface features, specimen thickness (and therefore volume) and the 3-dimensional spatial distribution of the defects can be determined.

After the experimenter has obtained suitable micrographs for quantitative analysis, some method must be found to extract the information from them. An appealing solution would be to use the micrographs themselves as input to a computer. The computer would then be suitably programmed to recognize the defect images, measure their dimensions, and determine their positions. The potential of this approach, as well as that of coherent optical analysis, will be discussed in the following sections.

III. DIGITAL DATA EXTRACTION

In discussing the possibilities of computerized defect analysis, it is useful first to look at the reliability of human micrograph interpretation and measurement. As a part of the BCC Ion Correlation Experiment (1), void distributions were measured by 8 laboratories on identical copies of a common micrograph of ion-irradiated molybdenum. The mean diameters determined by the various experimenters varied by ±4 % around the average. The number density varied from +10 % to -15 % around the average. This latter spread was especially interesting, since the same specimen thickness was assumed by each laboratory. This means that among experienced microscopists working on a good, sharply-focused picture, there was a significant difference in interpretation of what was and what was not a void. This variability needs to be considered in evaluating the performance of any digital system.

In any digital image scheme, the initial, and most basic, feature is the conversion of the image to digital form. This is done by converting the image to "pixels." The image area is divided into N lines, each of which is divided into n elements, or pixels. Each pixel is assigned a number representing its gray level, which is stored as a byte, or portion of a digital word. Depending on the precision of gray level desired, each byte could be any number of binary bits long. The most common leiigths are 5 bits (32 levels), 6 bits (64 levels), and 8 bits (256 levels). Common divisions for an image are 512 x 512 elements and 1024 x 1024 elements. This implies a large amount of data transmission and storage, since a 512 x 512 image at 64 gray level resolution consists of over 1.5 x 10^6 bits of data. In a photographic image, on the other hand, the information is stored at a higher spatial resolution (emulsion grains) with fewer gray levels for each element. If we consider a simplified case, with 1 micron grains, each of which is totally black or totally white, then a 70 mm square negative would contain approximately 5 x 10^9 individual bits. As discussed by Farnell and Flint (2), the situation is somewhat more complicated in the case of electron micrographs, since the effective "grain size" is induced by local fluctuations in electron exposure, but the basic difference in information organization remains, and must be considered in designing or evaluating micrograph analysis methods.

To successfully analyze an electron micrograph, a system must be able to perform four basic functions. It must detect the features of interest; it must accurately detect the edges of these features to measure their sizes; it must compensate for the overlap of image features; and, finally, it must reject artifacts. The detection of specific image features, known as "segmentation," divides the image into regions, such as void and non-void areas. . This is commonly done by "thresholding," a good example of which would be the detection of large (and thus dark) carbide precipitates in a micrograph lacking other contrast. All regions darker than some reference value would be detected as belonging to the carbide particles. Differential thresholding can also be used, so that an image feature is detected by finding regions that are surrounded by rapid changes in gray level. This is similar to the way the human eye detects images of small voids, by

the dark or light rings around them. Differential thresholding requires more computation than simple thresholding, but it can provide better detection and size measurement on the types of images of interest in TEM. Another important consideration in both detection and size measurement is the spatial resolution of the digital image in relation to the sizes of the features being detected. In many cases, this limiting feature may be considerably smaller than the defect itself, as with rings surrounding voids. Possibly the most troublesome area for TEM analysis is image overlap. If an overlap can be detected by eye and the image characteristic that indicates an overlap can be accurately described, it should be possible to digitally detect it and compensate for it. However, generalized routines for this purpose do not exist at present, so some software development would probably be required for each general type or shape of image encountered. All of the above considerations point to the need for a flexible interactive image analysis sytem.

The available hardware for digital image processing and analysis can be roughly divided into two categories, commercially packaged image analyzers and advanced experimental processing and analysis systems. Both kinds of systems operatre on the same principles, but the main differences are that the advanced systems tend to have provisions for storing multiple images on magnetic disks, more powerful central processors, and more sophisticated software for processing images. The principal advantage of these capabilities is that once an image has been read onto a disk file, it can be processed to enhance the features of interest and stored on another file before being analyzed by other parts of the software. This is particularly valuable when new kinds of images are encountered, since several image transformations can be tested to determine which produces the most readily analyzable final image. The cost of such an advanced system is considerable, roughly equivalent to a top-grade analytical electron microscope, but its flexibility could allow it to be shared by several groups within a university or major 1aboratory.

IV. COHERENT OPTICAL PROCESSING AND ANALYSIS

Another class of image processing and analysis equipment makes use

of coherent laser light and the Fourier transforming properties of lenses to analyze the spatial frequencies of images. These systems, which are well described in several texts, such as the one by Goodman (3), will not be treated in any detail here, but they do deserve some further investigation as potential tools for micrograph analysis. In a simple system, light of an expanded and collimated laser beam is passed through a transparency of the input image. A lens is then used to form the optical Fourier transform of the input image in its back focal plane. This transform, which represents the two dimensional spatial frequency distribution of the image, can then be recorded and analyzed. A fairly familar use of this type of information (although not necessarily from this type of system) is the determination of lattice fringe spacings by optical diffraction (4). The possibilities of other types of data extraction from micrographs by optical Fourier analysis should be further examined, particularly using the digital image processor to acquire the spatial frequency distributions.

Other experimental optical/digital image analyzers that are potentially useful for TEM are the interferometric optical stereo correlators, discussed by Balasubramanian (5). These rather complex instruments automatically calculate parallax distributions from stereo pairs of pictures. The proper reduction of this type of data could produce complete 3-dimensional defect size and distribution data, and directly solve the overlap problem. This type of equipment is still in the development stage, but the microscopy community should remain aware of advances in this field.

V. GENERAL OUTLOOK

In summary, the automated analysis of defect images produced by TEM does appear feasible, but some additional development work will be required for its routine application. The currently available digital image processing hardware should be adequate for these applications, but a set of software specifically oriented to the problems of TEM images is needed. Coherent optical optical processing of electron micrographs needs more investigation, but may also be a valuable technique. Whatever data extraction methods, including human photo interpretation, are used, close interaction between experimenters is needed so that the most useful information is produced.

REFERENCES

1. J. L. Brimhall, "Summary Report of BCC Ion Correlation Experiment," in Proceedings of the Workshop on Correlation of Neutron and Charged Particle Damage, Oak Ridge National Laboratory, June 8-10, 1976, CONF - 760673, pp. 241-251.

2. G. C. Farnel! and R. B. Flint, "Exposure Level and Image Quality in Electron Micrographs, "Journal of Microscopy 3 (1975), pp. 319-332.

3. J. W. Goodman, Introduction to Fourier Optics, New York, McGraw - Hill (1963).

4. R. Gronsky, R. Sinclair. and G. Thomas. "Optical Microdiffraction in Lattice Image Analysis,; Proceedings of the Twenty Fourth Annual Meeting of EMSA, 1976, Claitor's Publishing Division, pp. 494-495.

5. N. Blasubramanian, "Optical Processing in Photogrammetry," in Optical Data Processing, D. Casasent, ed., New York, Springer-Verlag (1978), pp. 119-149.

HYPERFINE TECHNIQUES AND EXAFS: PROBES OF SPECIFIC ATOMIC ENVIRONMENTS

F. Y. Fradin
Materials Science Division
Argonne National Laboratory
Argonne, Illinois 60439

I. INTRODUCTION

In this lecture I will discuss two classes of experimental probes of specific atomic environments: I. hyperfine interactions and 11. extended x-ray absorption fine structure (EXAFS). The emphasis of my discussion will be on a description of the types of information on the near neighbor atomic environments of specific probe atoms that can be obtained with these techniques. Generally speaking, the information is of two types: static structural information about the numbers, kinds, and locations of nearest neighbor atoms and dynamic information regarding the motion of atoms, which may include localized atomic vibrations or atomic displacements due to diffusion or dislocation motion.

In the remaining sections, I will review only two of the many hyperfine techniques, specifically nuclear magnetic resonance (NMR) and Mossbauer effect (or nuclear gama-ray resonance [NGR]) and also the newly developed x-ray technique (EXAFS).

II. NUCLEAR MAGNETIC RESONANCE

The nuclear magnetic ressnance technique involves the resonant absorption of radio frequency magnetic energy by coupling to nuclear Zeeman levels split by a static applied magnetic field. There are many abundant isotopes in the periodic table that yield high sensitivity probes for NMR investigations. The perturbing interactions of the nucleus with its surroundings that yield interesting information include:

A. Nuclear dipole - nuclear dipole interaction

This interaction between magnetic dipoles can be calculated in a straight-forward manner from the known nuclear magnetic moments of the

constituent elements. The interaction results in a broadening of the resonance absorption 1ine characterized by a second mement, which for nonequivalent neighboring nuclei of moment μ_s is given by

$$\langle \Delta H^2 \rangle = \frac{1}{3} \mu_s^2 \, S(S+1) \, \frac{1}{N} \sum_{j,k} \frac{(1-3\cos^2 \theta_{jk}}{r_{jk}^6} \qquad (1)$$

where S is the spin of the nucleus of moment μ_s, N is the total number of nuclei, r_{jk} is the internuclear vector between the resonant nucleus j and its neighbor k, and θ_{jk} is the angle between r_{jk} and the applied magnetic field. The time dependent modulation of dipole - interaction by atomic diffusion processes, which can change r and 8, yields a contribution to the nuclear magnetic relaxation rate T_1^{-1}, i.e. the rate of attainment of the thermal equilibrium population of the Zeeman leads. For the case of aluminum the diffusion contribution $T_1)^{-1}_{dif}$, is illustrated in Fig. 1 where

$$\left.\frac{1}{T_1}\right)_{diff} \sim \gamma^2 \langle AH^2 \rangle \frac{\tau}{1+4\omega^2\tau^2} \qquad (2)$$

Here $\gamma = \mu_{A\ell}/\hbar$, τ is the diffusional jumptime, and $\hbar\omega$ is the energy quanta of the nuclear magnetic resonance absorption. Fig. 2 illustrates the diffusion coefficients for aluminum obtained by various techniques.

Weaver and Weaver and Beezhold have used nuclear magnetic relaxation to study the aging of titanium tritide and to study ^{3}He implantation in Pd thin films. In the former study, they were able to study the aging effects resulting in a variety of environments for ^{3}He from atomically dispersed to eventually large ^{3}He bubbles (see Figs. 3 and 4). In the latter study, $\sim 3 \times 10^{18}$ ^{3}He was implanted in $\sim 2\mu$ Pd foil. All of the ^{3}He appeared to be confined to very small clusters of $\sim$ 10A diameter (see Fig. 5).

B. Nuclear electric quadrupole interaction

The nuclear electric quadrupole interaction is the electrostatic

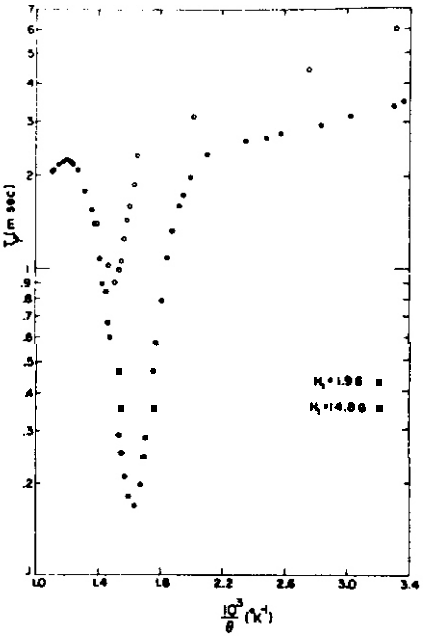

Figure 1. Spin lattice relaxation time $T_{1\rho}$ for ^{27}Al in the rotating frame vs. the reciprocal temperature. The electrical component T_e dominates below about 240°C and above 550°C after Fradin and Rowland.

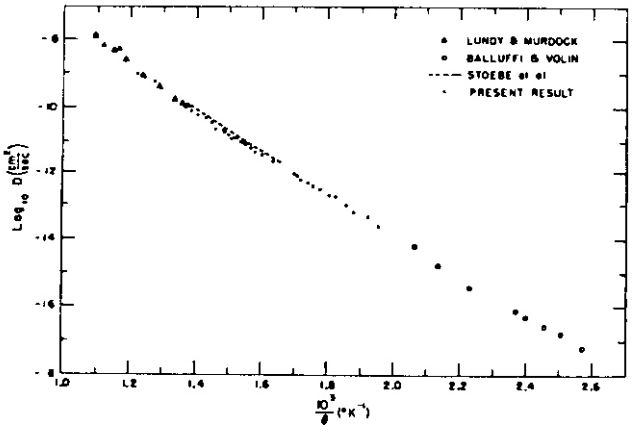

Figure 2. Results (Fig. 1) for the diffusion coefficient of Al, together with other determinations, plotted against reciprocal temperature. Values for D are best represented using D_o = **0.035 ± 0.015** cm^2/s, **Q** = 28.7 ± 0.8 kcal/mole after Fradin and Rowland.

Fig. 3

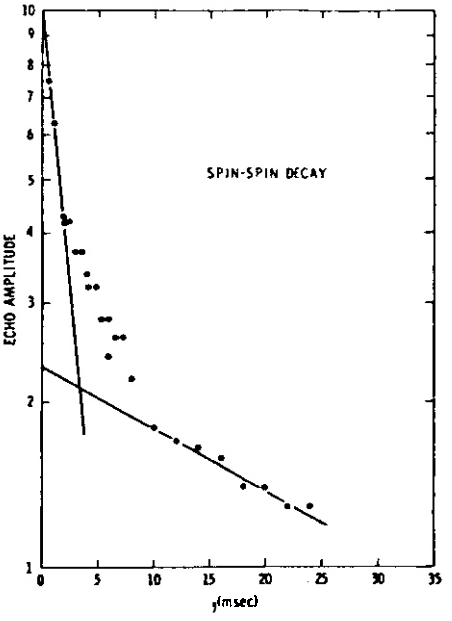

Fig. 4

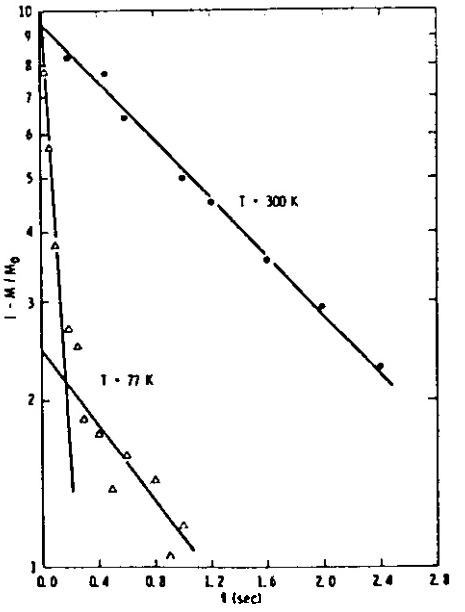

Figure 3. Transverse magnetization decay for ^{3}He contained in three-year-old $Ti^3H_{1.8}$ after Weaver. Multiple relaxation behavior due to a variety of environments for He.

Figure 4. Longitudinal magnetization recovery for ^{3}He contained in three-year-old $Ti^3H_{1.8}$ after Weaver. Most He in lattice exists as individual atoms or as < 10Å clusters; eventually He forms into bubbles with relaxation characteristics of bulk He.

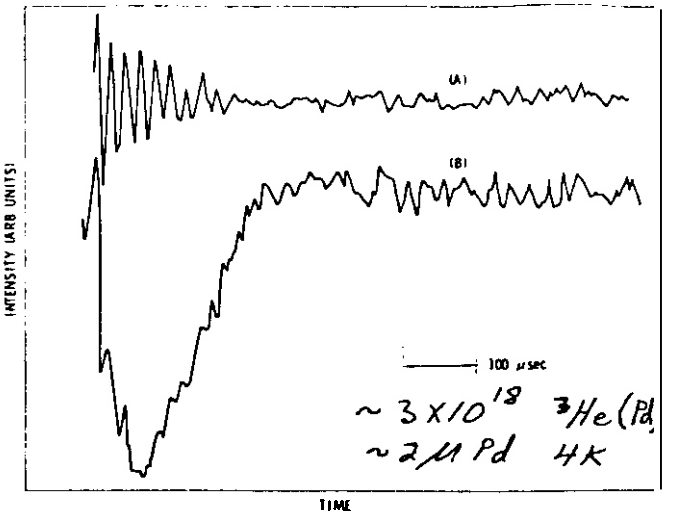

Figure 5. Free-induction decay for ^{3}He implanted into Pd. Two traces are for the spectrometer frequency set just off (A) and on (B) resonance after Weaver and Beezhold. All He found in $\lesssim$10Å clusters.

coupling between the quadrupole moment of the nucleus, i.e. for all nonspherical nuclei with $S > \frac{1}{2}$, and the electric field gradient (efg) of the environment. The interaction results in a splitting of the resonance line into a number of components due to a lifting of the Zeeman degeneracies. These quadruple split lines are very sensitive to changes in surrounding positions or type of aotms due to the attendant changes in the electric field gradient. This is illustrated in Figs. 6 and 7 for the ^{27}Al NMR in annealed and self-damaged $PuAl_2$, respectively. The time dependent modulation of the EFG, for example, by the motion of a dislocation, yields a nuclear magnetic relaxation effect similar to that from atomic diffusion. This effect is illustrated in Figs. 8 and 9.

III. MÖSSBAUER EFFECT

The Mössbauer effect technique involves the resonant emission and reabsorption of a gamma ray from nuclei in a standard sample and one in the environment under study. The gamma ray from the low lying nuclear excited state is typically of energy $\sim$ 14 KeV, and the source and absorber samples are brought in-io resonance by doppler shifting one or the other with a ' velocity drive. The resonance absorption line positions are perturbed by nuclear electric quadrupole interactions, as in NMR, by isomer shifts that are dependent upon the total electronic charge at the nucleus and by magnetic hyperfine interactions that are the analogs of chemical or Knight shifts in NMR and arise from coupling the nuclear spin to orbital and spin moments of electrons surrounding the resonant nucleus. In Fig. 10, the ^{57}Fe NGR of polycrystalline Al doped with 1.3 mCi ^{57}Co ($\lesssim$ 1 ppm Co) is shown. The satellite peaks on the high velocity side of the main peaks arise from these Fe nuclei that have trapped interstitials after irradiation to 2.3 x 10^{18} n/cm^2 at 4.6K.

In order for a nucleus to resonantly absorb a gamma ray, it must do so in a recoiless manner. That is, the momentum of the gamma-ray must be absorbed by the crystal as a whole not by the recoil of a single nucleus. The integrated intensity, therefore, is proportional to the recoiless fraction f, which for a harmonic solid is given by the Debye-

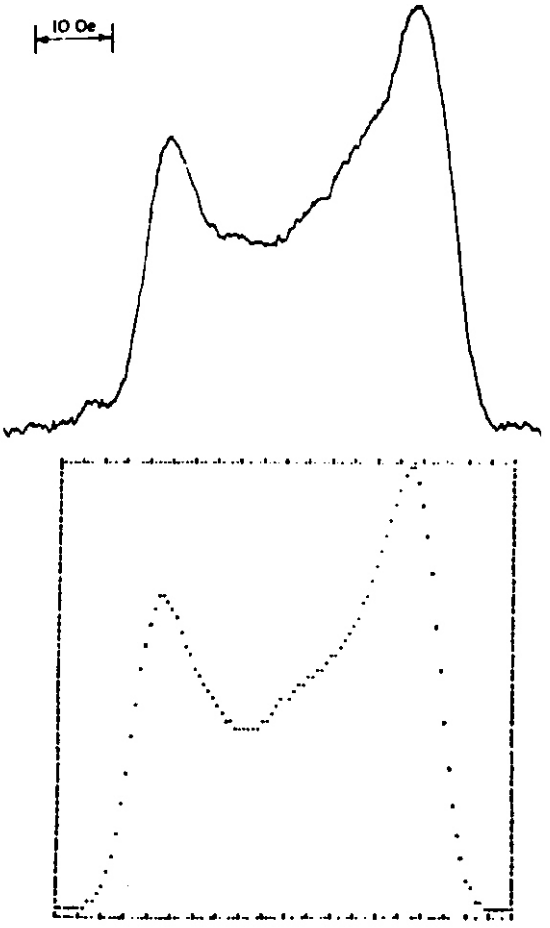

Figure 6. (Top) Experimental Fourier transform of ^{27}Al PNMR free induction decay of annealed $PuAl_2$ at 12 MHz and 77°K. Magnetic field increases to the right. (Bottom) Synthetic powder pattern obtained with $q_o = 0.73 \times 10^{24} cm^{-3}$. Major division on field axis is 4.0 Oe after Arko et al.

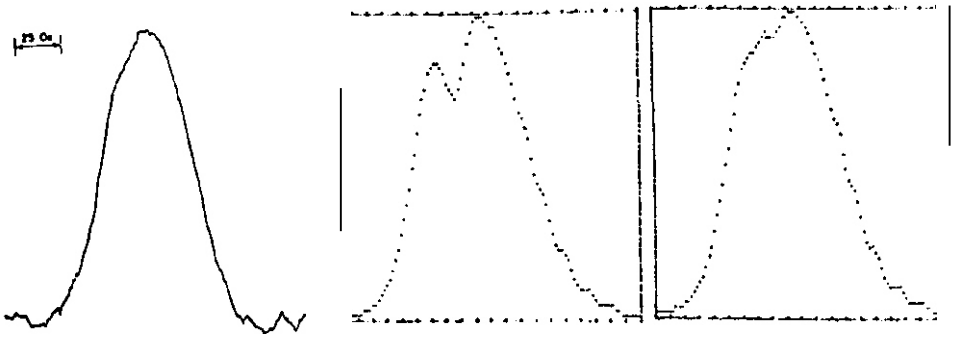

Figure 7. (Left) Experimental Fourier transform of ^{27}Al PNMR free induction decay of damaged $PuAl_2$. Experimental parameters identical to those in Fig. 6. Magnetic field increases to the right. (Middle) Synthetic power pattern obtained with $q_0=0.87\times10^{24}cm^{-3}$ and $\Delta q/q_0=0.5$. (Right) Same as (middle) but with an additional component with q=O and relative weight of 0.03. Major division on horizontal axis is 6.6 Œ after Arko et al.

Fig. 8

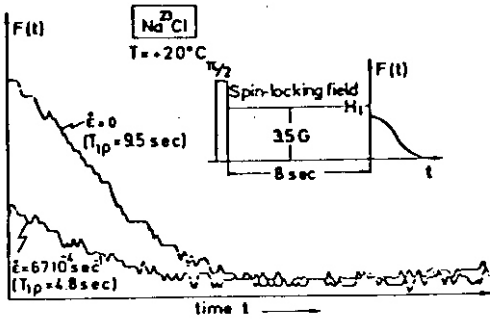

Fig. 9

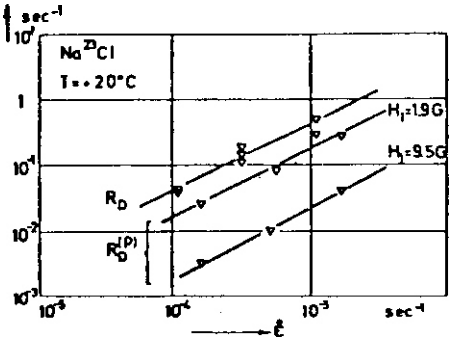

Figure 8. Showing two decay curves F(t) after the spin locking sequence (see insert), with zero and finite plastic deformation rates $\dot{\varepsilon}$. $T_{1\rho}$ is calculated from the expression: $S(\tau)=S(0)\exp(-\tau/T_{1\rho})$, with τ the duration of the locking pulse and S the maximum of F(t) after Hut, etal.

Figure 9. Comparison between Jeener (R_D) and spin locking ($R_D^{(\rho)}$) experiment, showing the proportionality between R_D and $R^{(\rho)}$, and $\dot{\varepsilon}$ after Hut, et al.

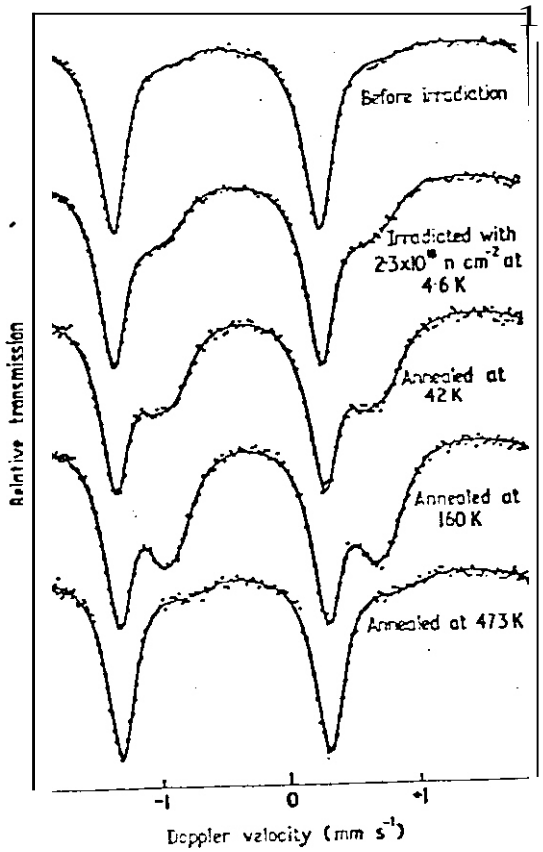

Figure 10. Characteristic Mossbauer spectra of $^{57}Co(^{57}Fe)$ in aluminum before and after fast neutron irradiation at 4·6K and after subsequent isochronal annealing. Source temperature during measurement 4·2K. The absorber is a 0.03 mm thick natural iron foil at 77 K which causes the magnetic splitting of the spectra. Only the two inner lines of the six line spectrum are measured after Vogl et al.

Waller formulation,

$$f \sim e^{-K^2 \langle X^2 \rangle} \tag{3}$$

where K *is* the wave number of the gamma ray and $\langle X^2 \rangle$ is the mean squared displacement of the absorbing nucleus. Figure 11 shows -an f vs. temperature for the unirradiated (open circles) and the irradiated (triangles) ^{57}Fe in aluminum of Fig. 10. The larger values of $\langle X^2 \rangle_{Fe}$ in the 'Fe-interstitial complexes result from a low frequency resonance mode.

Although there are only a few atoms in the periodic table that have useful Mossbauer isotopes, source experiments for appropriate isotopes have high sensitivity to defect environments.

IV. EXTENDED X-RAY ABSORPTION FINE STRUCTURE

The absorption of x-rays of energy E above an absorption edge, *e.g.* the K-edge, in a solid is given by

$$\mu_K(E) = \mu_o(E) \left[1 + \chi(E)\right] \tag{4}$$

where μ_o is the atomic absorption coefficient and $\chi(E)$ is the oscillatory component or EXAFS. (See Fig. 12). The probability for absorption of an x-ray depends on the dipole matrix element between the initial K-shell electron and the final electron state, which in a solid involves the scattering effects of an outgoing spherical wave off of neighboring atoms. These electron scattering effects off atoms at distances R_j from the absorbing atom yield interference effects given by

$$\chi(k) = \frac{\quad}{4\pi\hbar^2 k} \sum_j \frac{N_j}{R_j^2} t_j(k) e^{-2R_j/\lambda}$$

$$\sin\left[2kR_j + \theta_j(k)\right] e^{-2k^2\sigma_j^2} \tag{5}$$

where N_j is the number of atoms at R_j, t_j and θ_j are the backscattering

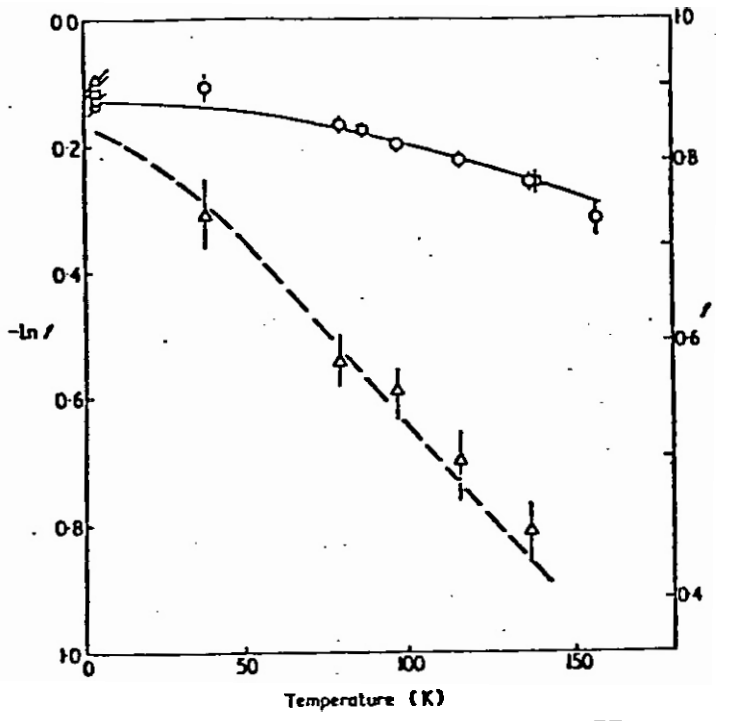

Figure 11. Logarithm of Debye-Waller factor of $^{57}Co(^{57}Fe)$ (< 1 ppm) in aluminum. 'Original line' in unirradiated sample; o 'Original line in irradiated sample; A 'Defect line' in irradiated sample. Full curve fit with Debye model (θ = 290 K); broken curve fit with two Einstein frequencies model (ω_{low} = 6.5 x $10^{12}s^{-1}$ weighted $\frac{1}{3}$, ω_{high} = 6 x $10^{13}s^{-1}$ weighted $\frac{2}{3}$). After Vogl et al.

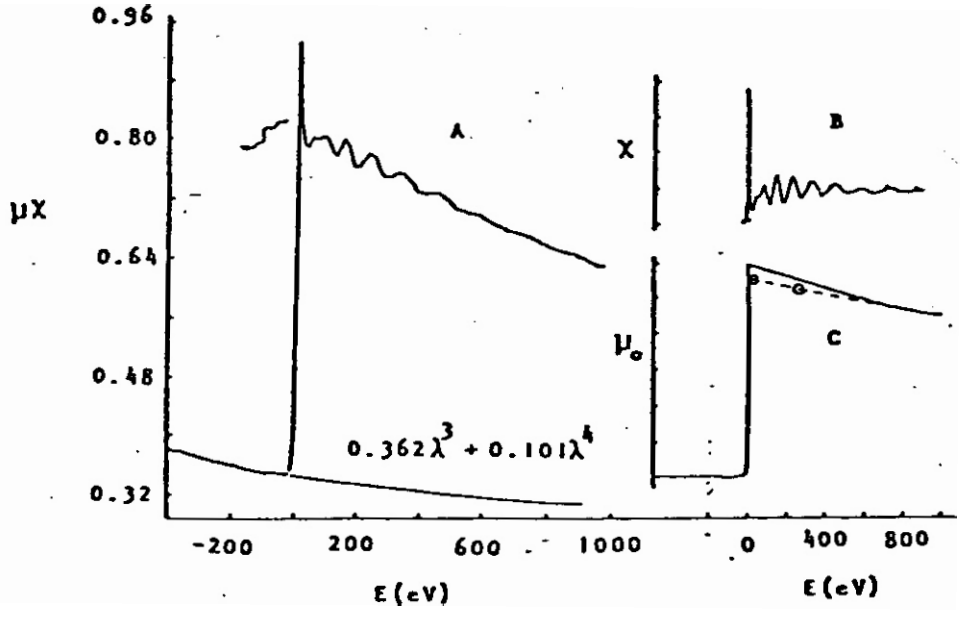

Figure 12. A. Absorption edge of Ge.
B. EXAFS after background subtraction.
C. Atomic absorption background after Lytle et al.

amplitude and phase shift of these atoms, λ is the elastic mean free path for the electrons, σ_j^2 is the mean squared relative displacement between the backscattering and absorbing atom, and k is the wave vector of the outgoing K-shell electron given by

$$\frac{\hbar^2 k^2}{2m} = E - E_K \tag{6}$$

where E_K is the energy of the absorption edge. As can be seen in Eq. (5), the EXAFS has sensitivity to the numbers, kinds, and distances to near neighbor atoms. Normally one looks at the radial distribution function of amplitude of the Fourier transform of the EXAFS. An example of Fe EXAFS in various silicate glasses is shown in Fig. 13.

Using a rotating anode source and fluorescence detection, one should be able to measure EXAFS on 2 x 10^{-6} Cu in Al, for example. Synchrotron sources should allow a couple of orders of magnitude more sensitivity when fully developed.

V. SUMMARY

The EXAFS technique yields direct structural information; the technique can be used with high sensitivity using rotating anode or synchrotron sources of x-ray and can be applied to all atoms heavier than carbon. A number of well developed hyperfine techniques such as NMR and NGR can yield unique information about the static and dynamic characteristics of specific atomic environments. However, these powerful atomic probes have still to be exploited for the study of radiation-induced defects in solids.

Because these probes are strongly affected by near-neighbor environments of specific probe atoms, they are highly suitable for determinations of the structure of small solute-vacancy or solute-interstitial complexes and vacancies or small vacancy clusters. The EXAFS technique gives direct structural information while that from hyperfine interactions must be deduced from models. An advantage of hyperfine techniques is their capability to be phase specific about the environment and numbers of probe nuclei.

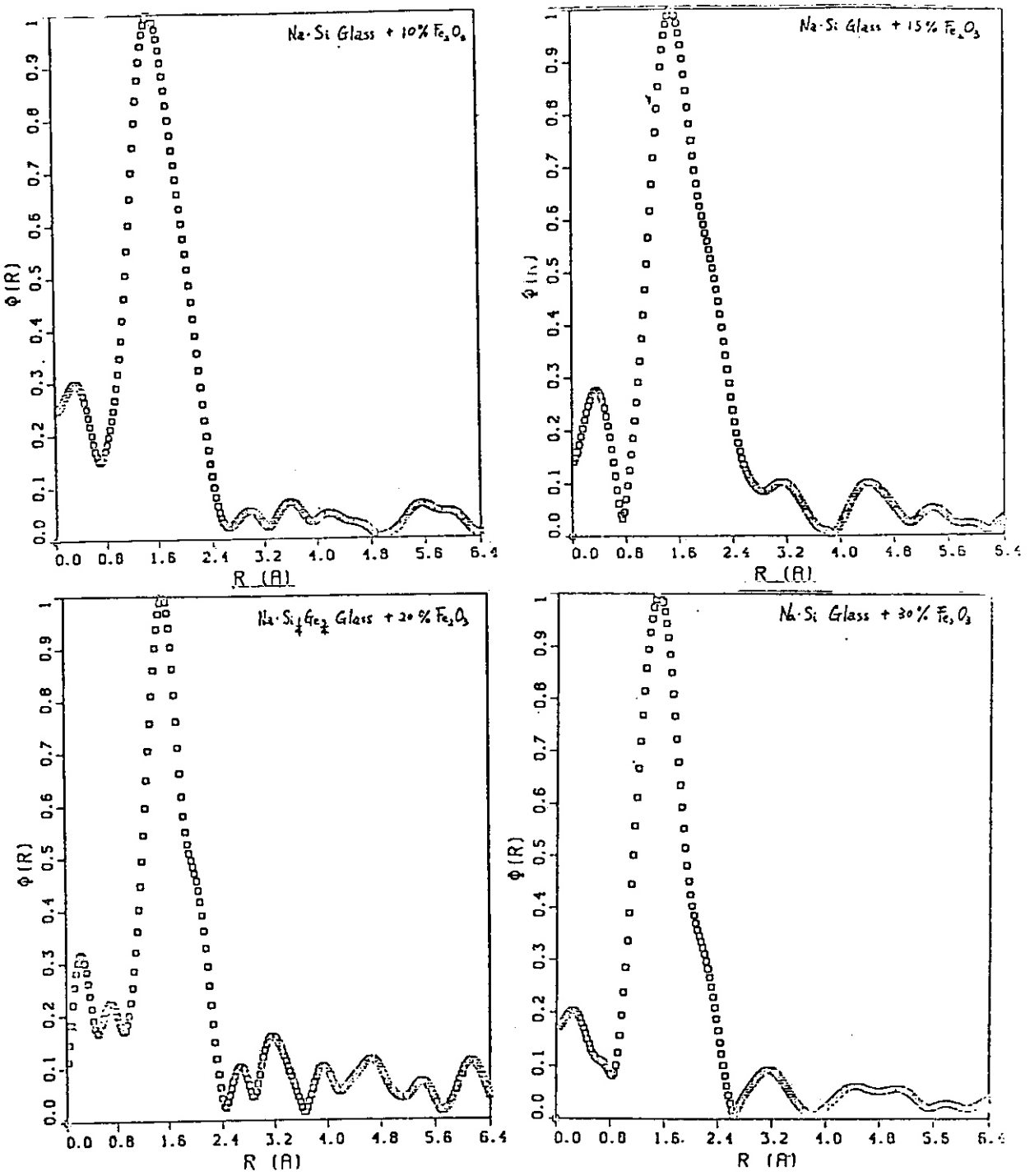

Figure 13. Fe K-edge EXAFS, amplitude of Fourier transform, for a number of doped Na-silicate glasses. Variation in structure between 1.2 and 2.0 A shows oxygen near neighbor environment about Fe (Ref. 4).

Furthermore, NMR techniques have been highly developed to determine the structure and diffusion properties of ^{1}H, ^{2}D, ^{3}He in materials. With regard to sample requirements, NMR and Mössbauer effect samples are normally $\lesssim 1$ gm of polycrystalline or single crystal material in powdered or foil form, EXAFS samples can be ~ 1 to 10 μm of any polycrystalline or single crystal material for absorption methods of detection or thin films for fluorescence or surface sensitive detection modes.

REFERENCES

1. A. J. Arko, F. Y. Fradin, and M. B. Brodsky, Phys. Rev. B **8**, 4104 (1973).

2. F. Y. Fradin and T. J. Rowland, Applied Phys. Letters, **11**, 207 (1967).

3. G. Hut, A. W. Sleeswyk, H. J. Hackelöer, H. Selback, and O. Kanert, Solid State Commun 17, 85 (1975).

4. G. S. Knapp and F. Y. Fradin "EXAFS Studies of Materials" in Electron and Positron Spectroscopies in Materials Science and Engineering, edited by O. Buck (Academic Press, Inc. 1979).

5. F. W. Lytle, D. E. Sayers, and E. A. Stern, Phys. Rev. B **11**, 4825, (1975).

6. G. Vogl, W. Mansel, and W. Vogl, J. Phys. F. **4**, 2321 (1974).

7. H. T. Weaver and W. Beezhold, Applied Phys. Letters, **24**, 522 (1974).

8. H. T. Weaver, Applied Phys. Letters **30**, 80 (1977).

SURFACE ANALYSIS TECHNIQUES

M. G. Lagally
Department of Metallurgical and Mineral Engineering
University of Wisconsin
Madison, Wisconsin 53706

I. INTRODUCTION

There are a present about fifty techniques that have been used for studying the properties of surfaces at the microscopic level, in addition to a number of others that measure macroscopic properties. Of the former, some are no more than laboratory curiosities, others have limited applicability to model systems in fundamental studies, while some have more general applicability to real systems as well as fundamental studies. No technique, of course, can give all the information that is desired for any material unders study. Hence it is necessary to define what type of surface is under investigation, what properties of that surface are required to be known, and what the major assets and liabilities of each technique are. From this it is then possible to evaluate the suitability of a particular technique to the problem of interest, be it basic research, materials characterization, or process control. In this brief report, we begin by illustrating comnonly encountered surface structure/composition interrelations, outlining the two general ways in which surface sensitivity is achieved by the common microscopic techniques, and then classifying them according to the type of information they give. We then list the major criteria that should be applied in evaluating the usefulness of given technique. This is followed by a very brief summary of the major techniques and a bibiliography that the reader may wish to turn to for a more detailed discussion of individual techniques.

II. SURFACES, SURFACE SENSITIVITY AND CLASSIFICATION OF TECHNIQUES

A. Surface Structure/Composition Relationships

In Fig. 1 is shown a summary of the most comnonly encountered combinations of surface structure and composition. The most ideal situa-

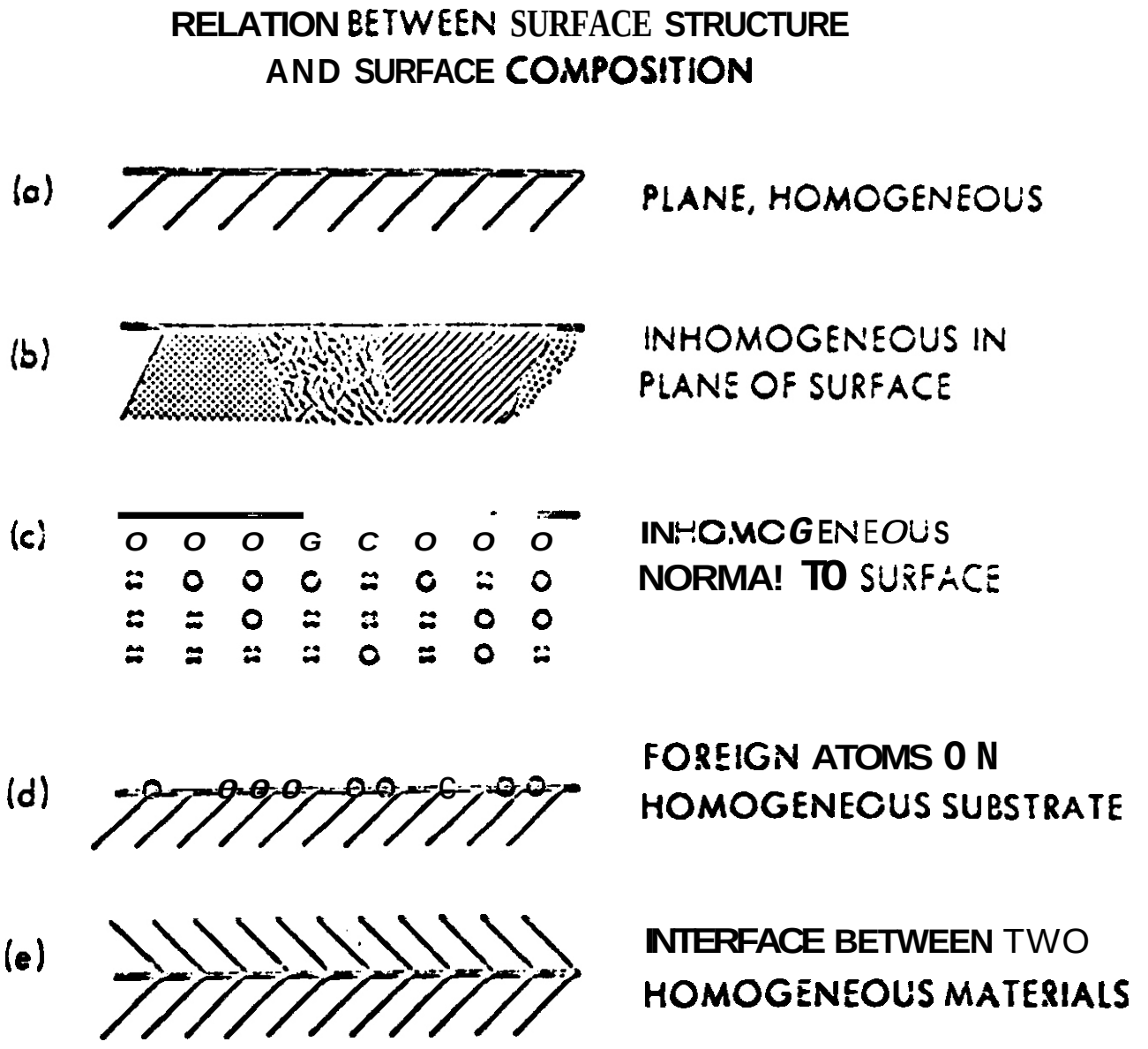

Figure 1. Relation between surface structure and surface composition. (From C. J. Powell, American Laboratory, to be published).

tions, and the one frequently assumed in real systems is shown as (a). Case (d) is comnonly encountered in chemisorption on single crystal surfaces. Most real situations fall into category (b) or (c) or worse yet, a combination of the two. Case (e) is more difficult to analyze with surface techniques because of the need to see the interface.

B. Surface Sensitivity

Surface sensitivity is achieved in two different ways. For electron spectroscopies, i.e., those techniques that depend on the measurement of the kninetic energy or momentum of an electron emitted from the solid, surface sensitivity is achieved because of the very short mean free path of slow electrons in solids. For an electron less than 1000eV, the mean free path is smaller than about 30-40 Å, with a minimum of about 3-5 Å for most metals in the energy range 50 to 200eV, giving two-to-three monolayer sensitivity. Major electron spectroscopies are Auger electron spectroscopy (AES), photoemission spectroscopy (PES, also called ESCA: electron spectroscopy for chemical analysis), low-energy electron diffraction (LEED), and energy loss spectroscopy (ELS).

The second group of techniques depends on the transfer of momentum from incident ions to achieve surface sensitivity. At sufficiently low energies (less than 1-2 kV) a certain fraction of the incident ions will be reflected without neutralization. Because the neutralization cross section is very high at these energies, reflected ions will come only from the outer layer. This is the basis for ion scattering spectrometry (ISS), touted as the only "true monolayer" technique. The incident ions that penetrate the surface will lose their momentum in a series of collisions, some of which will result in reversing the momentum direction. This leads to the escape of particles by "sputtering'. These particles come only from the surface region because, as in a series of collisions between billiard balls, only the last ball in line will actually move. This is the basis of secondary ion mass spectroscopy (SIMS). However, since cluster emission is possible, SIMS is not as surface sensitive as ISS.

Field ion microscopy (FIM) is a specialized surface technique that

depends on the ionization of gas atoms at a tip with a very high field gradient. It is discussed elsewhere in this volume. Rutherford ion backscattering (RIBS) is the high-energy analog of ISS. It is not a true surface-sensitive technique, but is quite useful in a number of applications. It is discussed elsewhere in this volume.

C. Classification of Techniques

Surface analytical techniques, as all others, can be classified into two broad categories, according to what information they give. These are elemental or chemical information, or geometric or structural information.

1. Elemental or Chemical Information

To determine chemical information, it is necessary to determine 1) what elemental species are present, 2) how much of each species is present, 3) what is its chemical form, i.e., does it occur as a pure element or as a compound, and 4) its dispersion, i.e., does it occur as a precipitate, uniformly dispersed, or segregated to boundaries. Furthermore it is of interest to follow the dynamics of a given elemental or chemical distribution, i.e., how much of what is moving from point A to point B in what time. The major techniques that are capable of giving elemental or chemical information are AES, ESCA. SIMS, and ISS.

2. Geometric or Structural Information

The most important geometric information of interest in surface analysis is, of course, the crystal structure of the surface or precipitate; i.e., the size and shape of the unit mesh and the positions of the atoms in it. Additionally, it is desirable to obtain a quantitative measure of the density of point and extended defects (including steps) on surfaces, and to study the thermodynamics and kinetics of surface structure formation, such as crystal or island growth, surface diffusion, and phase transformations in two-dimensional or quasi-two-dimensional systems. LEED is the major technique that provides such information.

111. CRITERIA FOR EYALUATING ANALYTICAL TECHNIQUES

Each technique has its own strength and weaknesses, and no single technique can provide a total analysis. In evaluating the applicability of a technique to a given problem, it may be useful to consider the following criteria:

--Elemental Analysis Techniques—

1. Sensitivity (absolute)
2. Sensitivity variation with Z
3. Element discrimination
4. Quantitative capability
5. Matrix information (chemistry)
6. Depth of analysis, depth resolution
7. Lateral resolution
8. Surface damage

--Structural Analysis Techniques--

1. Resolution of lattice parameters
2. Sensitivity to defects and/or long-range order
3. Depth of analysis, depth resolution
4. Lateral resolution
5. Surface damage

IV. MAJOR TECHNIQUES: PHYSICAL PROCESSES AND DISTINGUISHING FEATURES

A. Auger Electron Spectroscopy (AES)

The Auger effect is a deexcitation mechanism for ionized atoms that is competitive with x-ray emission. It yields a low-energy electron whose kinetic energy is characteristic of the element from which it came. Thus each element has its own signature. A series of Auger electrons results if a deep core level is originally ionized. For example, if a K shell is ionized, an Auger process can occur with an L shell electron dropping into the K shell, the excess energy being taken up by another L-shell electron (KLL process), an M-shell electron (KLM process) or an

even higher level. This is then followed by LMM, etc. processes where the hole(s) on the L shell is(are) now being filled. The strongest Auger processes are generally those involving the valence shell and a core level close to it in energy; these are also the transitions that are the most surface sensitive, because the emitted electron has a kinetic energy near the minimum in mean free path.

The major features of AES are that all elements can be analyzed except for H and He, with a sensitivity differing no more than about one order of magnitude; a lateral resolution of <1000 Å is commercially available, and 300 Å has been demonstrated; the technique is in many cases quantitative to within an uncertainty of ± 50%, and, on the scale of surface analytical instrumentation, the technique is relatively easy and cheap. The detection limit for reasonable laboratory times is about 10^{-3} monolayers (1000 ppm if uniformly dispersed). A typical Auger spectrum is shown in Fig. 2.

B. Photoelectron Spectroscopy (PES or ESCA)

Photoelectron spectroscopy is simply the application of the photoelectric effect to elemental and chemical analysis. It is an excitation technique, where the incident photo is absorbed by an electron, which is ejected from the atom with a kinetic energy equal to the difference of the energy of the photon and the binding energy of the electron that absorbed it. The kinetic energy of the photoelectron is measured in the experiment. Because each element has a unique set of atomic energy levels, each element has its own signature of photoelectron emission lines for a given photon energy. Surface sensitivity is again obtained because the kinetic energy is low. However, for typical commercially available sources (Al K_α and Mg K_α) the depth resolution is not as good as in AES, since many important photoelectron transitions occur at kinetic energies. up to 1450 eV. Using synchrotron radiation, it is possible to do photoelectron spectroscopy at any energy, since the photo energy is tunable with such sources.

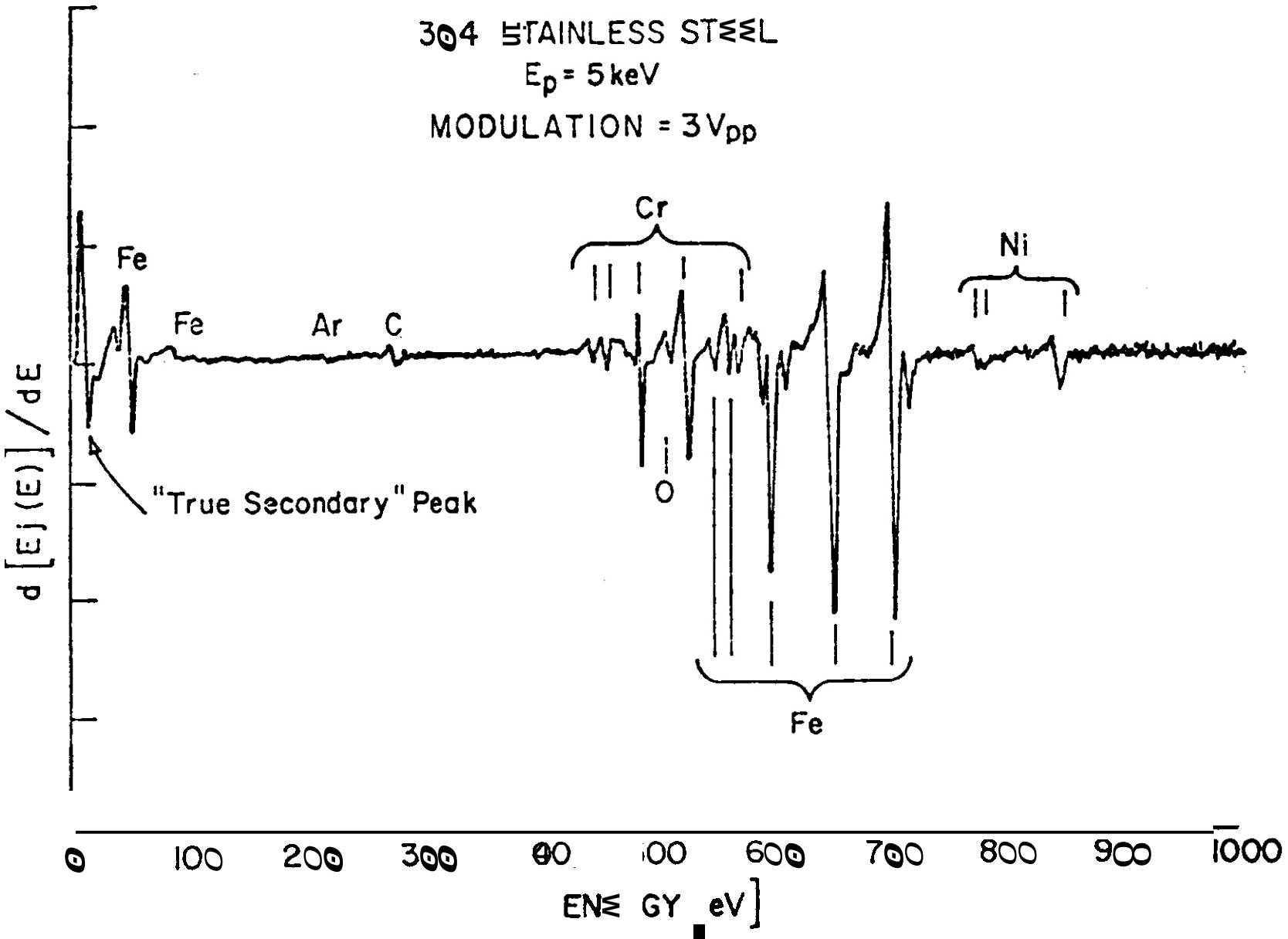

Figure 2 Auger spectrum of stainless steel (From S N Sickafus, J EMMSE 1, 1 (1973))

The outstanding assets of PES are that it can provide very good chemical information (through a phenomenon called the chemical shift, which is an adjustment of energy levels due to charge transfer in chemical bonding) and that it is less damaging to materials susceptible to electron beam damage, such as polymers. It is less sensitive than AES, thus requiring longer time to achieve given statistics. H and He are in principle observable, although the cross section for photoelectron emission from them is very low. Other than these, the relative sensitivity of XPS (with Al or Mg anodes) is within an order of magnitude for all elements. The technique is in many cases quantitative to ± 50%. Since photons are difficult to focus, good lateral resolution is not readily achievable with this method. A typical ESCA spectrum is shown in Fig. 3.

C. Secondary Ion Mass Spectroscopy (SIMS)

This technique depends simply on mass spectroscopic analysis of ions ejected from a surface by an incident ion beam. The simplest SIMS units consist of an ion gun and a mass spectrometer with an energy filter, although very complex instruments, such as the ion microprobe, are also used. The depth sensitivity is better than several monolayers, as indicated earlier.

The outstanding features of SIMS are highest detection sensitivity of all surfaces probes for many elements ($<10^{-4}$ monolayers) and very good sensitivity to H. Isotopic surface analysis is also possible with a good mass spectrometer. Focussed ion beams make good lateral resolution a possibility. The major disadvantage of the technique is extremely strong matrix effects, which make quantitative analysis suspect in any but the simplest cases. The measurement process, of course, damages the surface. A SIMS spectrum is shown in Fig. 4.

D. Ion Scattering Spectrometry (ISS)

In ISS, the kinetic energy of a reflected ion with incident energy less than about 2kV is measured at fixed geometry. The analysis is in terms of classical momentum transfer in elastic collisions between billiard balls of different mass. The ratio of final to initial kinetic energy of an ion of known mass scattered through a known angle will give the mass of the target (surface) atom. This identifies the surface atom.

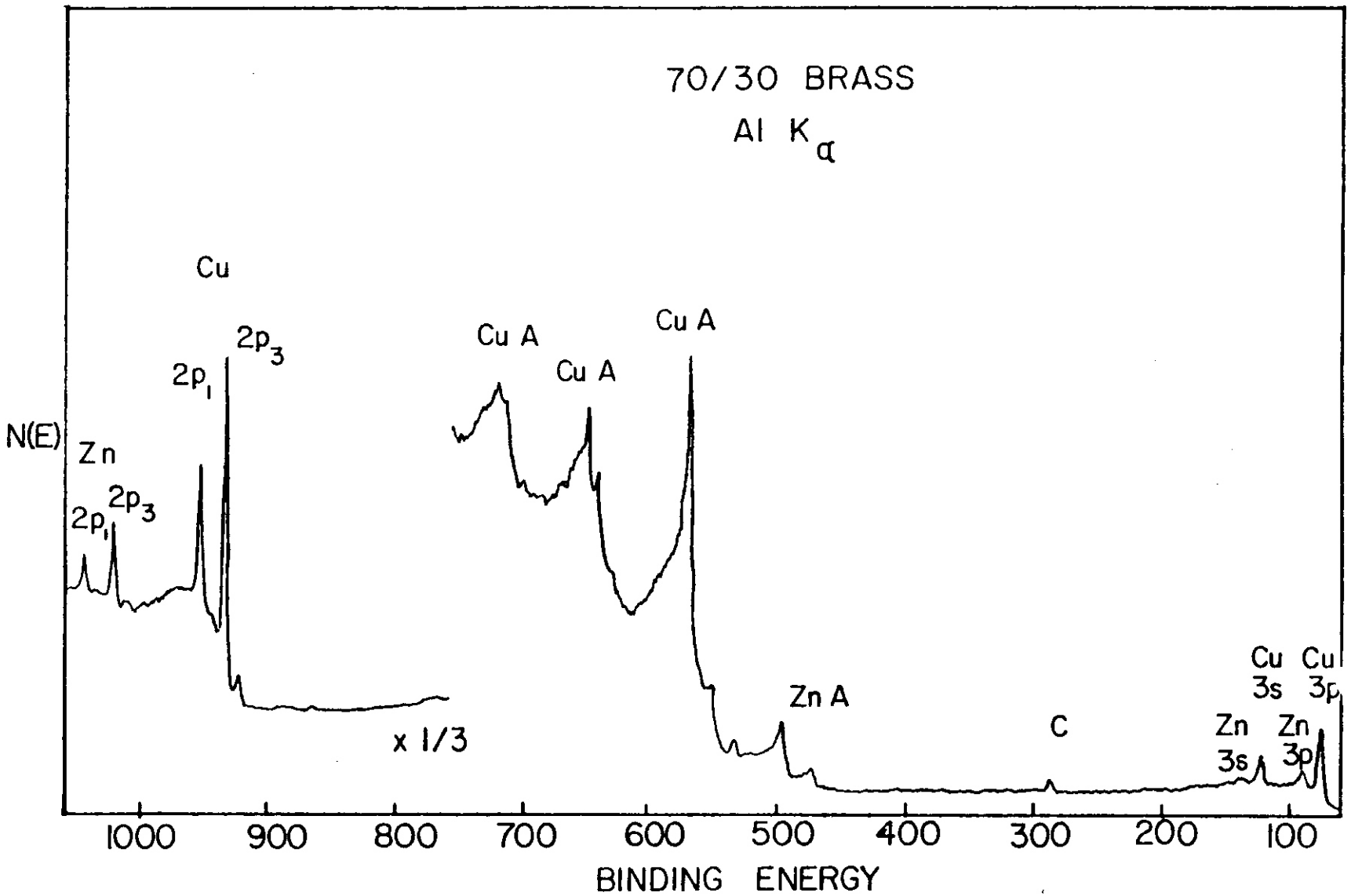

Figure 3. ESCA spectrum of 70-30 brass, also showing several Auger peaks.

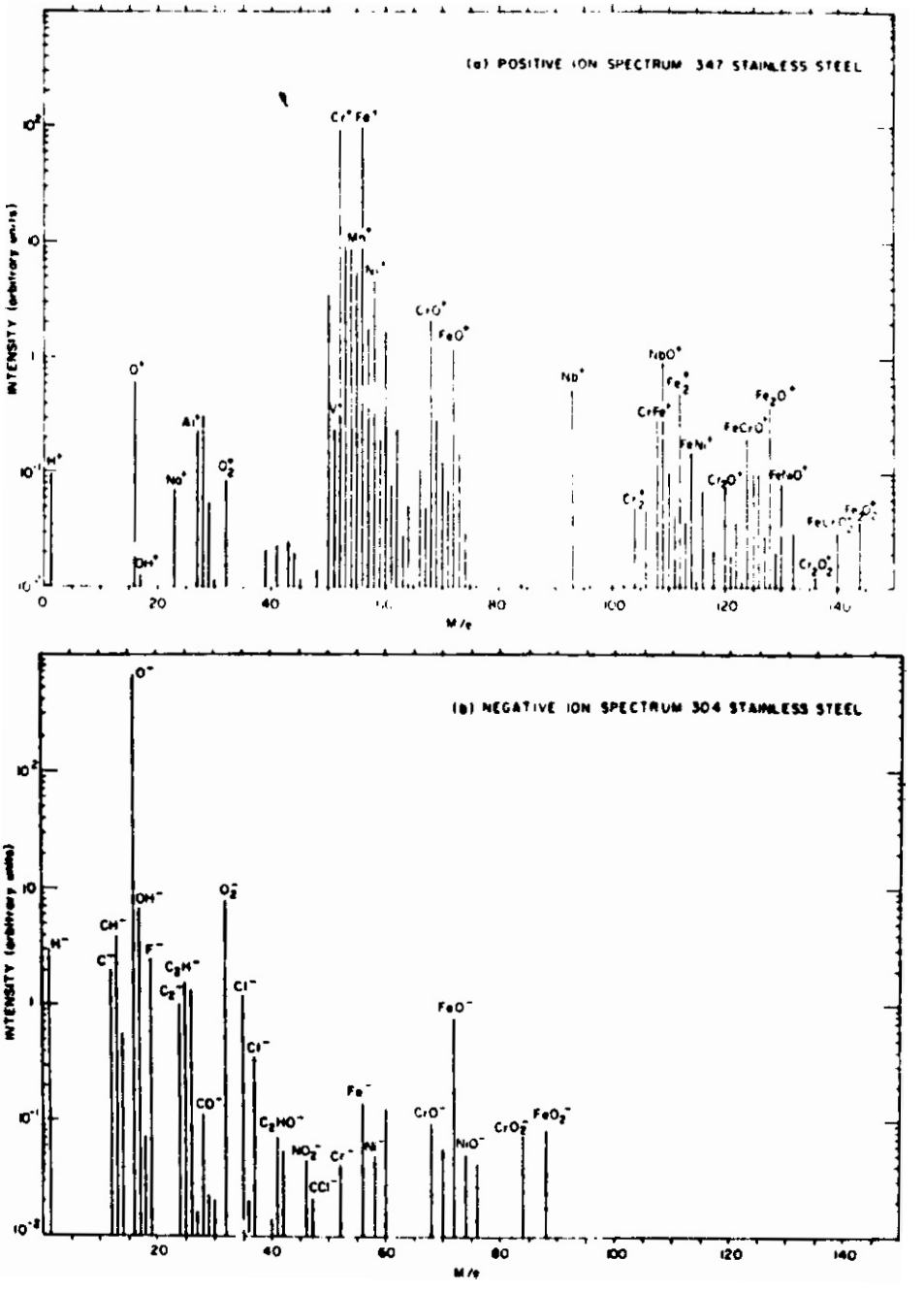

Figure 4. Positive and negative SIMS spectra of stainless steel (From J. A. McHugh, in Methods of Surface Analysis, ed. A. W. Czanderna, Elsevier 1975).

As already indicated, ISS is probably the most surface-sensitive of all probes, because of the very large neutralization cross section for ions that penetrate the lattice. The technique has relatively low sensitivity; there is a tradeoff between surface damage and time to acquire a signal with sufficient statistics. Focussed beams are possible, giving lateral resolution. Element resolution between neighboring elements is difficult; different projectile ions can be used to improve the mass resolution. A typical spectrum is shown in Fig. 5.

E. Low Energy Electron Diffraction (LEED)

LEED is the only commonly available technique that gives surface structural information. The angular distribution of electrons elastically scattered from a crystalline surface is measured as a function of the energy of the incident electrons. The technique is the surface analog of x-ray or high-energy electron diffraction; the surface sensitivity comes from the 0-1kV energies used in the method.

The outstanding features of LEED is the very easy determination of surface order and the size and shape of the unit mesh, simply by observation of the diffraction pattern. It has also been used to determine equilibrium positions of atoms in surfaces and overlayers, although such analyses are much more difficult. Surface extended defects, including steps, mosaic structure and strain effects, can be readily analyzed by measuring the angular distribution of intensity in the diffracted beams, with a sensitivity of about 1% of surface sites. Thermodynamics of ordered surface structures or segregation to surfaces can be studied by observing superlattice diffraction peaks. No materials characterization is, of course, possible, and the technique has so far been used only on single crystals, although scanning LEED is in principle possible. Surface damage to sensitive materials is possible, and, as with all electron spectroscopies, analysis of insulating materials is difficult.

V. CONCLUSION

Surface analysis has grown tremendously in the last fifteen years, and it is impossible to cover even one technique adequately in the limited

space available here. A number of books have been written on the various techniques. As a consequence, it seems efficacious to list some useful references rather than to extend the discussion. These are arranged in the bibliography according to technique.

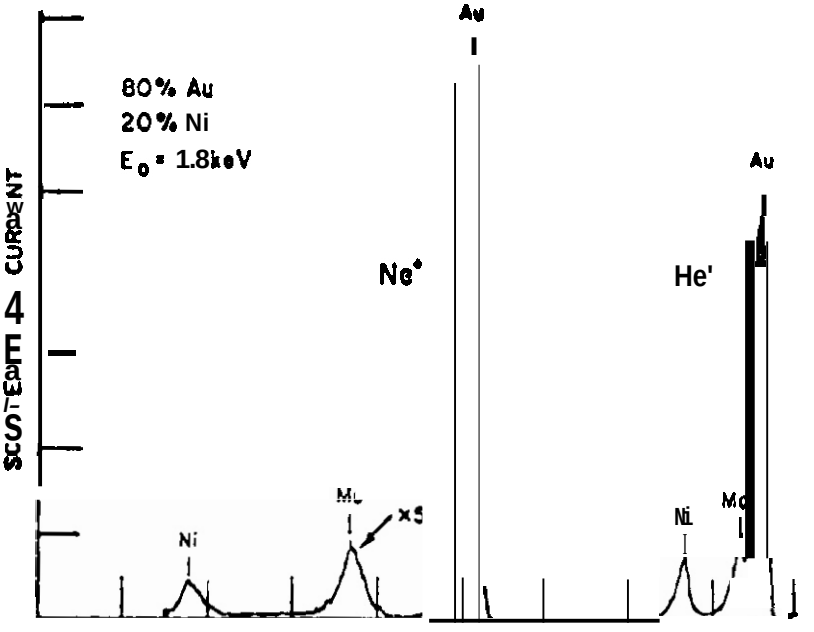

Bibliography

I. GENERAL OR MORE THAN ONE TECHNIQUE

1. Methods of Surface Analysis, ed. A. W. Czanderna (Elsevier 1975).

2. Characterization of Solid Surfaces, eds. P. F. Kane and G. B. Larrabee (Plenum 1974).

3. Systematic Materials Analysis, ed. J. H. Richardson and R. V. Peterson (Academic 1974).

4. Treatise in Solid State Chemistry, Vol. 6A, ed. N. Hannay (Plenum 1976), Chapt. 2.

5. Chemistry and Physics of Solid Surfaces, Vol. I, eds. R. Vanselow and S. Y. Tong, (CRC Press 1977).

6. Chemistry and Physics of Solid Surfaces, Vol. II, eds. R. Vanselow and S. Y. Tong, (CRC Press 1979).

7. R. L. Park, "Chemical Analysis of Surfaces" in Surface Physics of Materials, Vol. 11, ed. J. M. Blakely (Academic 1975).

a. Interfacial Segregation, Eds. W. C. Johnson and J. M. Blakely (ASM, 1979).

9. G. Ertl and J. Küppers, Low-Energy Electrons and Surface Chemistry, (Verlag Chemie, 1974).

10. C. J. Powell, The National Measurement System for Surface Properties, N.B.S. Report NBSIR 75-945. C. J. Powell, Appl. Surf. Sci. 2, xxx (1979).

11. quantitative Surface Analysis of Materials, ed. N. S. McIntyre, ASTM STEP 643, (ASTM, 1978).

12. K. A. Sevier, Low-Energy Electron Spectrometry–, (Interscience 1972).

13. A. W. Mullendore, G. C. Nelson and P. H. Holloway, "Surface Sensitive Analytical Techniques: An Evaluation", in Proc. Adv. Techniques Failure Analysis, Los Angeles (IEEE 1977) pg. 236.

14. Electron Spectroscopy for Surface Analysis, ed. H. Ibach (Springer 1977).

15. Surface Analysis Techniques for Metallurgical Applications, eds. R. S. Carbonara and J. R. Cuthill (ASTM 1976).

11. SPECIFIC TO A PARTICULAR TECHNIQUE

1. E. N. Sickafus, J. EMMSE 1, 1 (1979) [AES].

2. P. H. Holloway, "Quantitative Auger Electron Spectroscopy: Problems and Prospects", in Scanning Electron Microscopy, 1978 Vol. I, ed. 0. Johari (SEM 1978).

3. T. A. Carlson, Photoelectron and Auger Spectroscopy (Plenum 1974).

4. Siegbahn, et al, "AES and ESCA", ESCA (Almqvist and Wiksell 1967).

5. R. S. Swingle and W. M. Riggs, Critical Reviews in Analytical Chemistry, 5, 262 (1975) [ESCA].

6. Secondary Ion Mass Spectrosmetry, eds. K. F. J. Heinrich and D. E. Newbury, NBS Spec. Publ. 427 (1975) [SIMS].

7. J. T. McKinney and J. A. Leys, Eighth National Conference on Electron Probe Analysis (New Orleans, 1973) [ISS].

8. G. C. Nelson, J. Colloid Interface Sci. 55, 289 (1976) [ISS].

9. M. B. Webb and M. G. Lagally, Solid State Physics 28, 301 (1973) [LEED].

10. M. G. Lagally, G.-C. Wang, and T.-M. Lu, Critical Reviews in Materials and Solid State Sciences 7, 233 (1978) [LEED].

V. WORKSHOP DISCUSSION

Discussion Period

(An edited summary to bring out discussion highlights)

D. Doran: Which of the techniques are able to detect the structure of a single cascade and to measure the numbers and types of defects produced ?

R. Hendrix: X-ray and neutron scattering gives averaged data not single cascades. Also if many different clusters occur, the total scattering includes all of them. In addition, even for a single defect or cluster one needs a good theoretical model to relate scattered intensity to defect structure. Progress along these lines is currently being made at several laboratories. When complemented by electron microscopy, small angle scattering techniques provide a rapid and easy way of measuring complete defect populations, especially for voids.

D. Seidman: Field Ion Microscopy is a powerful tool for studying depleted zones in the absence of point defect diffusion. It requires:
(1) A high number density of cascades due to the small volume observed.
(2) Only a few cascades per specimen (<8).

Within these limits one can obtain a detailed picture of a small number of cascades.

In pure materials, W, Pt, Al, Ni good FIM images have been produced. In alloys (except for ordered materials) the image looks random as the solute concentration increases.

T. Picraux: Ion channelling is similar to small angle scattering in that an average result is obtained. It is best used on simple systems where the defects are known. The technique is best used for secondary damage structures.

R. Siegel: Position Annihilation Spectroscopy has the attraction that is provides information over the whole spectrum of vacancy defects from single vacancies to large clusters and voids. There is of course a deconvolution problem if all of these are present at the same time. In my paper where electron and neutron irradiated specimens are compared, one could see very

distinctly (fig. 10) the longer positron lifetime for the neutron case, presumably due to depleted regions within cascades. It should therefore be possible to determine at least the number of vacancies in the depleted zones. However, the sensitivity to interstitial defects is small.

R. Sinclair: Direct lattice resolution by electron microscopy samples a column of crystal at each point with perhaps a hundred atoms in each column. As a result, a single vacancy would probably be undetectable. However. centers of strain interstitials for example probably could be studied. It requires the use of models and detailed diffraction calculations (for which caputer codes are now available). However, neither the calculations nor the observations have yet been made.

J. Bently: We have been able to use the converging beam diffraction technique in the electron microscope to study a single dislocatian which we fully characterized. We do not yet understand all the details but the technique clearly has the potential for probing the structure on a very fine scale.

F. Fradin: Hyperfine interaction techniques are all point probes applying a very specific intensity to a very small defect or complex. It is therefore best used for single defects or complexes and their relaxations, including vacancies, interstitials, solute/vacancy and solute/interstitials. They are inappropriate for large regions like cascades.

D. Seidman: There is a problem with high resolution microscopy for single defects. The beam excites the defects so that single interstitials for example can be made to move below stage I. This has been observed.

R. Sinclair: That may not be such a limiting problem. One has to take into account the probability of an elastic interaction event with electrons from the beam. If this is low, the excitation events will be rare. Alternatively, if it does become a problem, the scanning transmission technique can be used in which the time of beam exposure is small.

D. Potter: Do we have any technique for observing clustering of solute atans within a cascade?

D. Seidman: Yes, one could do localized chemistry of the structure of the cascades by the ion probe on the FIM.

D. Doran: Can any of the techniques distinguish between high energy cascades from 14 MeV neutrons and lower energy cascades? In particular, could gas atoms produced by 14 MeV neutrons be detected if associated with cascades?

D. Seigel: The positron is sensitive to any significant change in the atomic structure of the state it is occupying. In the case of voids for example, gas contents or precipitate coatings are detectable. In fig. 10 of my paper on irradiated Mo, the extra increase in the position lifetime at high temperatures was found subsequently to be the result of annealing in an argon atmosphere. The gas was pumping into the voids and enhancing the lifetime.

The sensitivity therefore exists to obtain data on gas association with vacancy rich defects.

R. Odette: Each of the techniques seems to have a blind spot for particular kinds of defects. Can the panel give us some idea of what combination of measurements might eliminate these blind spots?

R. Hendrix: If it were the situation where each of the techniques could be applied to a specific kind of defect then one could do what you propose. However, it is usually not a matter of being unable to see something but of seeing too much and not being able to unravel it.

This applies to the non-localizing techniques like position annihilation, X-ray scattering and perhaps channelling. It is very difficult to deconvolute the result of scattering from many different kinds of defects and extract the inherent noise of the instrument.

For the scattering techniques at small angles, we can say that for voids with dislocation networks useful results can be obtained. If there are voids and random interstitial loops with no precipitates, this too is acceptable. If we have precipitates, voids and loops, the problem is intractable.

R. Siegel: Certainly in the positron case one is not faced with similar sensitivity to all defect types. In complex microstructures with vacancies and vacancy clusters, interstitials and interstitial clusters, dislocations and precipitates, positrons are primarily sensitive to the vacancy type defects.

The rest fall into a background. One is very sensitive to void formation, vacancy clusters and vacancies, and relatively insensitive to dislocation loops of both kinds. The technique provides qualitative information on the vacancy population in a real system.

T. Reuther: I think it is very important for practical reasons to separate the early stages from the later stages of microstructural evolution when voids are growing by Tong range transport. The general approach to produce radiation resistant materials is to delay the onset of long range transport. We have a better chance if we can beat the nucleation and growth stage from an engineering viewpoint. We therefore need to be able to look at distributions early in the nucleation stage.

W. J. Choyke: Is it possible to use Electron Energy Loss Spectroscopy to detect hydrogen and helium?

D. Joy: By using an aperture plane rather than a slit to collect the electrons, it is possible to separate the unscattered or elastically scattered electrons from those which have been inelastically scattered. The ratio of these two signals is proportional to the mean atomic number of the atoms in the volume of crystal being sampled. This proportionality is maintained over the entire periodic table and the technique has been applied to detect the loss of hydrogen in certain solids.

W. J. Choyke: Professor Sinclair mentioned that with ultrahigh resolution TEM techniques it is possible to observe effects of hydrogen and helium in the lattice. Are the techniques limited to "superfoils" of single crystal gold or iron, etc.

R. Sinclair: The imaging techniques I was referring to only require that atoms become displaced from their true positions because of the distortion introduced by a reasonable concentration of solute. This has proven to be a detectable and measurable effect in "commercial" iron-carbon alloys, for example. In fact very small carbon content differences have been measured by determining atomic spacing differences within the material. In principal, similar measurements can be made in thin foils made from other normal poly-crystalline materials for any solute that gives a large distortion relative to its concentration.

W. J. Choyke: It appears that a subsidiary part of the ion channeling and backscattering techniques, namely, nuclear reaction techniques, are most powerful in detecting and measuring hydrogen and helium in solids.

T. Picraux: That is correct. Techniques using nuclear reactions have been well developed. One can detect any isotope of hydrogen or helium and depth profile it in the first ten microns or so of the surface. It is possible to obtain valuable information about transport properties in this way.

W. J. Choyke: FIM-atom probe measurements indicate that helium can diffuse at 95°K. What do these measurements really tell us about the mobility of helium inside a metal far from the surface?

D. Seidman: I would like to make two points with respect to this question. First, the FIM-atom probe technique is not looking at helium moving on the surface but to the surface from the bulk of a little laboratory which has a volume of $\sim 10\ cm^3$. Except for (possibly) the last few jumps, the surface does not affect the overall migration. Second, this technique is currently being used to measure intrinsic diffusive properties of helium in defect-free crystals. If there were vacancies present, for example, they would be excellent deep traps for helium as a number of theoretical calculations have shown.

W. J. Choyke: The hyperfine interaction is apparently sensitive to strain. Could the hyperfine techniques sense the presence of surface stresses in helium-doped material?

F. Fradin: I think it would be very difficult to obtain quantitative information about long range stress fields. Moreover, looking at distributions of gas atoms in solids to determine whether they are occupying lattice positions or sitting in clusters of various sizes is a problem that cannot be solved easily using hyperfine techniques.

P. Okamoto: What can these techniques tell us about the detailed mechanisms of solute segregation? We know it is mainly a diffusion phenomenon and hence requires detailed knowledge of point defect formation energies, defect configurations and their migration mechanisms and energies.

M. Lagally: If the segregation occurs on a reasonably large scale with laterally homogeneous compositions over distances on the order of 0.1 μm, then Auger spectroscopy coupled with ion sputtering offers a means of getting very

good depth information on solute concentration profiles. The technique does not provide direct information on the contributions of vacancies and self-interstitials on interdiffusion phenomena. If the dominant mass-transport process is known, however, then the technique can be used to study the kinetics of the process.

P. Okamoto: How serious are the effects of preferential sputtering when one is trying to measure a concentration profile in this way?

M. Lagally: It depends on the metal and on the details of the system (sputtering ion mass and energy, etc.). Preferential sputtering can be a very serious problem resulting in changes of 50% or more in the actual surface composition. A separate analysis using standards is necessary to sort out the effects.

R. Siegel: There are a number of techniques, not represented in this workshop, which are very useful for obtaining point defect formation and migration energies and for determining the configurations and mobilities of point defect/solute complexes. Various relaxation techniques, electrical resistivity measurements, etc., have been applied in this general area of "defect physics." Such techniques should certainly be applicable for determining the mechanisms of radiation-induced solute segregation.

R. Hendricks: To the extent that solute segregation phenomena represent changes in the state of local atomic order - short range order - diffuse X-ray scattering and neutron scattering techniques for studying such effects have been well established for many years. They are best applied to alloys with solute concentrations greater than a few percent, in general, but the practical limits depend on the alloy system.

D. Joy: The EDS and EELS techniques are not very well suited for determining solute concentration changes in dilute solutions. It is unlikely that changes on the order of 1 part in 100 could even be detected.

D. Potter: Precipitate nucleation and growth under steady-state or pulsed irradiation are very complex processes. It is likely they involve cascade-enhanced nucleation and resolution effects as well as solute-point defect coupling effects which can dramatically alter precipitate nucleation and growth rates. How well can these techniques characterize precipitates and solute concentration profiles extending only a few hundred angstroms?

D. Seidman: Dr. Sid Brenner at U.S. Steel Research Laboratories has demonstrated the usefulness of combining TEM and FIM-atom probe techniques to fully characterize rather complex precipitates in the Fe-N and Fe-C systems. The only restrictions are the requirements for either a high number density of precipitates ($\sim 10^{15}/cm^3$) or particles of sufficient dimensions that they can first be located by imaging the FIM specimen in the electron microscope.

R. Sinclair: The high resolution electron microscope techniques are also applicable here if the solute causes sufficient lattice distortion. One of the biggest advantages of these techniques is the excellent spatial resolution because one observes the particle and adjacent regions plane by plane. Thus it is straightforward to obtain composition profiles which are referenced with respect to a microstructural feature.

M. Lagally: If the particles are large enough ($\sim 0.1\ \mu m$), SEM combined with scanning Auger spectroscopy can be used to find a particle and depth probe (by sputtering) through the particle into the matrix. The depth resolution would be tens to hundreds of angstroms. Improving the lateral resolution of the auger technique by tightening the electron beam is difficult because of signal to background considerations, space charge limitations, beam heating of the sample and topographic contrast effects.

J. Bentley: For observing and measuring populations of small voids, it appears that conventional transmission electron microscopy still reigns supreme for voids which are greater than ~ 15 Å in diameter. FIM and high resolution TEM are probably most useful for sizes smaller than 15 Å. The scattering techniques, especially small angle X-ray scattering, may be a way of providing better statistics in a quicker way than TEM and a more rapid way of determining swelling. Does anyone on the panel disagree with this assessment?

R. Hendricks: I would modify it slightly. Fifteen angstrom diameter cavities are probably at the lower limit for small angle scattering measurements.

F. W. Wiffen: Experiments are in progress at Brookhaven and ORNL to cross-calibrate positron annihilation, TEM and small angle X-ray scattering measurements on identical irradiated specimens. The positron annihilation and TEM results agree very well.

VI. COMMENTS

Applications of Workshop Techniques to Precipitation

D. I. Potter

Precipitation during irradiation may occur by solute clustering and formation of precipitate embryos. These commonly grow, by depleting the matrix of solute, or coarsen, whereby larger particles grow at the expense of smaller ones. Particles may also dissolve, perhaps by cascade dissolution at their surfaces or by irradiation-induced-segregation fluxes causing solute depletion at points where point-defect-sinks contact the particle surface. Parameters of importance in characterizing precipitation include particle size distributions, average particle size, particle number density, and volume fraction precipitate. These can be obtained from TEM as well as low angle x-ray or neutron scattering (R. Hendricks). Irradiated particles are often irregular in shape and morphological characterization is best done with dark field TEM.

Nucleation of precipitates can be monitored with positron annihilation (R. Siegel), nuclear magnetic resonance or Mossbauer spectroscopy (F. Fradin) with some hope of identifying heterogeneous nucleation within cascades. The chemistry of precipitates can be determined with EDS or EELS (D. Joy) from particles $\gtrsim$ 100 Å in diameter. The stability of larger particles depends on local chemistry i.e. solute gradients, and differentiation between various dissolution mechanisms requires quantitative evaluation of these gradients. This is best obtained by combining the ion-probe of field ion microscopy (D. Seidman) with lattice imaging in TEM (R. Sinclair). In the latter case, variations in lattice fringe spacing provide a measure of solute concentration and can be used to study chemistry localized to regions $\lesssim$ 50 Å.

Average matrix concentration can be monitored with conventional x-ray diffraction techniques (disappearing-phase method or parametric method) or more accurately by monitoring intensities of hyperfine interactions (NMR, Mossbauer) and use of the enhanced lever rule[1]. Electrical resistivity may also provide information about average solute concentration in the matrix.

1. L. H. Bennett and G. C. Carter, Met. Trans, vol. 2, 3079 (1971).

Applications to Studies of Cascade Structure

D.G. Doran

The only techniques discussed that appear promising are field ion microscopy (FIM), ultrahigh resolution transmission electron microscopy (UHRTEM), diffuse x-ray scattering, and positron annihilation.

The FIM technique has well known limitations, including materials, cascade energy, inability to see whole cascade, proximity of surface, and low throughput. On the other hand, it is the most direct approach we have and could benefit from an increase in the number of investigators in the field. In particular, a facility dedicated to, or at least strongly influenced by, the DAFS Program could operate beneficially for a number of years. This would permit selection of materials and initial conditions, of specific parameters for study, etc.

The application of UHRTEM to the study of cascades deserves further consideration. As I understand it, if there is sufficient strain associated with the cascade, its presence should be revealed. The interpretation of the image would require calculations for various models of the cascade structure. It is not clear to me at this time how quantitative such observations could be. I presume that any information gained must be considered supplementary to that gained by other means, rather than complete in itself. UHRTEM is being investigated as part of the HEDL RTNS-II Program.

Diffuse (high angle) x-ray scattering may be applicable to the study of cascades, according to Hendricks. I gather that this requires a high degree of specialization coupled with good theoretical calculations. It might provide volume average data to supplement observations on single cascades. B.C. Larson at Oak Ridge is preparing to make such measurements in several months on copper, ion irradiated below stage I-E.

Positron annihilation is another technique that appears to have possibilities under carefully controlled conditions. It is not clear that a specimen containing a wide range of sizes and configurations of vacancy aggregates is analyzable. However, since the measurement is sensitive primarily to vacancy type defects, it might supplement measurements using diffuse x-ray scattering. A comparison of high purity and dilute binary alloys specimens might shed light on whether the solute influences the size and configuration of the cascade debris, on solute aggregation at cascades, etc. Annealing studies would be a natural part of such experiments.

Applications to Hydrogen and Helium Detection

W.J. Choyke

Almost all the techniques except AES described at the workshop lend themselves in some way to the study of hydrogen isotopes and helium in solids.

Two points were brought out in the discussion which might be emphasized:

1. There are many ways that one can obtain profiles of hydrogen and helium all of which are, in a sense, particle scattering techniques related to the channeling technique discussed by S.T. Picraux. An instructive review has recently been given by J. Bottiger of Aarhus.[1]

2. D.N. Seidman discussed FIM measurements of the diffusion of He in perfect crystals at 95°K. In the question period the issue was raised as to whether such a measurement really constituted the bulk diffusion of He in a solid since experience with irradiated samples indicates that He moves very little at elevated temperatures (800°K). Theoretical estimates (Wilson) of the trapping energy for He in a perfect crystal are very small and agree well with values deduced by Seidman. On the other hand, the trapping to a vacancy is of the order of several volts (Wilson). This appears to explain the fact that under radiation environments and in less than perfect samples He is extremely well trapped.

(1) J. Bottiger, J. Nucl. Mater. 78 (1968), p. 161.

USEFULNESS OF THE WORKSHOP TECHNIQUES IN THE CONSTRUCTION OF MATHEMATICAL MODELS OF RADIATION DAMAGE

M. R. Hayns

The first aim of the workshop, to examine the state of the art in techniques for investigating radiation damage was undoubtedly successful. The speakers gave a clear impression of the advances made recently. It is clear that the possibility of obtaining very detailed information is present. I think that the second aim of the workshop, the determination of the usefulness of the techniques for CTR materials and the definition of new experiments was not so successful, mainly because it was very difficult to grasp the implications of some of the measurements being offered in terms of our previously rather "coarse" way of looking at irradiation-induced microstructure. Hopefully, once the papers have been made available, a clear picture will emerge. From a theoretician's viewpoint, the possibility of observations which can identify essentially single atoms is both exciting and daunting. The excitement arises from the possibility of characterizing very small aggregates and hence leading to a much better understanding of the nucleation processes, and of the segregation of rather small quantities of impurities to extended defects and surfaces. It is daunting because these areas have traditionally been "unobservable" and hence the crude assumptions used to model them could not be vigorously examined.

Two main aspects of the measurement techniques emerged, first that structural information is becoming very much more detailed, but this means that overall microstructure is neglected in the much higher resolution experiments. Further, these techniques tend to be only useful at present for very specialized materials, e.g., heavy metals for FIM or very particular geometrics of samples. On the other hand, the scattering techniques which average over the bulk of the material offer methods of rapid assessment of the irradiation microstructure, at a better level than previously available in rapid screening techniques (e.g., density, or step height measurements). Traditional electron microscopy still plays a vital role in the "middle ground," with the possible enhancement of its usefulness by means of automated counting techniques.

It seems clear that the very high resolution methods need careful assessment in terms of the detailed usefulness to the overall CTR materials program. As instruments for extending our basic understanding, they are exciting possibilities. The special averaging techniques look very useful as a way of obtaining a reasonable assessment of the large amount of neutron data becoming available, but these results have to be seen in connection with sufficient TEM to expose the behavior of the whole microstructure, and not just cavities, if full use is to be made in creating physical models of the observed damage.

DISTRIBUTION

UC-20 (119)

UC-20c (77)

DOE-HQ/Office of Reactor
Research and Technology
NE-530
Washington, DC 20545

PB Hemmig, Safety & Physics

DOE-HQ/Office of
Fusion Energy (3)
Washington, DC 20545

JF Clark, ER-70
JF Decker, ER-54, G-256
TC Reuther, ER-70

DOE-RL/Office of Asst Manager For
Projects and Facilities Management (2)

GM Chenevert, FMITPO

DOE-RL/Office of Asst Manager
for Advanced Reactor Programs

AR DeGrazia, Physical Scientist,
Technology Development

Argonne National Laboratory (13)
9700 South Cass Avenue
Argonne, IL 60439

FY Fradin
LR Greenwood
K-Y Liou
KL Merkle
RE Nygren
FV Nolfi
PR Okamoto
Lynn Rehn
RW Siegel
DI Potter
A. Taylor
APL Turner
H. Wiedersich

Battelle Memorial Institute (3)
Pacific Northwest Laboratory
P.O. Box 999
Richland, WA 99352

JL Brimhall
DA Dingee
TD Chikalla

Bell Laboratories
Materials Research Division
600 Mountain Avenue
Murray Hill, NJ 07974

DC Joy

Brookhaven National Laboratory
Associated Universities
Upton, Long Island, NY 11973

Chairman, Nuclear Energy Dept

Columbia University
Plasma Physics Laboratory
New York, NY 10027

RA Gross

Cornell University
Dept of Materials Science & Eng
Bard Hall
Ithaca, NY 14853

OM Seidman

EG&G Idaho, Inc
P.O. Box 1625
Idaho Falls, ID 83415

RW Schmunk

DISTRIBUTION (Cont'd)

General Atomic Company (2)
P.O. Box 81608
San Diego, CA 92138

GR Hopkins
JR Gilleland

Georgia Institute of Technology
School of Chemical tng
Atlanta, GA 30332

S. Spooner

INESCO
11011 Torreyana Rd
San Diego, CA 92121

RD Stevenson

Lawrence Livermore Laboratory (2)
P.O. Box 808
Livermore. CA 94550

MW Guinan
CM Logan

Los Alamos National Laboratory (2)
P.O. Box 1663
Los Alamos, NM 87544

DJ Dudziak
CR Emigh

Massachusetts Institute of Technology (5)
77 Massachusetts Avenue
Cambridge, MA 02139

L. Lidsky
I- W Chen, 13-5118
NJ Grant, 8-305
DB Montgomery, NW21
JB Vander Sande, 13-5025

Massachusetts Institute of Technology
Nuclear Reactor Laboratory
138 Albany St
Cambridge, MA 02139

OK Harling, NW12-204

McDonnell-Douglas Astronautics Co. (2)
P.O. Box 516
St. Louis, MO 63166

D. Kummer
JE O'Neal

Mound Laboratory
P.O. Box 32
Miamisburg, OH 45342

Manager, Tech Appl & Dev

National Bureau of Standards
Gaithersburg, MD 20760

CD Bowman

Naval Research Laboratory (3)
Washington, DC 20375

I. Manning, Code 6672
JA Sprague, Code 6395
LE Steele, Code 6390

North Carolina State University
Department of Nuclear Engineering
Raleigh, NC 26707

JR Beeler, Jr.

Oak Ridge National Laboratory (12)
P.O. Box X
Oak Ridge, TN 37830

Director, Thermonuclear Div,
(Bldg 9201-2)

J. Bentley
MR Hayns
RW Hendricks
PJ Maziasz
NH Packan
FG Perey
M. Roberts, Bldg 9204-1
J. Sheffield
JO Stiegler
C. Weisbin
FW Wiffen

DISTRIBUTION (Cont'd)

Princeton University (2)
Plasma Physics Laboratory
Forrestal Campus
P.O. Box 451
Princeton, NJ 08544

K. Wakefield
H. Furth

Rockwell International
8900 DeSoto Ave
Canoga Park, CA 91304

O. Kramer

Sandia Laboratories (2)
P.O. Box 5800
Albuquerque, NM 87185

FL Vook, Org 5100
ST Picraux, Div 511

Sandia Laboratories
Livermore, CA 94550

WD Wilson

Stanford University
Dept of Materials Science & Eng
Stanford, CA 94305

R. Sinclair

University of California
Berkeley, CA 94720

K. Westmacott

University of California
Dept of Chemical & Nuclear Eng
Santa Barbara, CA 93106

GR Odette

University of California (2)
School of Eng & Applied Science
Los Angeles, CA 90024

RW Conn
L. Weaver

University of Cincinnati
materials Science &
Metallurigical Eng Dept
Cincinnati, OH 45221

J. Moteff

University of Michigan
Nuclear Engineering
Ann Arbor, MI 48109

T. Kammash

University of Missouri
Mechanical & Aerospace Engineering
1006 Engineering Bldg
Columbia, MO 65211

M. Jolles

University of Virginia (2)
Deot of Materials Science
Charlottesville, VA 22901

WA Jesser
ML Sattler

University of Wisconsin (3)
Dept of Metallurgical Engineering
1509 University Ave
Madison, WI 53706

MG Lagally
P. Wilkes
WG Wolfer

DISTRIBUTION (Cent'd)

Westinghouse
Advanced Reactors Division (2)
P.O. Box 158
Madison, PA 15663

A. Boltax
AL Chang

Westinghouse
Research and Development Center (2)
1310 Beulah Road
Pittsburgh, PA 15235

WJ Choyke
JA Spitznagel
S. Wood

(AECL)
Atomic Energy of Canada LTD
Whiteshell Nuclear Research
Establishment
Pinawa, Manitoba Roe ILO

D. Faulkner

Commission for the European Communities
200, Rue de la Loi
B-1049 Brussels, Belgium

J. Darvas

(ECN)
Energieonderzoek Centrum Nederland
Westerdionweg 3
NL-1755 ZG Petten, NH, The Netherlands

B. Van Der Schaaf

(EIR)
Swiss Federal Institute
For Reactor Research
CH-5303 Wuerenlingen, Switzerland

WV Green

EURATOM
Joint Research Center Ispra
Materials Science Division
1-21020 Ispra, Varese, Italy

P. Schiller

Hahn-Meitner Institute
fur Kernforschung
Glienickerstrasse 100
0-1000 Berlin,
Federal Republic of Germany

H. Wollenberger

Japan Atomic Energy Research Institute
Physical Metallurgy Laboratory
Division of Nuclear Fuel Research
Fukoku Seimei Bldg
2-2, Uchisaiwai-cho 2-chome, Chiyoda-ki,
Tokyo 100, Japan

K. Shiraishi

(KFA-IFF)
Kernforschungsanlage Julich GmbH
Postfach 1913
D-517 Julich,
Federal Republic of Germany

H. Ullmaier

(KFK-IMF II)
Kernforschungsaniage Karlsruhe
Institut fur Reaktorbauelemente
Postfach 3640
D-7500 Karlsruhe 1,
Federal Republic of Germany

K. Ehrlich

DISTRIBUTION (Cont'd)

National Research Council
Montreal Road
Ottawa, Canada

EV Kornelsan

Osaka University
beat of Nuclear Enaineerina
2-1, Yamada-Oka, Suita,
Osaka, 565, Japan

K. Sumita

Science University of Tokyo
Engineering Dept
Kagurazaka, Shinjuku-Ku
Tokyo, 162, Japan

RR Hasiguti

(SCK/CEN)
Studiecentrum voor Kernenergie
Centre d'Etude de l'Energie Nucleaire
Boeretang 200
B-2400 Mol, Belgium

J. Nihoul

Tokyo Institute of Technology
T2-1, 2-Chome, O-Okayama
Meguro-Ku, Tokyo, Japan

K. Kawamura

(UKAEA-Harwel 1)
United Kinadom Atomic Energy Authority
Atomic Energy Research Establishment
Metalluray Division
Building 388
Oxfordshire, OX11 ORA, UK

DR Harries

University of Tokyo (3)
Bunkyo-ku,
Tokyo 113, Japan

Naohiro Igata
Shiori Ishino
Taijiro Uchida

HEDL (38)

HR Brager	W/A-64	NF Panayotou	W/A-65
WL Bunch	W/B-47	EF Parker	W/E-17
LL Carter	W/B-47	RW Powell	W/A-64
DG Doran (5)	W/A-57	RJ Puigh	W/A-58
EA Evans	W/C-23	FH Ruddy	W/C-39
FA Garner	W/A-57	FA Schmittroth	W/A-4
DS Gelles	W/A-64	WF Sheely	W/C-62
R. Gold	W/C-39	RL Simons	W/A-57
HL Heinisch	W/A-57	AL Trego	W/E-15
DL Johnson	W/A-4	GL Wire	W/A-58
GD Johnson	W/A-65	HH Yoshikawa	W/C-44
NE Kenny	W/C-115	Central Files (5)	W/C-110
FM Mann	W/A-4	Publ Services (2)	W/C-115
WN McElroy	W/C-39	Doc Management	W/C-125
EK Opperman	W/A-58		